Cold Flow Plume Entrainment Test Final Report
NTF Test Number 2456

11/2005
Joseph Ruf, joseph.h.ruf@nasa.gov, 256 544 4942
David McDaniels, david.mcdaniels@nasa.gov, 256 544 1578
Jason Mishtawy, jason.e.mishtawy@nasa.gov, 256 544 4077
NASA/Marshall Space Flight Center, Huntsville, AL
Dr. Narayanan Ramachandran, narayanan.ramachandran@msfc.nasa.gov,
256 544 8308, BAE Systems Analytical Solutions Inc., Huntsville, AL
and
Dr. Khaled J. Hammad, Khaled.hammad@dantecdynamics.com,
201 236 2466, Dantec Dynamics Inc., Ramsey, NJ.

> *This is a final version of the report on the test.*
> *It has been given to Tech Pubs to convert to a NASA TP.*
> *Tech Pubs will put it in the appropriate format.*
> *The information contained in it will not change.*

Table of Contents

List of Figures

Trademarked/Registered Names

Excel
TecPlot
Hewlett-Packard
National Instruments
Pressure Systems, Inc.
Dantec Dynamics, Inc
BAE SYSTEMS Analytical Solutions, Inc
FlowMap
New Wave Research
PIVTEC
TSI
Aerotech
Labview

Acronyms

NTF Nozzle Test Facility
LIFO Last In First Out
TCP/IP Transmission Control Protocol/Internet Protocol
PCI-MIO Peripheral Component Interconnect – Multifunction Input/Output
PC Personal Computer
FOV Field of View
CCD Charged Coupled Device
NASA National Aeronautics and Space Administration
MSFC Marshall Space Flight Center
PSI Pressure Systems Inc.
PIV Particle Image Velocimetry
HFA Hot Film Anemometry
RTF Return to Flight
CFD Computational Fluid Dynamics
DTA Debris Transport Analysis
NI National Instruments
NPR Nozzle Pressure Ratio
SCXI Signal Conditioning Extension for Instrumentation

Nomenclature – in order of use

P_{static} = nozzle inlet static pressure
P_{total} = nozzle inlet total pressure
$P_{ambient}$ = ambient pressure
P_{inlet} = nozzle inlet pressure
T_{total} = nozzle inlet total temperature
$T_{ambient}$ = ambient temperature
dX = particle displacement
$\sigma(\Delta x_i)$ = position uncertainty
N = Number of particles

Xpix, Ypix, = average particle displacement in X and Y directions
X, Y = coordinates in the nozzle global coordinate system
X´, Y´ = coordinates in the plume capture pipe coordinate system
U, V = velocity along X and Y directions
dy = distance from nozzle outer diameter

1. INTRODUCTION

As part of the Space Shuttle Return to Flight (RTF) program, Marshall Space Flight Center (MSFC) performed computational fluid dynamics (CFD) analysis to define the velocity flowfields around the Shuttle stack at liftoff. These CFD predicted velocity flowfields were used in debris transport analysis (DTA). High speed flows such as plumes induce or 'entrain' mass from the surrounding environment. Previous work had shown that CFD analysis over-predicts plume induced flows. Therefore, the DTA would tend to 1) predict more debris impacts, and 2) the debris velocity (and kinetic energy) of those impacts would be too high.

At a November, 2004 peer-review it was recommended that the Liftoff DTA team quantify the uncertainty in the DTA caused by the CFD's over prediction of plume induced flow. To do so, the Liftoff DTA team needed benchmark quality data for plume induced flow to quantify the CFD accuracy and its effect on the DTA.

MSFC's Nozzle Test Facility (NTF) conducted the "Nozzle Induced Flows test, P#2456" to obtain experimental data for plume induced flows for nozzle flow exhausting into q quiescent freestream. Planning for the test began in December, 2004 and the experimental data was obtained in February and March of 2005. The funding for this test was provided by MSFC's Space Shuttle Propulsion Systems Integration and Engineering office.

2. TEST PROGRAM

The NTF normally tests subscale nozzles in a sealed test cell that is evacuated to simulate altitude. The test medium, or nozzle's working fluid, is warm air. The NTF was modified to move the nozzle test articles downstream and outside of the test cabin to enable measuring the entrainment of the surrounding air. See Section 2.2 for a description of the NTF and modifications to it for this test.

This experiment was run with two existing test articles; a Stratford nozzle and a Bell nozzle. The Stratford nozzle has a design area ratio of 1.115; the Bell, 12.2. These test articles are fully described in Section 2.1.

The Bell nozzle entrainment data was of primary interest to the Liftoff DTA team. Within the limits of the NTF capabilities, it provided a plume structure most similar to a Space Shuttle main engine's plume at sea level. The Stratford nozzle, being close to a sonic nozzle, provided an entrainment dataset with simpler plume physics.

The test data acquired and documented in this report consists of; Schlieren images of the plume structure, fog based flow visualization, nozzle wall pressures (Bell only), particle image velocimetry (PIV), and hot film anemometry (HFA). The test data systems and test setup are described in Section 2.3. The test results are presented and discussed in Section 3.

2.1.   Description of Nozzle Test Articles

The nozzle test articles are shown in Figure 1. Both are aluminum. The Stratford nozzle cross-section is shown in Figure 2. It has a design area ratio of 1.115. Its as-designed throat diameter is 35.56mm. The Stratford nozzle's throat was measured at 35.725mm. The difference between the as-designed and the as-built throat diameters results in a 1% increase in throat area. The nozzle's internal contour shown on the drawing, the as-designed contour, (Figure 2) was generated with the formula as defined in Reference 1. Appendix 1 contains a table (Table A1) of nozzle wall points calculated with the formula in Reference 1. The Excel® file ('NozzleInternalGeo.xls') used to generate the nozzle internal contour in Table A1 and for the test related computational fluid dynamics is included in the electronic media associated with this report.

The Stratford nozzle did not have internal wall pressure measurements.

The Bell nozzle cross-section is shown in Figure 3. It has an area ratio of 12.2. Its throat diameter is 39.218mm. The nozzle wall is 12.7mm thick. The as-designed internal contour points for this nozzle are in Table A2 in Appendix 1. This internal contour is contained within the Excel file, 'NozzleInternalGeo.xls', which is included in the electronic media associated with the report.

The Bell nozzle had about 40 static pressure measurements on its internal wall. The locations of these are also defined in Table A3 in Appendix A.
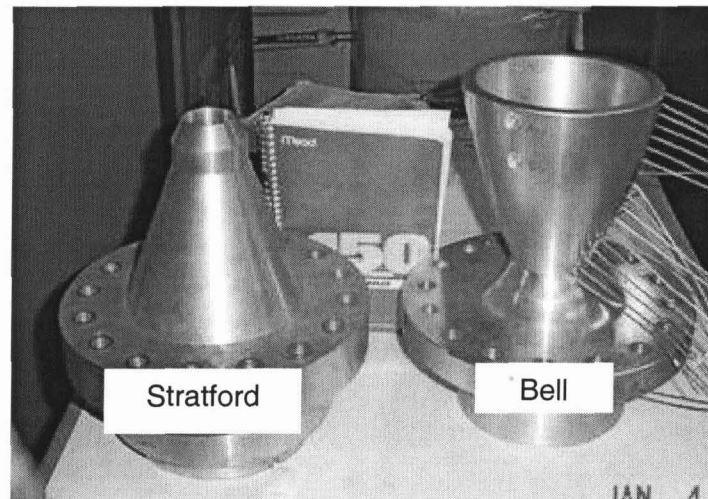
Figure 1. Nozzle Test Articles.

START OF CURVE
X=0.000
Y=0.000

146.4 Diameter

59 Diameter

BREAK EDGE

0.933

2.100

END OF CURVE
X=3.850
Y=0.510

2.800 R

1.624

B

32

ø4.200

35.725

1.400   1.478   **20.3**

0.933R

15.875

16

16.51

ø.047THRU
C'BORE ø.125°.250P

109.2

32.39

A

51.3   **38.1**   **141.6**

231
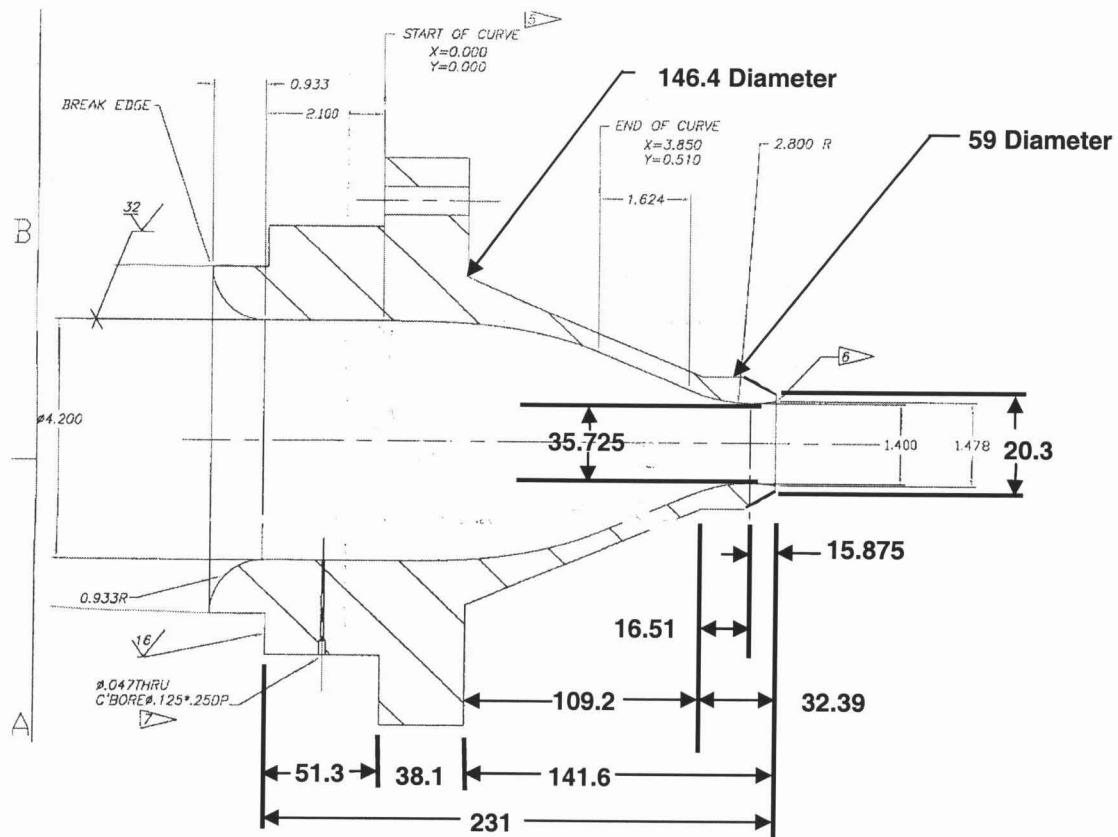
Figure 2. Sonic Nozzle Cross-Section.
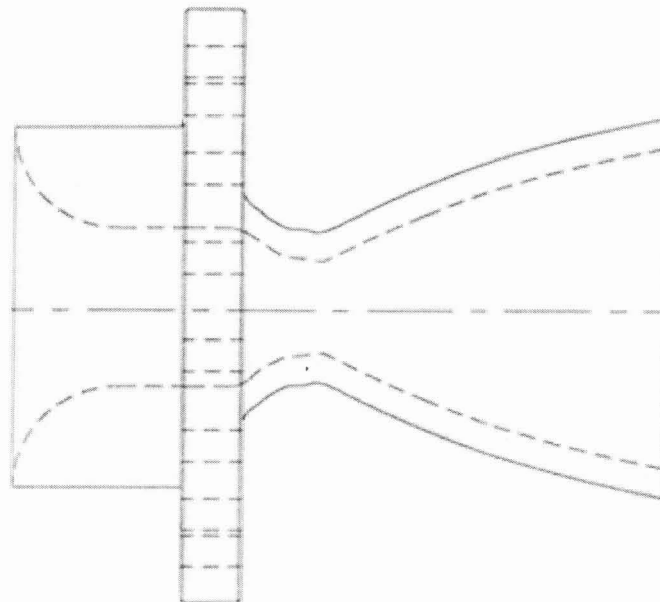
Figure 3. Bell Nozzle Cross-Section.

2.2.   Test Facility

The NTF is designed to determine nozzle performance across a wide range of pressure ratios. The supply system can provide up to 5.4 kgm/s of heated (up to 422°K) air at 20.4 atmospheres. The test cabin pressure can be reduced to pressures as low as 6.8e-3atm and is controlled with a two-stage air ejector system. Thrust and off-axis loads generated by nozzles are measured with flexure-isolated load cells. Induced loads from thermal growth and bringing flow across the metric plane are accounted for with a tare process.

Facility instrumentation used in this test consisted of mass flow and nozzle inlet total temperature and pressure. Schlieren images of the plume structure were recorded on a video camera.

The data acquisition system is composed of thermocouples and individual pressure transducers from various manufacturers, two Pressure Systems, Inc®. (PSI) Model 780B pressure scanners, a Hewlett-Packard® Model 3852 Integrating Voltmeter, and two National Instruments® SCXI multiplexers connected to National Instruments PCI-MIO-16 cards. Data is collected by three desktop computers.

2.2.1. Modifications for Current Test

The NTF was modified, as shown schematically in Figure 4, to move the nozzle out of the test cabin to a new test position downstream and outside of the test cabin. Photographs of the NTF before and after the modification are shown in Figure 5 and Figure 6. To move the nozzle downstream, a pipe was fabricated and attached to the flow straightening section that remained in the test cabin. The load cell normally used to measure thrust remained in place, but thrust was not a desired measurement in this experiment. Furthermore, securing the extension pipe in place invalidated the thrust measurement. No valid thrust measurements were obtained.

The ejector pipe was cut as shown in Figure 6 to become the 'plume capture pipe'. The ejectors were not run during this experiment. However, the ejector hardware remained within the plume capture pipe. This hardware is approximately three meters downstream of the pipe entrance.
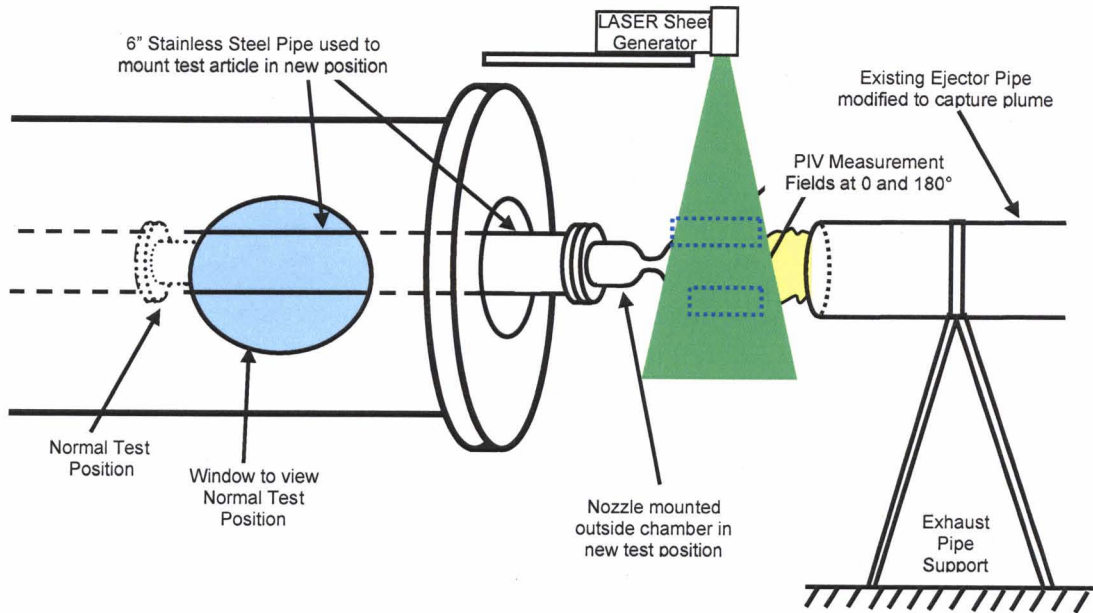
Figure 4. Schematic of Test Set Up.
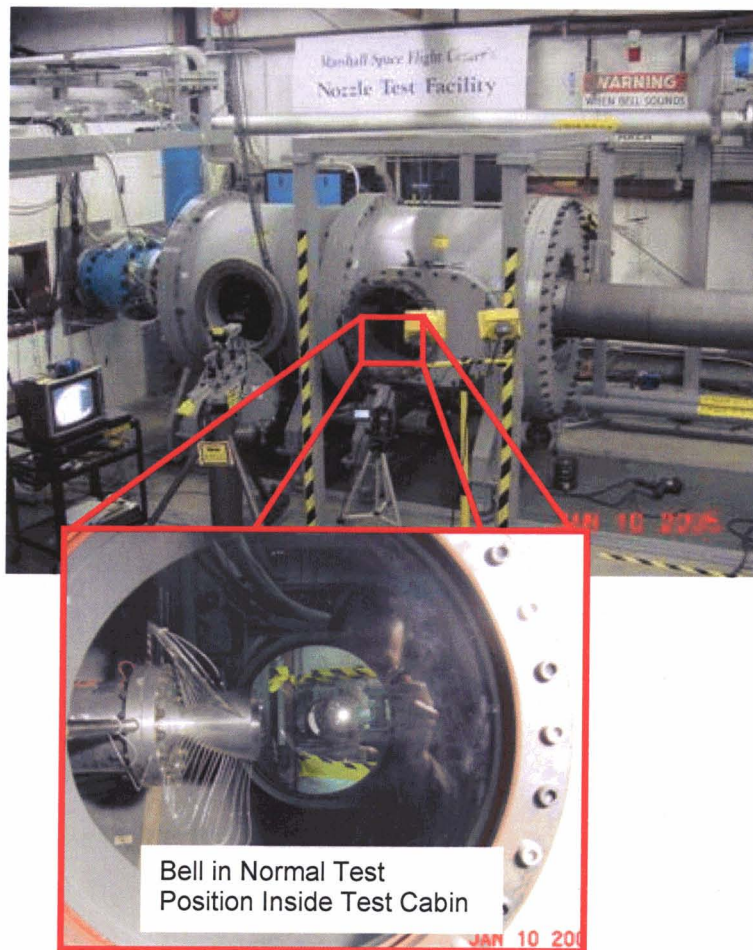
Figure 5. Nozzle Test Article in Normal Test Position.
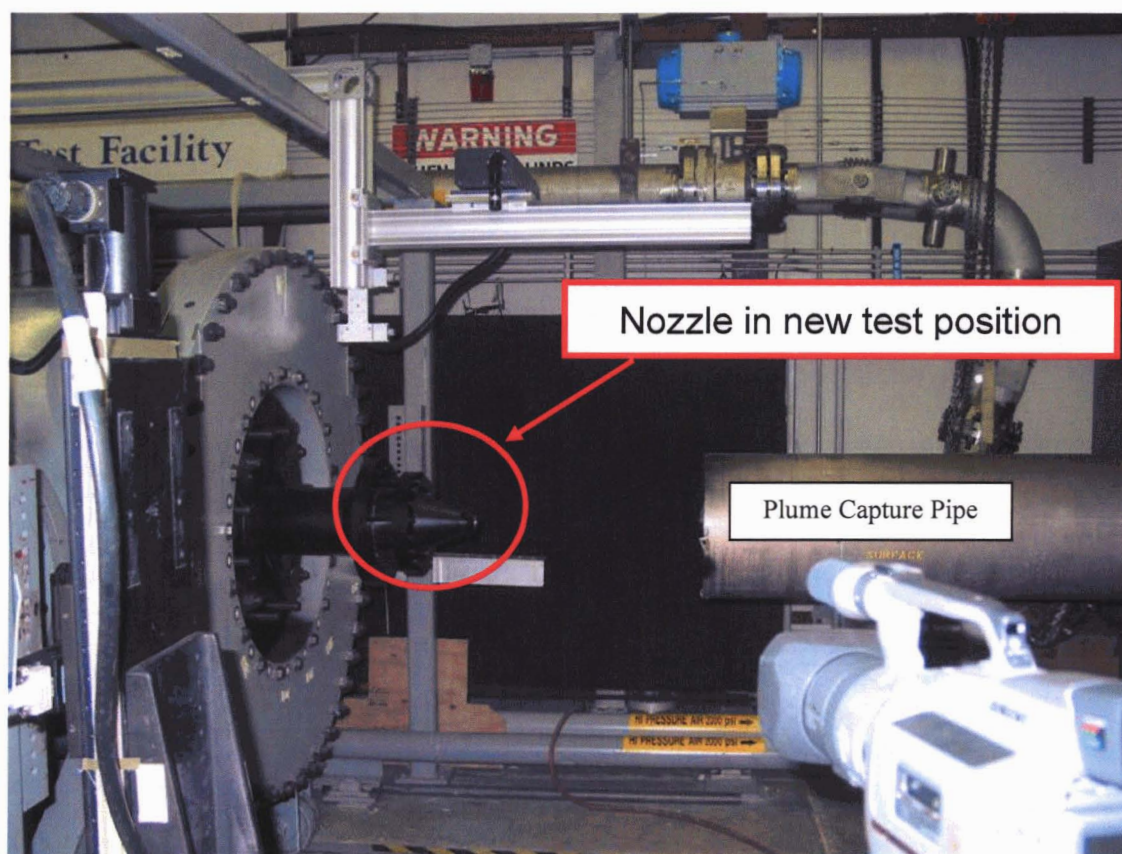
Figure 6. Stratford Nozzle in New Test Position.

2.2.2. Geometry of Current Test Configuration

The layout of the room (A-bay of building 4777) containing the NTF is shown in Figure 7. There were several small holes in the walls, and three large openings in the building though which outside air entered the building during the experiment. The large openings were the roof vents, the rollup garage door and the doorway between A-bay and B-bay.

There was a fourth large opening for part of the testing. A window (approximately 813mm wide by 508mm tall) in the south wall of the A-bay was open during acquisition of the Stratford PIV windows A, B, E, F and C. Between the window and the test cabin, a screening panel was placed to divert the inflow and reduce its northerly momentum. After the Stratford PIV C window data was obtained, the window was covered with a tarp, which significantly reduced the air flow through it. Partially covering this window with the tarp was one of the parametrics done to improve the seed quality for the PIV. The tarp remained in place through the rest of the PIV data acquisition and all of the HFA data acquisition.

The ceiling vents were approximately one third of the length of the building, centered, north to south, in the ceiling. They were about 300mm wide, east to west and were opened, vertically, approximately 200mm. The rollup door was 4.2m wide and was raised approximately 700mm. The doorway between the A and B-bay is 2108mm tall by 84mm wide.

Figure 7 indicates the plume capture pipe centerline was on the same centerline as the test articles. However, the plume capture pipe centerline was offset approximately 25mm south of the nozzles' centerlines. The plume capture pipe centerline was approximately parallel to the nozzles' centerlines. The centerlines were coincident in the horizontal plane (i.e., relative to the floor).

The Bell nozzle setup is shown in Figure 8 and Figure 9. The Stratford nozzle setup is shown in Figure 10. Figure 8 and Figure 10 are both looking south. Those dimensions not shown in the Stratford image can be found in the Bell nozzle images. The distances from the floor to the outer diameter of the nozzle (in the 180° plane) were 1121 and 1182mm for the Bell and Stratford nozzles, respectively.
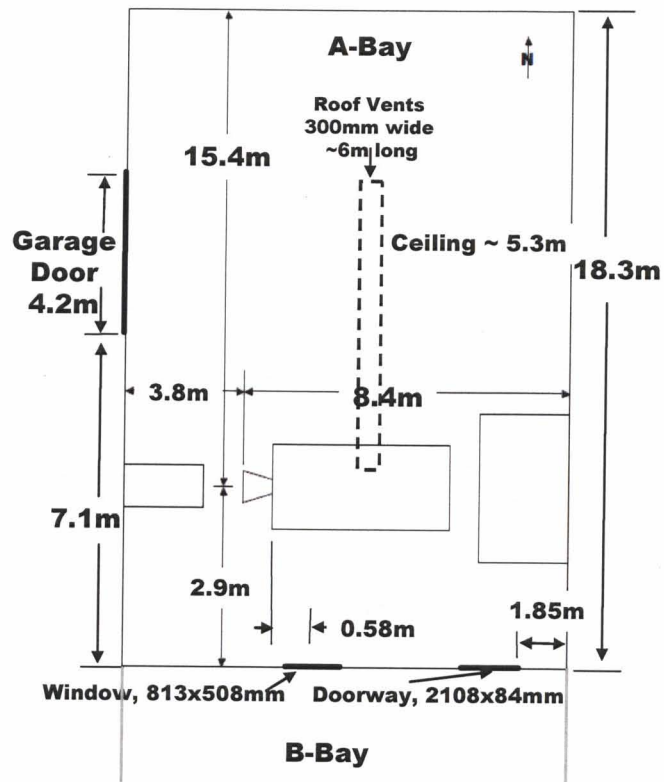
Figure 7. Layout of A-Bay.
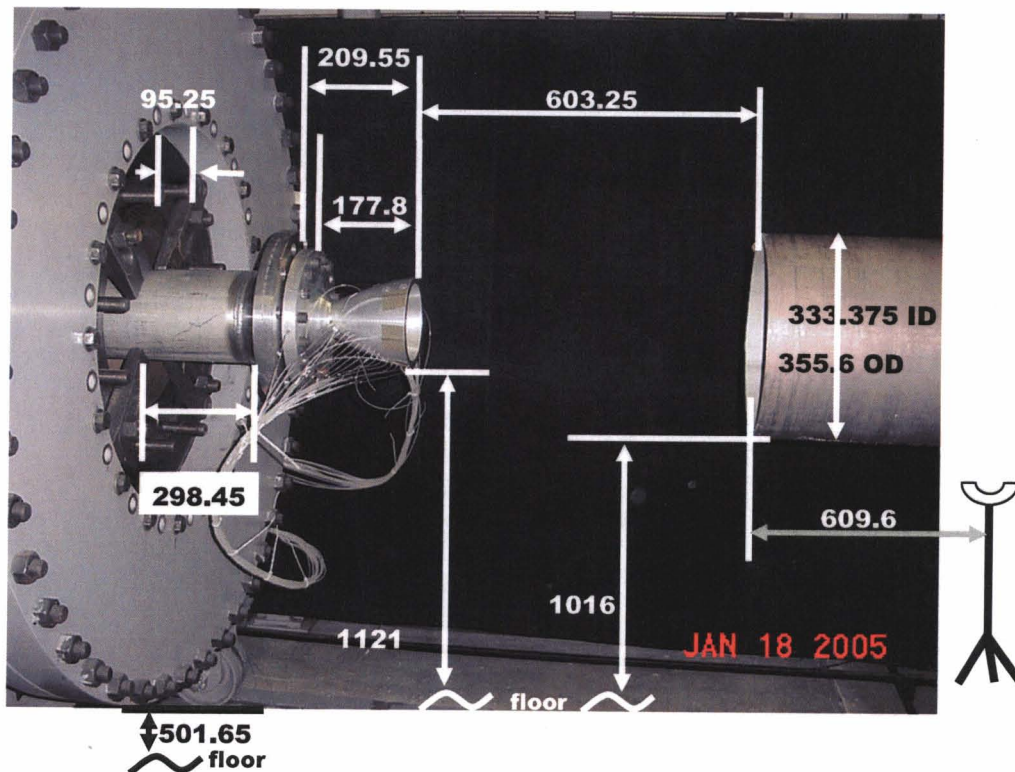
Figure 8. Dimensions (in mm) of Bell Nozzle Test Configuration.
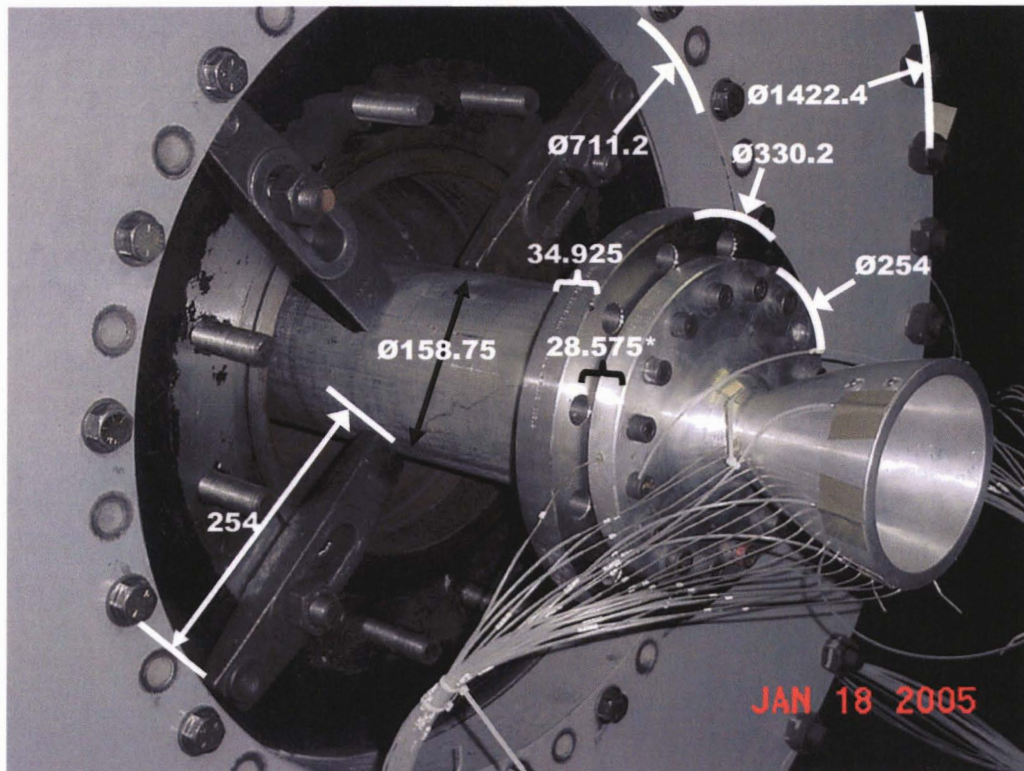
Figure 9. Details of Bell Nozzle Test Configuration. Dimensions in mm. *Includes Thickness of Gasket.
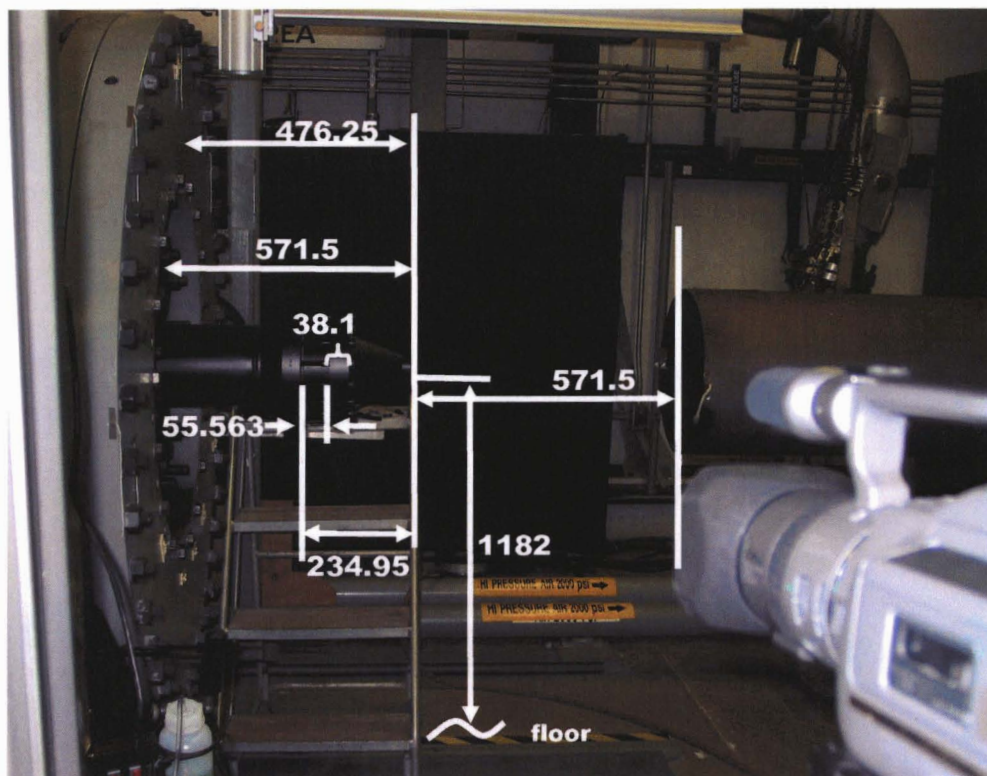
Figure 10. Dimensions (in mm) of Stratford Nozzle Test Configuration.

2.3.   Test Data Systems

2.3.1. Pressure Measurements

The static and total pressures were recorded on a Pressure Systems Inc. (PSI) Model 780B pressure scanner. The PSI hardware scanned the pressures faster than 100Hz. The PSI hardware averaged the eight most recent scans of each channel then transmitted 'frames' of all of the channels at slightly less than one frame per second. The pressure measurements were recorded four times a second in the 'facility data'. The facility data contains other pressure and temperature measurements of interest to the facility operators. Facility data was acquired on a National Instruments PC based system.

Five, 10 second slices of the facility data were averaged to create five sets of nozzle wall static pressure data for the Bell nozzle. These sets of wall static pressure data are presented in Section 3.3. The locations of the measurements are described in Section 2.1 and Appendix 1. The Bell nozzle had about 40 static pressure measurements. The Stratford nozzle had no static pressures measured in or on the nozzle.

2.3.2. Particle Image Velocimetry System

Dr. Ramachandran, of BAE SYSTEMS Analytical Solutions Inc®, assisted in scoping the initial PIV requirements and identifying a company that could perform the PIV measurements. BAE subcontracted the PIV measurement task to Dantec Dynamics Inc®. Dr. Hammad was the Dantec Dynamics representative responsible for making the PIV measurements. Dr. Hammad was involved in the pre-test discussions and made a pre-test consultation visit to MSFC to set the final PIV requirements. Dr. Hammad traveled to MSFC to make the PIV measurements. Drs. Ramachandran and Hammad both helped manipulate and interpret the PIV data.

In PIV, the flow's velocity vectors are derived from the movement of particles in the flow. The basic PIV process is shown in Figure 11[2], and can be described as follows. The flow is seeded with light reflecting particles. The flow in the target area is then illuminated with a pulsed laser light sheet. A camera lens images the target area onto the charged coupled device (CCD) array of a digital camera. The CCD captures each light pulse as a separate image frame. Pairs of images are recorded with a known time difference between them. These images are divided into small sub-sections called interrogation areas. The interrogation areas from each image frame are cross-correlated, pixel by pixel. The correlation produces a signal peak, identifying the common particle displacement, dX, for each interrogation area. An accurate measure of the displacement, and thus the velocity, is achieved with sub-pixel interpolation. A velocity vector map over the whole target area is obtained by repeating the cross-correlation for each interrogation area within the image pair.

The number of velocity vectors in the vector map is dependent upon the number of pixels in the CCD camera and the size of the interrogation area. For these entrainment tests a CCD camera with 1186 by 1600 pixels was used for PIV image acquisition. The interrogation areas selected were 64 by 64 pixels with 50% overlap in each direction. The overlapping technique is used for optimizing the information available in the image

maps. With the setup used in these entrainment tests, each PIV dataset resulted in a vector map of 36 by 49 data points distributed at regular spacing throughout the camera's field of view (FOV). The CCD camera's FOV was approximately 133 by 180mm. The camera was approximately 1m from the laser sheet. Multiple PIV datasets were recorded for each nozzle tested. See Sections 3.4.1.1 and 3.4.2.1 for specifics on the PIV datasets recorded.

To obtain different datasets the PIV camera was positioned by a traverse system. It consisted of two Unidex 11 Aerotech® linear stages, each with 300mm traverse length, configured in an orthogonal two dimensional traverse system.

A Dantec Dynamics Inc. PIV system, "FlowMap"[3], was used in these tests. It consisted of a dual pulsed laser system, light sheet optics, the system hub, a personal computer (PC) with the FlowMap® software, and GigaBit Ethernet communications link between the PC and the system hub. The laser was a New Wave Research® Solo Nd-Yag high-energy double oscillator pulsed laser. This class IV laser provided light pulses with a maximum energy of 120mJ at a wavelength of 532nm. The laser illuminated at a rate of 15 pairs of pulses per second. A Dantec Dynamics 80X60 series light sheet optics setup was used to generate a pulsing light-sheet for image plane illumination. The typical light sheet thickness was 2 to 3mm.

The FlowMap System Hub executed the measurement task in uninterrupted sequences, while the personal computer performed on-line analysis of the data at the performance pace of the PC. Communication between the FlowMap System Hub and the PC was via a TCP/IP protocol. The GigaBit Ethernet connections were established in a peer-to-peer configuration. The FlowMap System Hub also maintained control of the auxiliary devices such as cameras and lasers, and receiving or sending trigger signals to or from other devices associated with the measurements.

The flexible connectivity of the FlowMap System Hub, whether through a network or in a peer-to-peer connection, was of great benefit here since the application PC was located in a control room, where all monitoring of the experiment took place.

On-line feedback during data acquisition was accomplished via a FlowMap System Hub LIFO (last-in first-out) capability. The LIFO on-line capability manages data buffers to guarantee the acquisition performance of the system in uninterrupted sequences, while still being able to display on-line images and on-line derived analysis, such as PIV velocity vector maps. During PIV data collection, the FlowMap System Hub supplied the PC with images at a pace giving the PC time to analyze the data according to the complexity of the task and the computing capability of the PC. The LIFO on-line capability also allowed for the display of the newest information during the data run, so recording quality can be monitored on-line at the same time as the images were safely stored at full system performance. No lab time was wasted, when the images were being recorded, the on-line monitoring capability ensured a successful off-line post-processing.

An air operated seeder (PivPart40 from PIVTEC®) was used to generate seed particles for the entrainment tests. Olive oil was used as the seed medium and a typical particle size of 1μm. The operating pressure of the seeder was set to about 3bar.
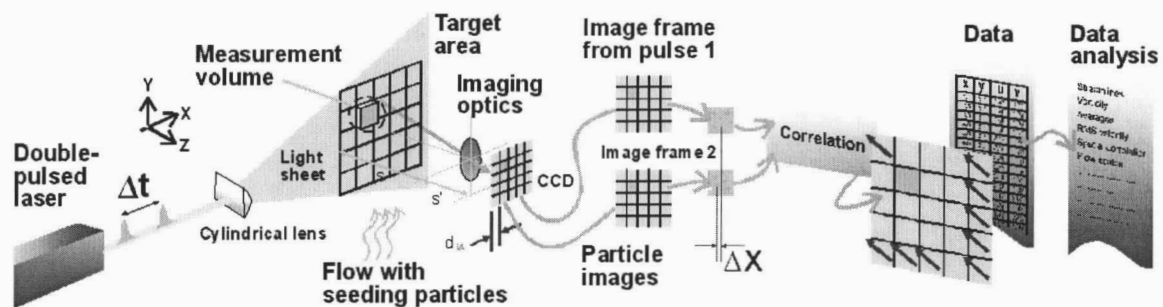
Figure 11. The Basic PIV Process.

2.3.3. Hot Film Anemometry System

BAE SYSTEMS Analytical Solutions Inc, an MSFC support contractor, developed the hot film anemometry system with hardware available at BAE and MSFC. The HFA measurements were made with a TSI® Model Intelligent Flow Analyzer 100. The hot film probes were model TSI 1260A-10. The probes were mounted in a Unidex 11 Aerotech traverse mechanism. During a data acquisition run, the traverse mechanism was capable of 300mm movement in two axes. The traverse mechanism was mounted on a rail system and moved manually between runs as necessary.

The Labview® programming language was used to drive the traverse mechanism, tell the Intelligent Flow Analyzer when to acquire each data point and then store the HFA data. It also was used to process the HFA data against the probes' calibrations. The probes were calibrated in a TSI calibrator model 1125.

2.4.   Nozzle Set Point Repeatability and Data Accuracy

This section discusses the variability of the nozzle inlet set point conditions for both nozzles. It then discusses the accuracy of the static pressure measurements made for the Bell nozzle. The accuracy of the PIV measurements is then discussed. This PIV accuracy is an 'uncertainty' on the value of the velocity assigned to each data point based on the image processing technique used in PIV. It is not a total uncertainty which should include at least the effect of:

- nozzle inlet condition set point variation,
- variations in the ambient conditions,
- positional errors in setting up and translating the camera.

A total uncertainty is not calculated for any of the data presented in this report. Repeatability of the PIV measurements is assessed in Section 3.4.4.

2.4.1. Nozzle Inlet Conditions

The set points for nozzle inlet conditions for the Stratford and Bell nozzles were 338.9° K at 10.3 and 19.39atm, respectively. After the test, the facility measurement of nozzle inlet total pressure (P_{total}) was found to be leaking. The corresponding nozzle inlet static pressure (P_{static}) did not leak. When testing the Stratford and Bell nozzles, the area ratio for the location at which these facility measurements were made was 18.77 and 15.42, respectively. Using isentropic gas relations, P_{total} should equal $P_{static}/0.9993$ and $P_{static}/0.999$, respectively. These ratios result in a P_{total} approximately 0.015atm higher than P_{static}. This small difference is well within the ±0.15% accuracy (or ± 0.051atm) of the 0 to 34atm pressure gages used for these nozzle inlet pressures. Hence, for the test data and through out this report, the P_{static} measurement was used for nozzle inlet (i.e., total) pressure.

Stratford Nozzle Inlet Conditions for PIV Acquisition

The variation of the nozzle inlet conditions during PIV data acquisition for the Stratford nozzle is shown in Figure 12 and Figure 13. The average value of the Stratford nozzle inlet conditions during PIV acquisition for each data set or 'window' is provided in Table 1.

Table 1. Average Stratford Nozzle Inlet Conditions and Ambient Temperature During
PIV Data Acquisition

Window	Pstatic Avg (Atm)	Ttotal Avg (K)	Tambient Avg (K)
A	10.36	338.30	291.88
E	10.36	338.94	291.28
B	10.35	339.36	290.80
F	10.36	338.26	290.06
C	10.36	338.23	292.26
G	10.37	341.53	293.47
D	10.37	339.69	293.65
H	10.37	336.91	293.79
I	10.31	339.14	290.50
J	10.31	339.15	290.62
B180	10.36	339.88	294.31
F180	10.35	337.95	294.36
C180	10.35	337.07	294.20
G180	10.35	340.22	294.56
D180	10.35	338.08	294.48
H180	10.35	336.76	294.37

There was very little variation of nozzle inlet pressure. The I and J windows had
slightly lower nozzle inlet pressure. The nozzle inlet temperature was usually close to
339°K, but was as high as 342°K and as low as 334°K. The nozzle inlet temperature was
measured with a type K thermocouple with an accuracy of ±2.2°K.
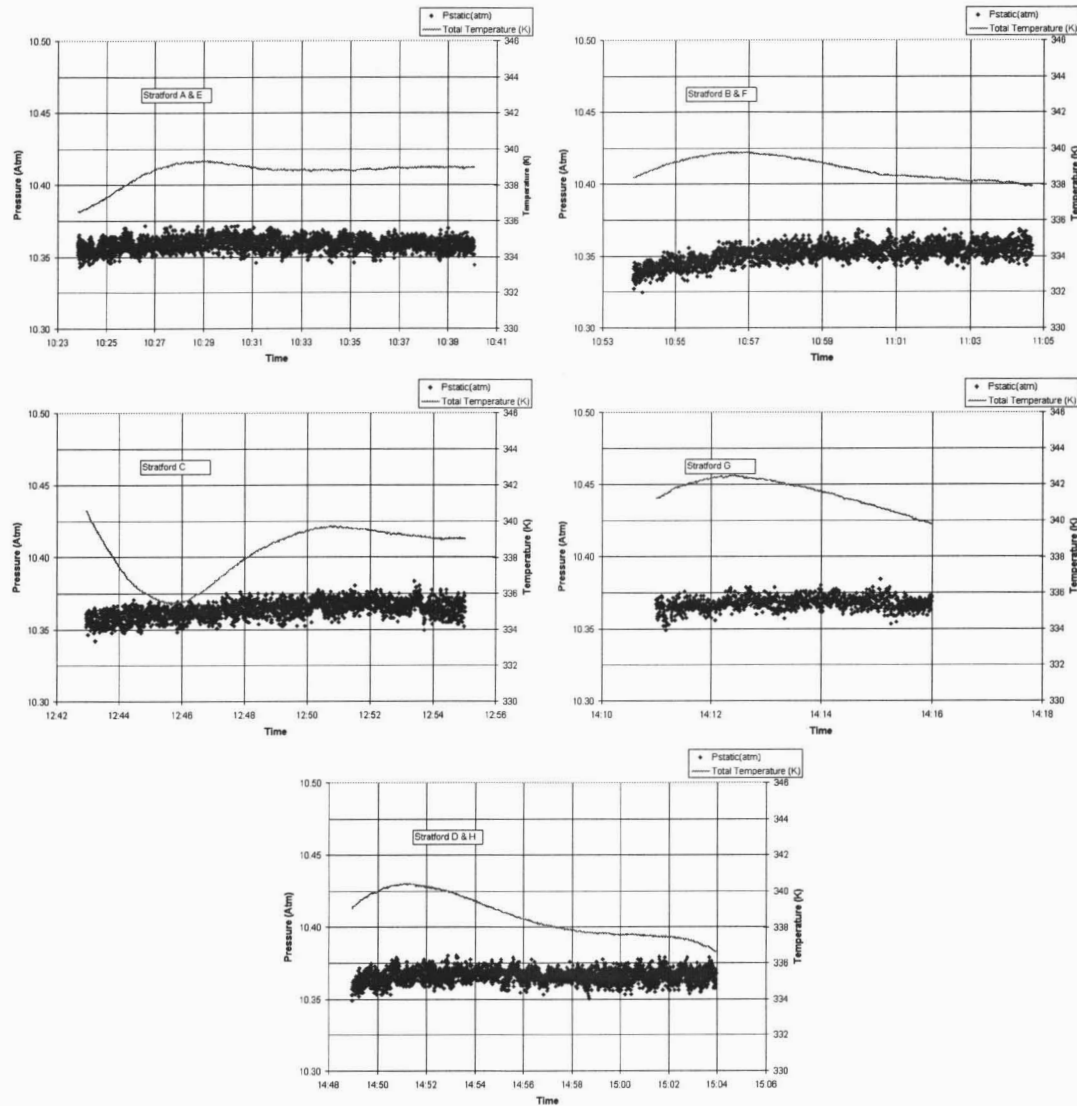
Figure 12. Stratford Nozzle Inlet Conditions for Windows A Through H.
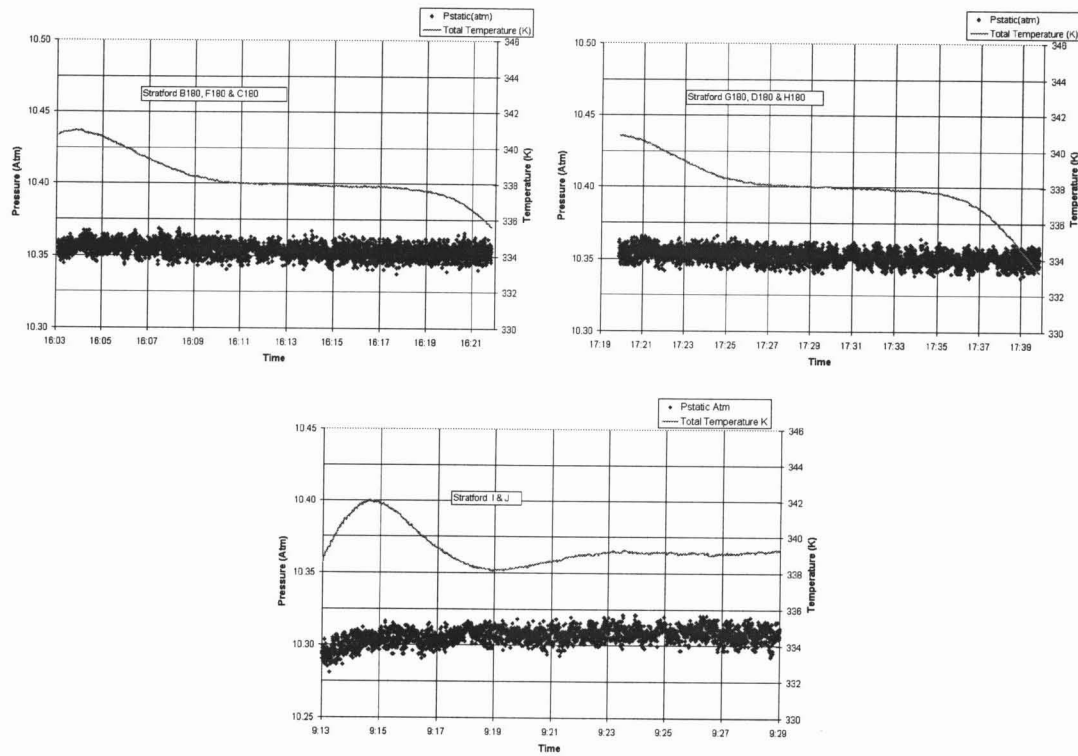
Figure 13. Stratford Nozzle Inlet Conditions, Continued for Windows B180 Through H180 and I and J.

Bell Nozzle Inlet Conditions for PIV Acquisition

The variation of the nozzle inlet conditions during PIV data acquisition for the Bell nozzle is shown in Figure 14 and Figure 15. The average value of the Bell nozzle inlet conditions during PIV data acquisition in each window is provided in Table 2.

Table 2. Average Bell Nozzle Inlet Conditions and Ambient Temperature During PIV Data Acquisition.

Window	Pstatic Avg (Atm)	Ttotal Avg (K)	Tambient Avg (K)
A	19.67	340.0	291.6
E	19.70	338.5	291.8
B	19.68	338.0	292.5
F	19.65	338.8	292.5
C	19.65	335.8	294.0
G	19.64	338.3	294.1
D	19.62	337.9	294.6
H	19.65	338.5	294.7
K	19.55	338.9	294.7
B180	19.66	337.1	296.0
F180	19.68	339.0	296.0
G180	19.61	338.4	296.1
C180	19.40	338.3	296.1
D180	19.19	337.3	296.1
H180	18.92	337.2	296.1

The saw tooth variation in nozzle inlet pressure was relatively small compared to its magnitude. During acquisition of the PIV measurements in windows A through G180 the difference between the maximum and minimum nozzle inlet pressure was about 0.3atm, or 1.5% of intended set point. This variation was due to the nozzle set point being near the NTF maximum supply pressure. As NTF supply pressure dropped, the facility valve settings were adjusted to hold temperature and pressure set points close to the intended values.

For windows B180, F180 and G180, the set point was well maintained. Windows C180, D180 and H180 were obtained as the nozzle inlet pressure began to fall off. No effect was seen on the flow entrained in the PIV data . The nozzle inlet temperature only varied slightly. The nozzle inlet temperature was measured with a type K thermocouple with an accuracy of ±2.2°K.
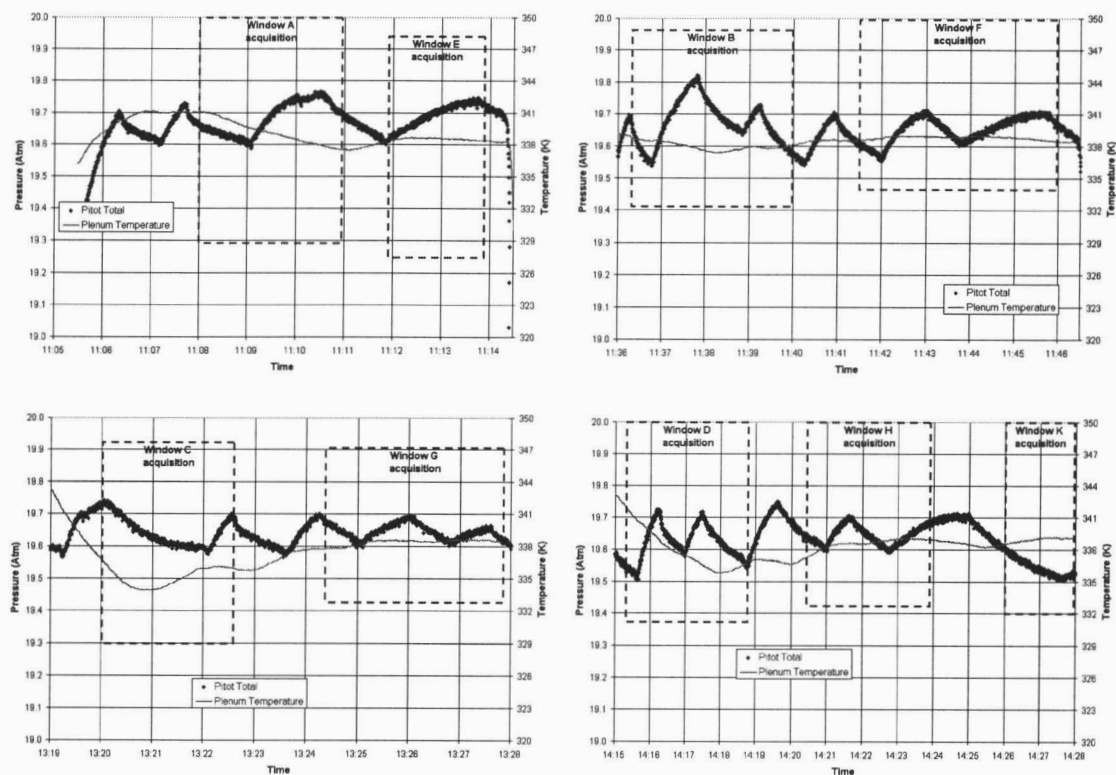
Figure 14. Bell Nozzle Inlet Conditions During Runs 51, 52, 53 and 54.
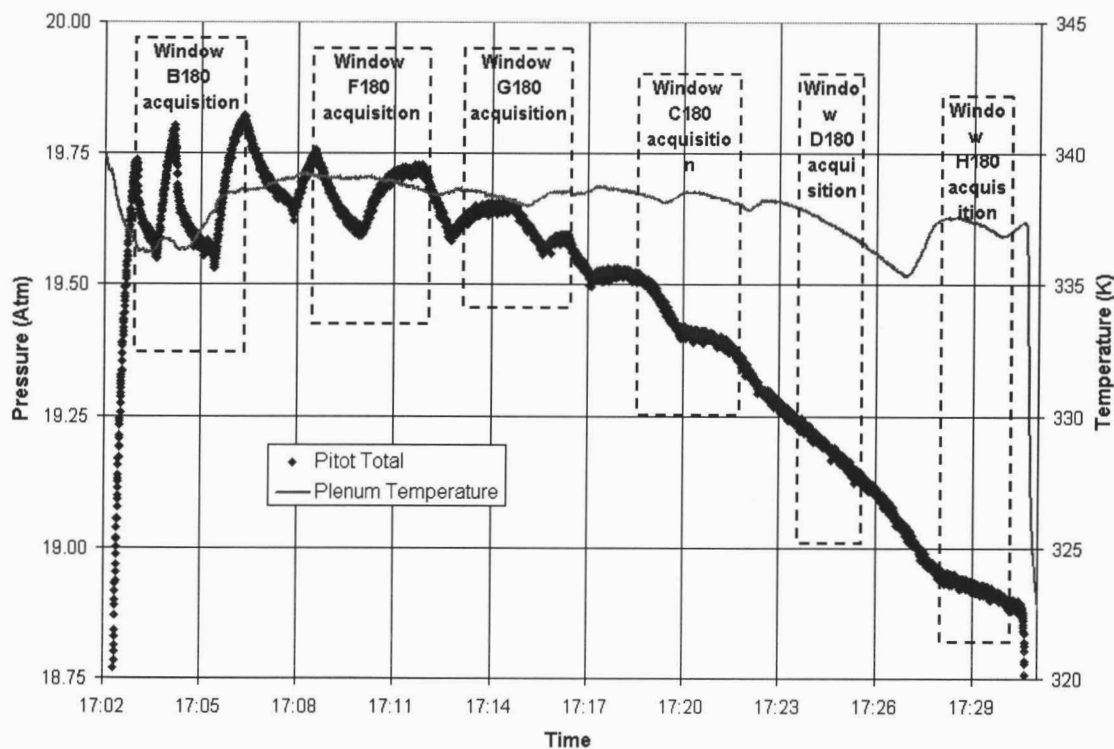
Figure 15. Bell Nozzle Inlet Conditions During Run 55.

HFA Nozzle Set Points

The intended nozzle set points for the HFA data acquisition runs were the same as the PIV data acquisition runs. The nozzle inlet conditions maintained during the HFA runs were very similar to those shown above for the PIV runs.

2.4.2. Static Pressure Data

All nozzle test article static pressures were acquired on a Pressure Systems, Inc. (PSI) Model 780B pressure scanner. The specifics of the data system are discussed in Section 2.3.1. All PSI channels were referenced to atmosphere, except nozzle inlet P_{total}. Nozzle inlet P_{static} was acquired on a 34atm module and P_{total} was acquired on the 1atm-differential module but referenced to nozzle inlet P_{static} instead of atmosphere.

All pressure measurements made on the PSI hardware had a manufacturer quoted uncertainty of 0.15% of the full scale output of the modules they were measured on. PSI module noise levels are periodically verified to be within the manufacturer quoted values. The modules used for each static pressure measurement are given below.

- Nozzle Base 1A through Nozzle Base 2C and Nozzle Inlet P_{total} were acquired on 1atm-differential modules.
- PS1-SR-6 through PS1-SR-18 & PS1-SR-24 through PS1-SR-36 were acquired on 3atm-differential modules.
- PS2-SR-01 through PS2-SR-05 and PS2-SR-19 through PS2-SR-23 were acquired on 6.8atm-differential modules.
- PS3-SR-37 through PS3-SR-39 and P_{static} were acquired on 34atm-differential modules.

2.4.3. Particle Image Velocimetry Accuracy

The method used to estimate the accuracy of the PIV velocity measurements is discussed below. The repeatability of the PIV measurements is addressed in Section 3.4.4.

To estimate the accuracy of the PIV velocity measurements many parameters have to be considered. For the measurements taken in this test, the dominant source of error was non-systematic and was mainly due to the uncertainty in the determination of the average particle displacement in the interrogation area. A validated method of evaluating PIV data uncertainty from laboratory or 'ideal' test conditions is provided in Reference 2. Paraphrased, in very brief form, it is as follows.

If $\sigma(\Delta x_i)$ is the position uncertainty associated with each individual particle pair, then the accuracy of one particle's displacement estimate originating from an interrogation area containing N particles is

$$\sigma(\mu_i) = \frac{1}{N}\sqrt{\sigma^2\left(\Delta x_1\right) + \sigma^2\left(\Delta x_2\right) + \cdots} = \frac{\sigma\left(\Delta x\right)}{\sqrt{N}} \qquad \text{Eq. 1.}$$

In practical situations the camera's F-number is often reduced to a minimum to have sufficient light to detect the particles. As a result of the particle diameter, the wavelength of light, the camera's scale factor and F-number, the particle images are less than 1 pixel in diameter. If tracking one particle less than a pixel in size, it can be said the accuracy is ±0.5 pixel, or approximately that $\sigma(\Delta x) = 0.33$ pixels. As a rule of thumb, 10 particles in the interrogation area are required to have a good signal. With 10 particles, N=10 and equation 1 results in a position uncertainty of about 0.1 pixels.

An interrogation area's average particle displacement in the X and Y directions is measured in pixels, Xpix and Ypix, respectively. The magnitude of the particles displacement is

$$\text{displacement} = \sqrt{\left(Xpix^2 + Ypix^2\right)} \qquad \text{Eq. 2.}$$

The effect on PIV accuracy of the 0.1 pixels positional uncertainty on each interrogation area's average particle displacement is calculated as follows. In PIV measurement terminology, this 'accuracy' is called 'uncertainty'.

$$\text{Accuracy} = \text{Uncertainty} = 0.1 \Bigg/ \sqrt{\left(Xpix^2 + Ypix^2\right)} \qquad \text{Eq. 3.}$$

Or, in terms of a percentage uncertainty,

$$\%\text{Uncertainty} = 100 * \left(0.1 \middle/ \sqrt{\left(Xpix^2 + Ypix^2\right)} \right) \qquad \text{Eq. 4.}$$

In PIV the U and V velocity components of the flow are directly scalable from the Xpix and Ypix. Therefore, equation 4 can also be applied to quote a percent uncertainty for each velocity measurement (that is, at each interrogation area) made by the PIV system,

For these entrainment tests, when processing the data, an interrogation area of 64 x 64 pixels was selected to maximize the number of seeding particles in an interrogation area. Assuming an average of 10 particles per interrogation area would lead to an average displacement uncertainty for each interrogation area of about 0.1 pixels.

These entrainment tests did not present the laboratory or 'ideal' test conditions for PIV measurements that this 0.1 pixels positional uncertainty was based on. To compensate for this, Dr. Hammad, the Dantec Dynamics PIV expert, suggested using a more conservative 0.2 pixels average displacement uncertainty. Therefore, for these entrainment tests, an uncertainty (for each interrogation area) was calculated to gage the PIV data accuracy as follows:

$$\%\text{Uncertainty} = 100 * \left(0.2 \middle/ \sqrt{\left(Xpix^2 + Ypix^2\right)} \right) \qquad \text{Eq. 5}$$

The use of this calculated PIV uncertainty is discussed in Sections 3.4.1.2.2 and 3.4.2.2.2 of this report.

2.4.4. Hot Film Anemometry Uncertainty

Two HFA probes were used and both were calibrated for two velocity ranges: a 'low speed' calibration and a 'high speed' calibration. For the low speed calibration a fourth-order polynomial was utilized to fit the data. Typical accuracy is of the order of ±2% for speeds more than 1m/s. The accuracy decreases below 1m/s. At 0.1m/s the accuracy is ±8%.

For the high speed calibration the data was linearized using the King's law approach as implemented by Collis and Williams.[6] This approach has a maximum error of ~15% at the higher velocities with an average error around 8%.[7]

The first probe was used for the Stratford nozzle 180° and Bell nozzle 0 and 180° planes. Its low speed calibration range was 0.5 to 2.8m/s. Its high speed calibration range was 18.0 to 88.0m/s. Due to the limitations of the calibration hardware, there was no explicit calibration data for the 2.8 to 18.0m/s range velocities. However, the high speed calibration data could be applied all the way down to 0.5m/s and produce velocities less than 10% different from those calculated with the low speed calibration. Therefore, the low speed calibration was applied for velocities up to 3.0m/s and the high speed calibration was applied for velocities above 3.0m/s.

The second probe was used for the Stratford nozzle 0 and 90° and the Bell nozzle 90° planes. Post test data analysis determined its low speed calibration was suspect. Therefore, its high speed calibration was used for the full velocity range. Based on the comparison of the first probe's low and high speed calibrations the error introduced in the low speed range should be less than ±10%.

Another important factor in the measurement accuracy is the angular response of the hot film. The single wire probes used here are most accurate when the probe wire is normal to the velocity. If the velocity is at a 45° angle to the wire, the tangential component introduces an error, causing the reading to be higher. For regions of highly angled flow relative to the wire, the error of the component normal to the wire is estimated to be about 15% (high).

Although no rigorous stack up of the uncertainties was done the uncertainty for the HFA data, it could be as much as -10 to +15% for the HFA data. However, this is believed to be a conservative uncertainty.

3. TEST RESULTS

The experimental data acquired is discussed in this section. The data acquired consists of: schlieren images of the plume structure, laser and fog flow visualization for the Bell nozzle, wall static pressures for the Bell nozzle, particle image velocimetry for the Stratford and Bell nozzles and hot film anemometry for the Stratford and Bell nozzles.

3.1.   Schlieren Images

Schlieren images (Figure 16) were recorded of the Stratford and Bell nozzle plumes prior to modifying the test facility. The test cabin portholes were removed for these tests so that the test cabin pressure would remain close to ambient pressure. The Stratford nozzle plume is shown for nozzle inlet pressure of 10.24 atmospheres and a cabin pressure of 0.977 atmosphere. The Bell nozzle plume is shown for inlet pressure of 20.06 atmospheres and a cabin pressure of 0.978 atmosphere. The Bell nozzle did not quite flow full at this nozzle pressure ratio. The nozzle flow separated from the nozzle wall just upstream of the nozzle exit. A Mach disk is visible just downstream of the nozzle exit plane.

Figure 16. Schlieren Images of Stratford and Bell Nozzle Plumes (Flow Right to Left).

3.2.   Flow Visualization

Flow visualization is provided for the Bell nozzle. Still images from the flow visualization video are presented for three regions: first in the 0 and 180° planes - aligned with the plume flow; second, normal to the plume flow, just downstream of the nozzle exit; third, underneath the plume capture pipe. Two videos of flow visualization, for the second and third regions listed above, are included in the electronic media associated with this report.

Aligned With the Plume

Figure 17 shows the Bell nozzle with the PIV laser illuminating the seed particles in the entrained flow. These images, recorded with the facility video camera, are from a test while the seeding and laser setup were still being refined. The nozzle inlet pressure was approximately 10atm, not at the set point of 19.65atm. The entrainment over the lip of the nozzle, into the nozzle, is visible in the 0° plane.

Normal to the Plume

Figure 18 shows the hardware orientation used to record the flow visualization in a plane normal to the plume. An alternate, lower power laser was used for this flow visualization. The laser light sheet generator is visible in Figure 18, pointing south, across the plume. The laser sheet was approximately 100mm downstream of the nozzle exit. The fog generator was positioned at different times, to put fog both in the base area upstream of the nozzle (the test cabin west face) and above the test cabin. The camera was looking upstream.

Figure 19 is a still image from the video showing the nozzle, with fog going into the base area and the laser sheet illuminating the fog downstream of the nozzle. The Bell nozzle was at its set point of approximately 19.4atm. Figure 20 is nine still images from the video which presents about 0.25 seconds of the video. Filaments of entrained flow are visible. They were not symmetric, nor were they steady. The flow entrained from the base area tended to roll up into large vortices. The vortices were generally attached to the west face of the test cabin. The ring in the middle of the images is that fog which had mixed into the plume shear layer.

The video these images were taken from is five minutes long, approximately 1Gb in size and is named 'BellFlowViz.mov'.

Plume Capture Pipe

Figure 21 shows the hardware orientation used to record the flow visualization of the flow under the plume capture pipe. The flow visualization was done to illustrate the vortex in that region. The laser sheet was horizontal, about 100mm below the pipe. Figure 22 and Figure 23 are stills from the video. They show the vortex below the pipe

inlet. In Figure 22 the overhead lights are still on. The laser's illumination of the fog and vortex is visible. This vortex was attached to the floor, moved around quite a bit, but was generally just below the pipe. No other vortex was seen associated with the inlet of the plume capture pipe.

The vortex was large enough at times that it affected the downstream PIV and HFA measurements in the 180° plane. Its effect can be seen in the lower right corner of the lower image in Figure 17. That region has no fog because the vortex has pushed the fog out of the plane of the PIV laser.

The video these still images were taken from is two minutes long, 444Mb in size and is named 'CapturePipeFlowViz.mov'.
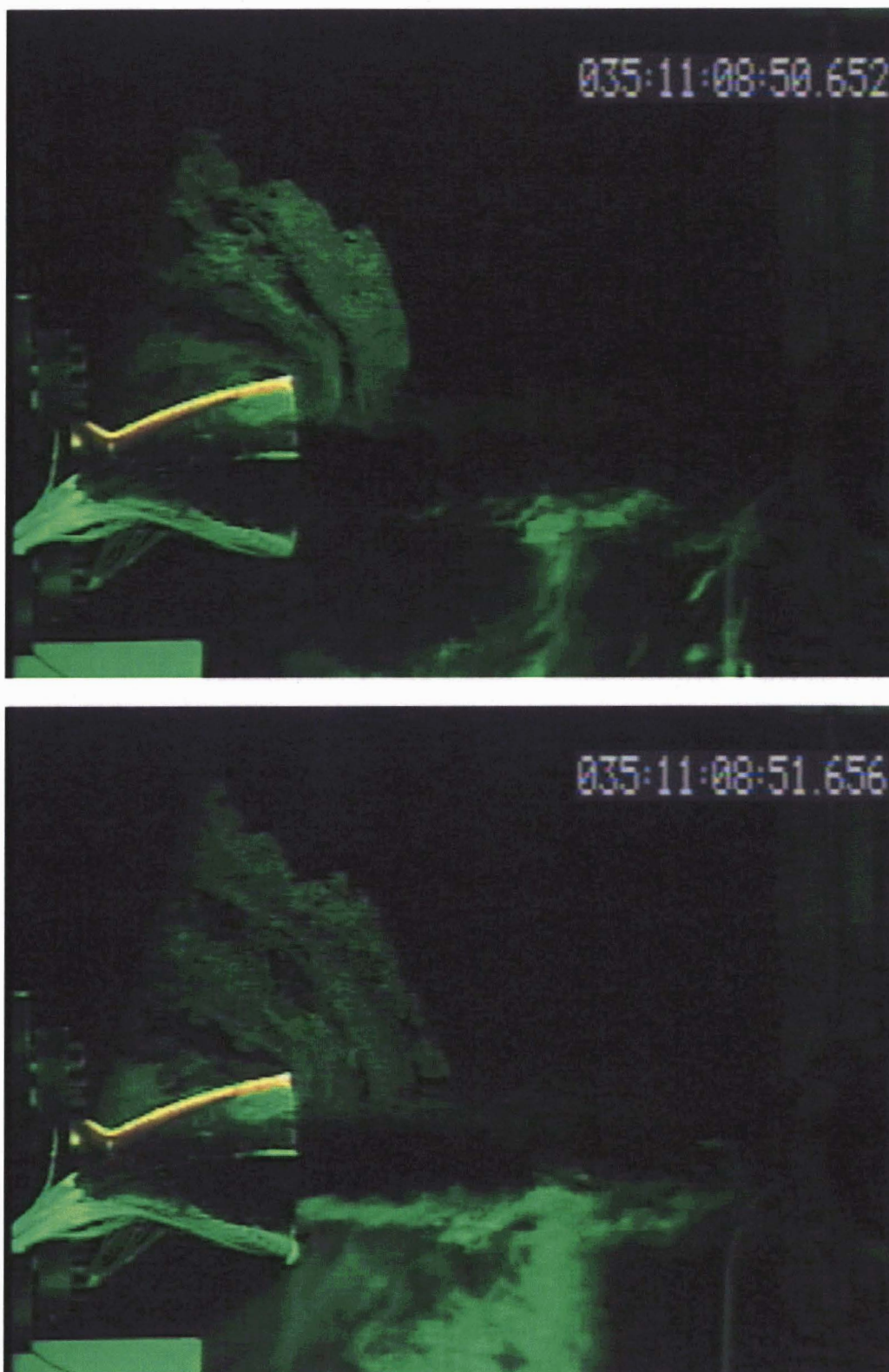
Figure 17. PIV Laser Illumination of Entrained Flow During a Diagnostic Run.
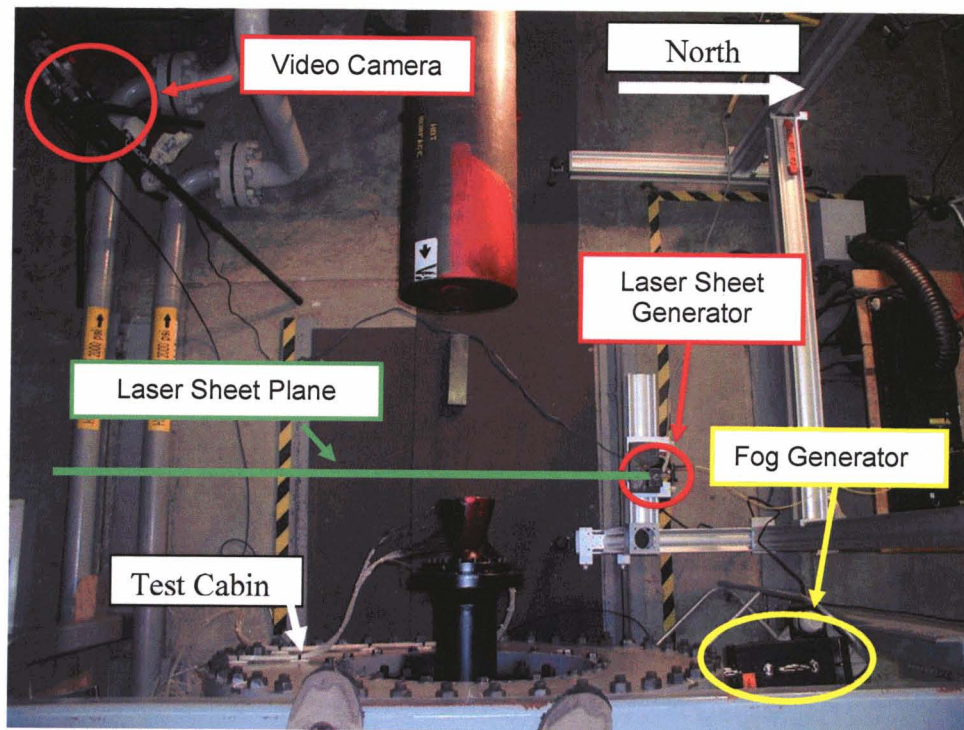
Figure 18. Setup for Flow Visualization Normal to Plume.
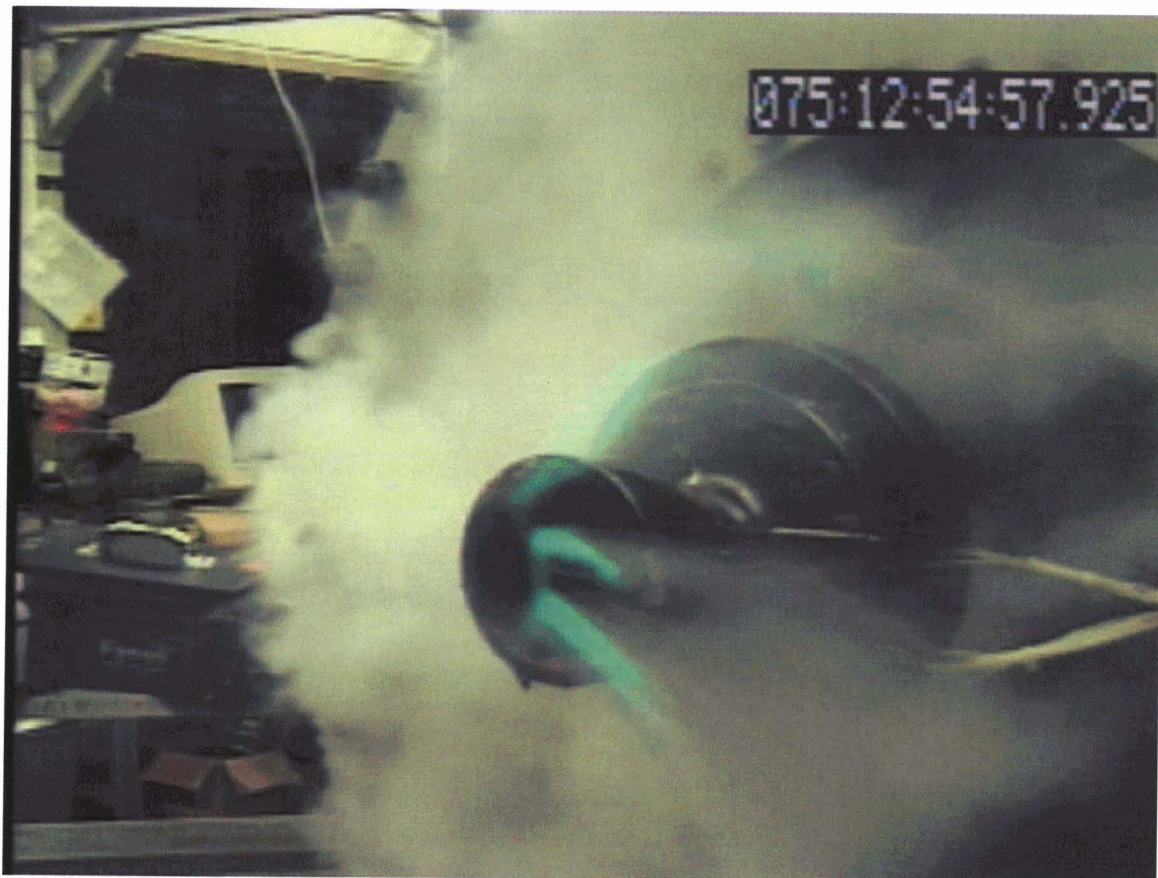
Figure 19. Flow Visualization Normal to the Plume, With Overhead Lights On.
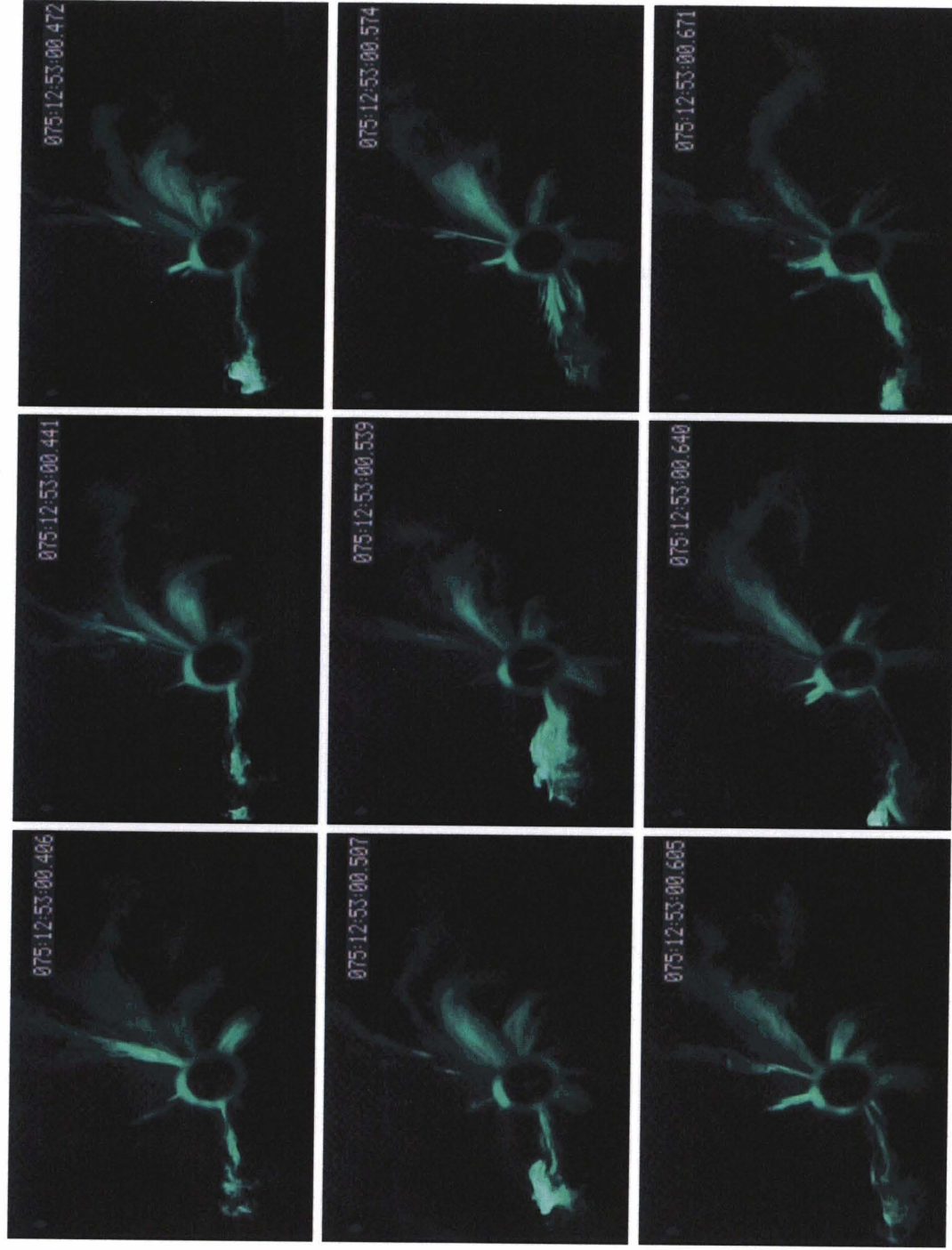
Figure 20. Nine Still Images from Video of Flow Normal to Plume.
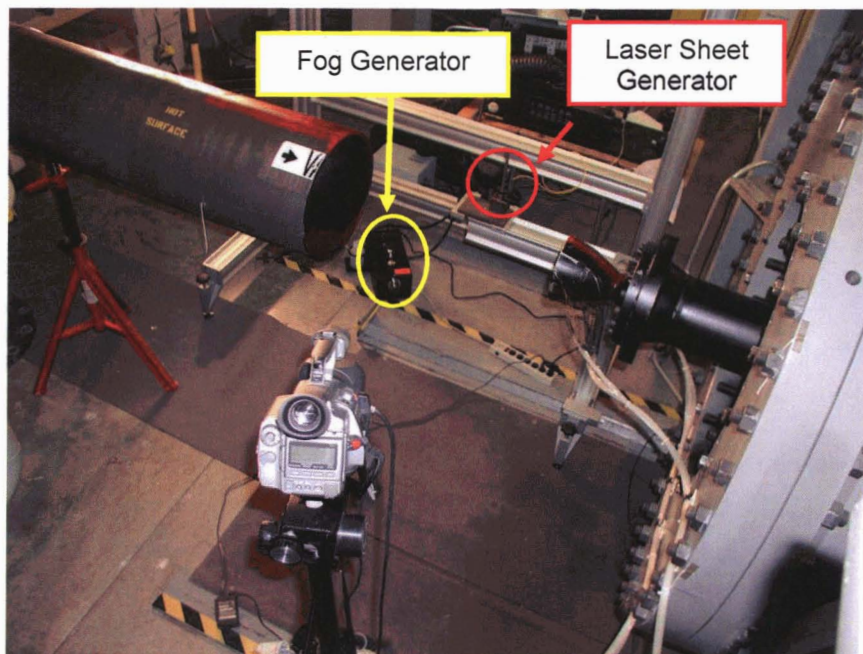
Figure 21. Setup for Flow Visualization of Flow Under the Plume Capture Pipe.

Figure 22. Flow Visualization of Flow Under the Plume Capture Pipe, With Overhead Lights On.

075:14:08:32.363

075:14:08:35.765
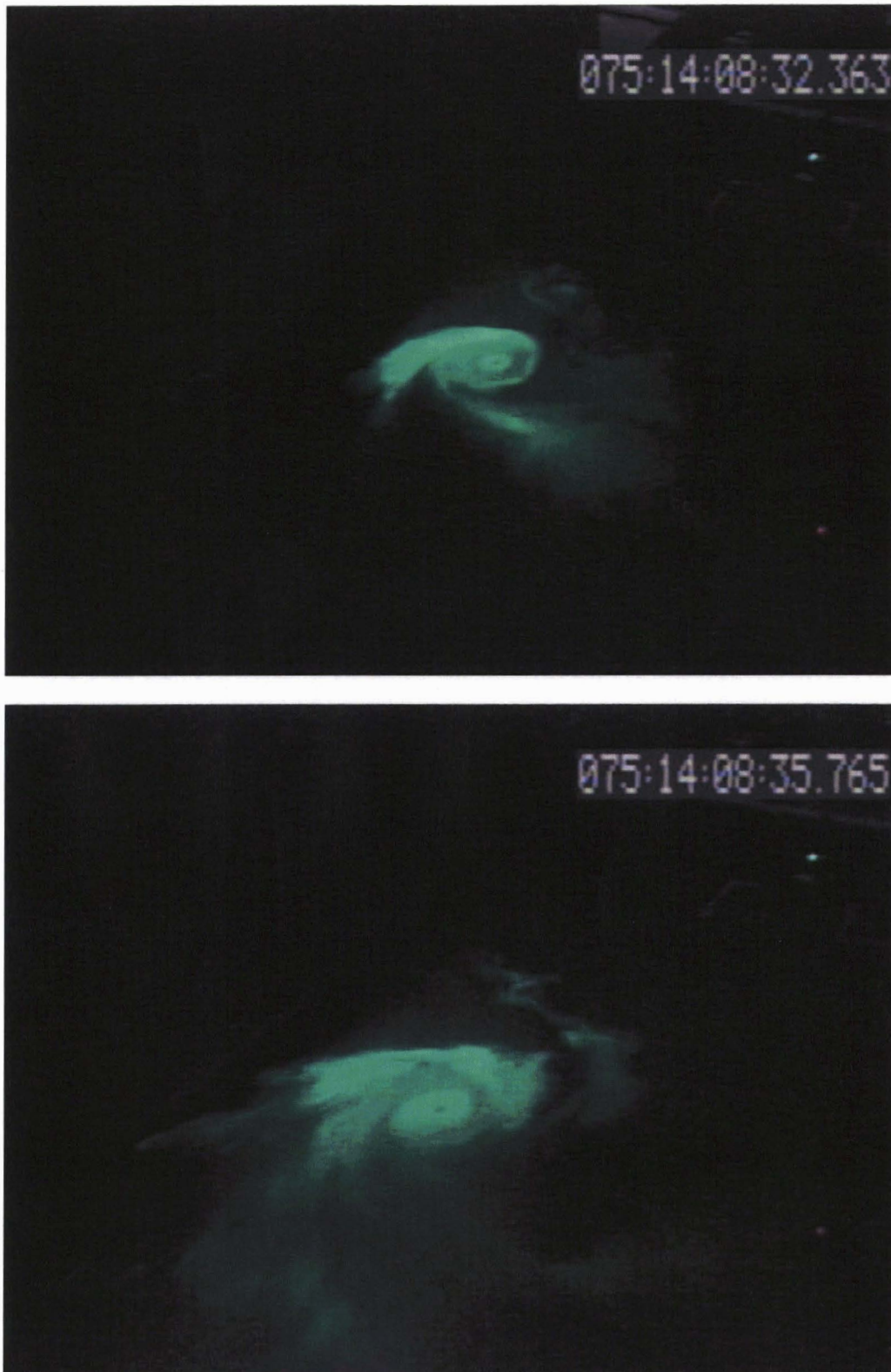
Figure 23. Two Still Images from Flow Visualization of Vortex Under the Plume Capture Pipe.

3.3.   Nozzle Wall Static Pressure Data

Figure 24 plots normalized Bell nozzle wall pressures for five nozzle pressure ratios (NPR), $P_{inlet}/P_{ambient}$. The data plotted in Figure 24 is provided in Table A4. Three of the NPRs correspond to a P_{inlet} of 19.65atm which was the average P_{inlet} during PIV data acquisition. The Bell nozzle did not flow full at the 19.65atm. The flow separated from the nozzle about 30mm upstream of the nozzle exit.

The pressure ports at X=146mm were at the nozzle exit plane, on an aft facing surface. The pressure recorded by those ports was close to ambient pressure. Note that the wall pressures in the nozzle separation were below ambient. These sub-ambient pressures induced a region of reverse flow into the nozzle. The flow entrainment near the nozzle exit was enhanced by this suction of ambient air into the nozzle.

The NPR of 19.15 corresponds to the P_{inlet} during PIV data acquisition of the H180 window. The nozzle flow was separated slightly further upstream. The NPR 10.41 corresponds to P_{inlet} of 10.27atm. This NPR was included for reference only: no entrained flowfield data was acquired for the Bell nozzle at this NPR.
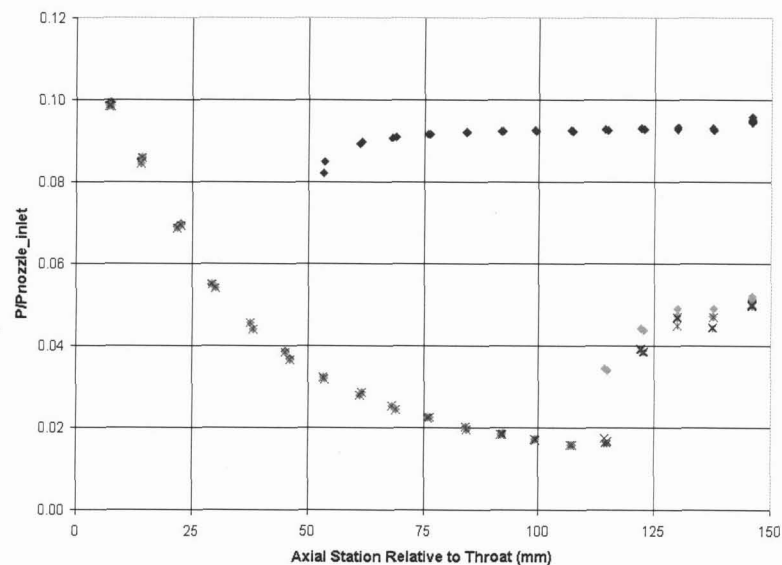
Figure 24. Normalized Bell Nozzle Wall Pressures.

3.4.   Particle Image Velocimetry Velocity Data

The PIV data for the Stratford nozzle is discussed first. The PIV data for the Bell nozzle is then discussed. The order and format in which the data are presented is very similar for both nozzles and is as follows. First, notes about the test data and the relative positions of the 'windows' are discussed. The velocity field is then discussed in two formats; 'best data without manipulation' and 'merged data files'. The first presents the best test data for the individual windows from the different delta-T datasets recorded for each window. The 'merged data files' section discusses the merging of all data in each plane into one dataset based on the PIV data uncertainty. It is this merged data that most users will find useful.

The velocity data is then presented in line plots. After discussion of the Stratford and Bell nozzle data individually, the two flowfields are compared.

3.4.1. Stratford Nozzle

3.4.1.1. Data Taken
Chronological Order with Notes from Run Logs

All the PIV data could not be taken in one run. Typically two to four windows of PIV data could be obtained in each run. The limiting factors were the position of the PIV laser sheet generator, the traversing limits of the mechanism that held the PIV camera and the NTF's supply of hot air. The Stratford nozzle PIV data were taken in the following order.

Run 40, Windows A and E
Run 41, Windows B and F
Run 42, Window C
Run 43, Window G
Run 44, Windows D and H
Run 45, Windows B180, F180 and C180
Run 46, Windows G180, D180 and H180
Run 49, Windows I and J.

For the PIV technique to work well, the test medium must be homogeneously seeded. The test medium for this entrainment experiment was the air in (and that air flowing into) the A-bay of building 4777. For the first several runs the seeding was either insufficient or poorly diffused. This marginal seeding affected windows A, E, B, F and C. Several different combinations of seeders and seeding locations were tried to correct the poor seeding. By Run 43, window G, a good location was found for the seeder. Another factor influencing the seeding quality was the window in the south wall (see Section 2.2.2) of the A-bay. This window was covered with a loose fitting tarp (starting with window G), significantly reducing the air flow through it. At that point the quality of the seeding was much improved and difference in the quality of the PIV data after these changes is visible in the contour plots shown in the following section, Section 3.4.1.2.

For Run 45, the rollup door on the west end of building 4777 was not opened. This was an oversight. This does not appear to have affected the data in windows B180, F180 and C180.

Delta-T Interval Matrix and File Naming Convention

The term 'window' refers to a region in space in which data was collected. This region was function of the camera's field of view (FOV). The term 'dataset' refers to a set of PIV data recorded at a specific delta-T in a window. Multiple PIV datasets were obtained at each window. Table 3 documents the different delta-T intervals used to acquire the PIV datasets. Each of these PIV datasets is in the electronic media associated with this report.

Table 3. Matrix of Delta-Ts at Each Window and Names of the Data Files.

WINDOW	2 ms	5 ms	20 ms	50 ms	100 ms	200 ms	300 ms	500 ms
				Laser Pluse Dt				
A				Sonic A050.dat	Sonic A100.dat	Sonic A200.dat		Sonic A500.dat
B				Sonic B050.dat	Sonic B100.dat	Sonic B200.dat		Sonic B500.dat
C		Sonic C005.dat		Sonic C050.dat	Sonic C100.dat	Sonic C200.dat		Sonic C500.dat
D		Sonic D005.dat		Sonic D050.dat	Sonic D100.dat	Sonic D200.dat		Sonic D500.dat
E					Sonic E100.dat	Sonic E200.dat		Sonic E500.dat
F					Sonic F100.dat	Sonic F200.dat		Sonic F500.dat
G				Sonic G050.dat	Sonic G100.dat	Sonic G200.dat		Sonic G500.dat
H			Sonic D020.dat	Sonic H050.dat	Sonic H100.dat	Sonic H200.dat		Sonic H500.dat
K								
B180		Sonic B180005.dat		Sonic B180050.dat	Sonic B180100.dat	Sonic B180200.dat		Sonic B180500.dat
C180		Sonic C180005.dat		Sonic C180050.dat	Sonic C180100.dat	Sonic C180200.dat		Sonic C180500.dat
D180	Sonic D180002.dat	Sonic D180005.dat		Sonic D180050.dat	Sonic D180100.dat	Sonic D180200.dat		Sonic D180500.dat
F180					Sonic F180100.dat	Sonic F180200.dat		Sonic F180500.dat
G180					SonicG180100.dat	SonicG180200.dat		SonicG180500.dat
H180					Sonic H180100.dat	Sonic H180200.dat		Sonic H180500.dat
I			Sonic I020.dat	Sonic I050.dat	Sonic I100.dat	Sonic I200.dat		Sonic I500.dat
J					Sonic J100.dat	Sonic J200.dat		Sonic J500.dat

Relative and Absolute Positions of PIV Windows

A schematic of the windows in which PIV datasets were recorded is shown in Figure 25. Eight windows of PIV data were obtained above the nozzle in the 0° plane. Two windows were obtained above the plume capture pipe. Six windows of PIV data were obtained below the nozzle in the 180° plane.

The position of the nozzle in the camera's FOV in the A and B and B180 windows was used to determine the coordinate transformations required to locate windows A and B180 in the nozzle global coordinate system of the Stratford nozzle. (Note that the Stratford and Bell nozzle global coordinate systems are different). The data from the rest of the windows in the 0° and 180° planes were then translated relative to the A and B180 windows based on the commands sent to the traversing mechanism.

The position of the plume capture pipe in the camera's FOV in the I window was used to determine the coordinate transformations required to locate I in the coordinate system of the pipe. Window J's data was then translated relative to I based on the commands sent to the traversing mechanism.

The translations for all windows are provided in Table 4. These translations were applied to the coordinate system of the datasets for each window. Each window's datasets consist of a matrix of 36 by 49 data points. The origin of the coordinate system of each window's data points is that window's lower left hand corner. The fifth and sixth columns in each dataset file (Table 3) are the X and Y positions (in mm) of each data point within that window's datasets. The translations given in Table 4 were applied to these X-Y coordinates to position each window's datasets in the Stratford nozzle's global coordinate system.

The coordinate systems within the datasets in the 0° plane are identical. That is, the matrix of X-Y locations within the datasets relative to the windows' origin is the same. Likewise all datasets in the 180° plane have the same matrix of X-Y points. There are slight differences between the 0° and 180° planes. See notes in Table 4 for details.

Table 4. Window Coordinate Transformations for Stratford Nozzle PIV Data.

Stratford Nozzle PIV Data Window Coordinate Transformations and Resulting Global Coordinates's

General Notes
Global Origin is at nozzle exit on nozzle centerline
All dimensions are in millimeters
The nozzle outer lip radii is 20.33 mm

Notes for the 0degree Plane
Windows A through H are 133.351 mm wide by 180.2 mm tall

The origin of A was 129.184mm to left of nozzle exit plane
B & F were 110 mm to right of A & E. C & G were 110 mm to right of B & F. D & H were 90 mm to right of C & G.
The bottom of A through D was 15.32mm below the nozzle lip.
E through H were 155 mm above A through D.

Window Name	E X	E Y	F X	F Y	G X	G Y	H X	H Y
Translations	-129.184	-15.60 +20.334 +155	-129.184 +110	-15.60 +20.334 +155	-129.184 +110 +110	-15.60 +20.334 +155	-129.184 +110 +110 +90	-15.60 +20.334 +155
Total Translation	-129.184	159.734	-19.184	159.734	90.816	159.734	180.816	159.734
Global Coordinates	-129.184 to 4.167	159.73 to 339.93	-19.184 to 114.167	159.73 to 339.93	90.816 to 224.167	159.73 to 339.93	180.816 to 314.167	159.73 to 339.93

Window Name	A X	A Y	B X	B Y	C X	C Y	D X	D Y
Translations	-129.184	-15.60 +20.334	-129.184 +110	-15.60 +20.334	-129.184 +110 +110	-15.60 +20.334	-129.184 +110 +110 +90	-15.60 +20.334
Total Translation	-129.184	4.734	-19.184	4.734	90.816	4.734	180.816	4.734
Global Coordinates	-129.184 to 4.167	4.73 to 184.93	-19.184 to 114.167	4.73 to 184.93	90.816 to 224.167	4.73 to 184.93	180.816 to 314.167	4.73 to 184.93

Window Name	B180 X	B180 Y	C180 X	C180 Y	D180 X	D180 Y
Translations	-13.66	-170.9 -20.334	-13.66 +110	-170.9 -20.334	-13.66 +110 + 90	-170.9 -20.334
Total Translation	-13.660	-191.234	96.340	-191.234	186.340	-191.234
Global Coordinates	-13.66 to 118.8	-12.24 to -191.237	96.34 to 228.8	-12.24 to -191.237	186.34 to 318.8	-12.24 to -191.237

Window Name	F180 X	F180 Y	G180 X	G180 Y	H180 X	H180 Y
Translations	-13.66	-170.9 -20.334 -155	-13.66 +110	-170.9 -20.334 155	-13.66 +110 + 90	-170.9 -20.334 155
Total Translation	-13.660	-346.234	96.340	-346.234	186.340	-346.234
Global Coordinates	-13.66 to 118.8	-167.24 to -346.23	96.34 to 228.8	-167.24 to -346.23	186.34 to 318.8	-167.24 to -346.23

Notes for 180degree Plane
Windows B180 through H180 are 132.4579 mm wide by 178.997 mm tall
The origin of B180 was 14.7 mm to left of nozzle exit plane
C180 & G180 were 110 mm to right of B180 & F180. D180, H180 were 90 mm to right of C180 & G180.

The bottom of B180 through D180's was 160.3 mm below the nozzle lower lip.
F180 through H180 were 155 mm below B180 through D180.

Notes for I and J Data
The origin of I was 84.118mm from pipe entrance
J is 110mm right of I

Pipe OD is 330.2 mm

Pipe wall thickness is 9.525mm

Window Name	I X'	I Y'	J X'	J Y'
Translations	-89.448	-32.68 +174.625	-89.448 +110	-32.68 +174.625
Total Translation	-89.448	141.945	20.552	141.945
Global Coordinates	-89.448 to 221.026	141.945 to 319.745	199.448 to 331.026	141.945 to 319.745
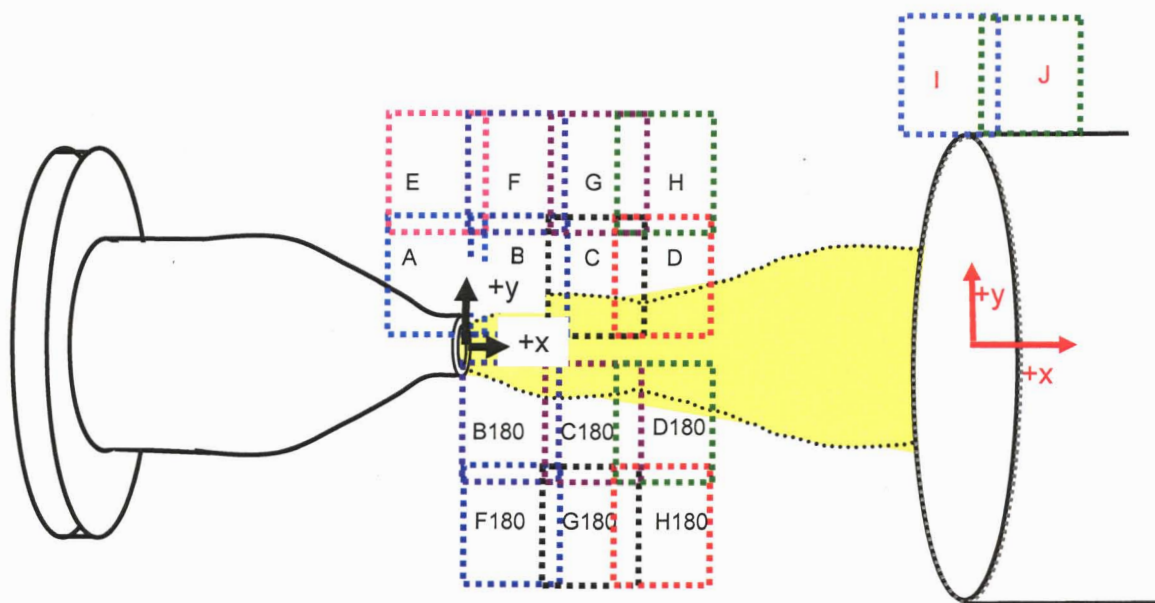
Figure 25. Schematic of PIV Windows for the Stratford Nozzle.

3.4.1.2. Velocity Field Discussion

The velocity data is presented in two forms. First, the best dataset for each window, without modification of the datasets, is presented. Second, a single dataset created from the best data available from datasets of all windows, is presented.

3.4.1.2.1. Best Data Without Manipulation

Table 3 lists the different delta-Ts used to acquire data for each PIV window. The smaller delta-T's resolved higher velocities better than the larger delta-T's. Figure 26 illustrates this. The 50 microsecond delta-T resolved higher velocities close to the nozzle exit and in the plume shear layer. However, the smaller delta-Ts have higher uncertainty in the low velocity regions as illustrated in Figure 27.

Of the data recorded, it was judged that the best representation of the flowfield (without modification of the datasets) is captured by the 100 microsecond delta-T dataset for windows A to D and B180 to D180 and 200 microsecond delta-T dataset for windows E to K and F180 to H180. Figure 28 presents these datasets. Note in these TecPlot® images that the overlapped regions of adjacent windows are plotted, but only the window that is in 'on top' is visible.

The datasets in Figure 28 are the best compromise between capturing the high velocity regions, acceptable uncertainty levels and smooth velocity gradients between adjacent windows. These datasets show the high velocity near the nozzle exit and the general acceleration of the entrained flow with axial position. The seeding was less than optimum for windows A, B, C, E and F and the resulting PIV data is of reduced quality for those windows. Window C was particularly difficult to get good seeding and that data has obvious discontinuities with its neighboring windows. The seeding was adequate for windows D, G, and H in the 0° plane and for all the 180° windows. The PIV data in those windows appears to be better quality data.

The character of the flow is symmetric. The PIV data indicates the 180° plane had higher peak velocities near the nozzle exit. This was probably caused more by the poor seeding in the A and B windows than by real physics.

The indicated low velocity near the centerline is the plume flow. The velocity was not measurable with the delta-Ts presented here. Also, the plume was not seeded as the intent of the test was to measure the entrained flow. The apparent low velocity region at the outer edge of E to H is discussed in Section 3.4.3.
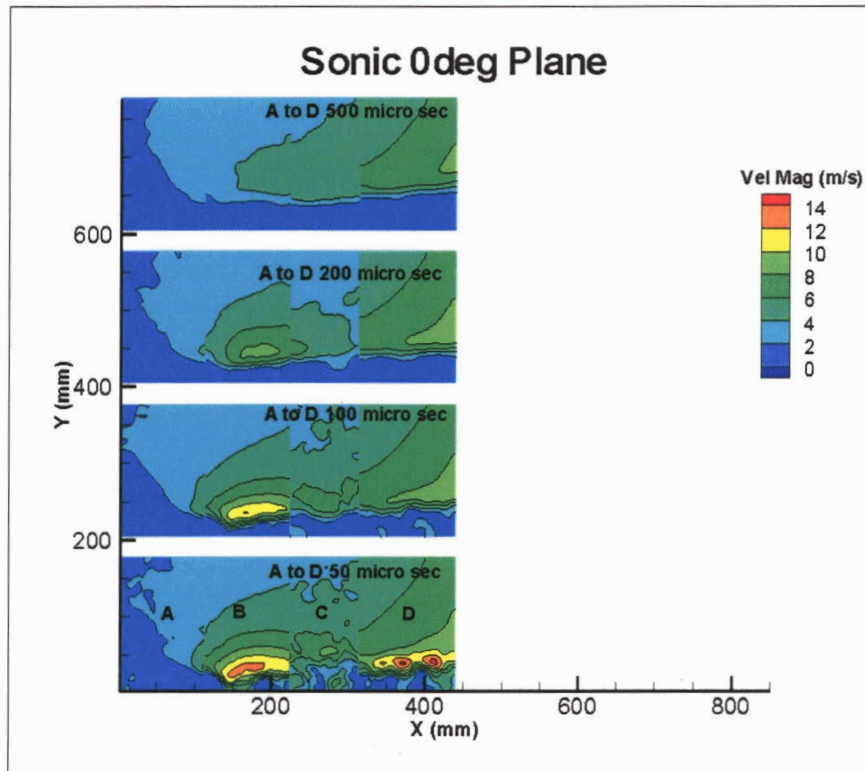
Figure 26. Velocities Resolved with Different Delta-Ts.
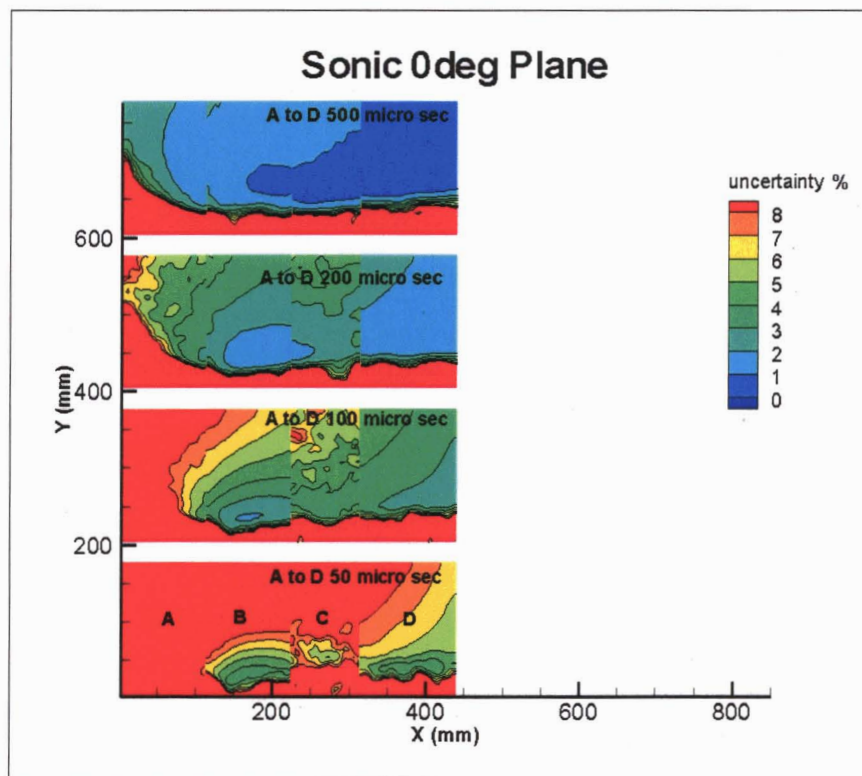
Figure 27. Uncertainty Resulting from Different Delta-Ts.
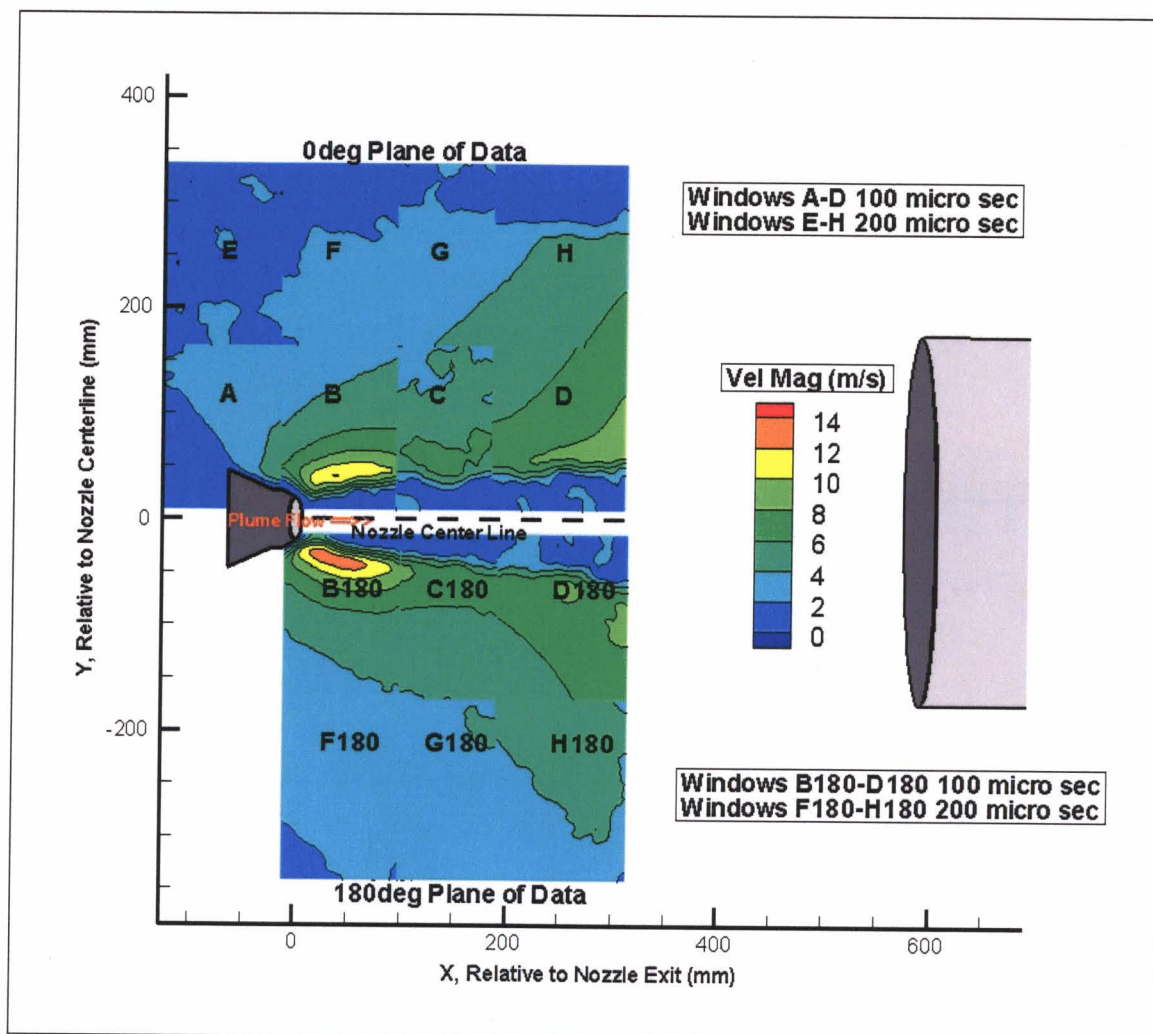
Figure 28. Best Representation of Stratford Nozzle Entrainment Flowfield without Modification of the PIV Datasets.

3.4.1.2.2. Merged Data Files

Velocity Contour Plots

A more accurate representation of the entrained flow was created by combining the data from the multiple delta-T datasets available for each window. The high velocity regions from the small delta-T datasets were 'merged' into the larger delta-T datasets that captured the general entrained flowfield better. Merging of multiple delta-T datasets was only required for the inner row of windows (A to D and B180 to D180) where there were large gradients in measured velocity.

Figure 26 and Figure 27 are used to explain the merging of multiple delta-T datasets. These two figures show that the 50 microsecond delta-T resolved higher velocity near the nozzle exit and in the nozzle shear layer with relatively low uncertainties. If one were willing to accept 8% uncertainty (Figure 27), much of the 50 microsecond delta-T dataset is acceptable near the plume shear layer and nozzle exit. These higher velocities were incorporated into the merged data shown in Figure 29.

The merging was done by assessing the data, point by point. The logic for merging was that the data from the smallest delta-T dataset was used if the uncertainty at that data point was 'acceptable' – in this example – an uncertainty of less than 8%. Because the calculation of the PIV data uncertainty is somewhat subjective (as described in Section 2.4.3), an uncertainty was chosen that resulted in a fairly continuous velocity flowfield. For the Stratford nozzle data, 8% uncertainty was deemed a good compromise between accuracy and resolution of the flowfield. Lower uncertainty levels (2 and 5% were assessed) resulted in noticeable flowfield discontinuities or flowfields that failed to capture the higher velocities near the plume shear layer and nozzle exit.

The merging of data within each window was done in an Excel spreadsheet. These Excel files are provided in the electronic media associated with this report. The structure of these files is discussed in Section 3.4.6. If an alternate uncertainty is desired, these files can be manipulated to produce merged data with the alternate uncertainty as the criterion.

After the data was merged within each window, the merged data were then joined or 'woven' together (by sorting on the radial and axial stations in the spreadsheet). Thus, creating a single data field that encompassed all of windows A to F (Figure 29) and a second that encompassed windows B180 to H180 (Figure 31). These woven data fields allow the overlapped regions to be seen when plotting contours in TecPlot®. They also enable extracting line plots through the entire flowfield. (See Section 3.4.6 for discussion of the Excel files).

To clarify the terminology used here: 'merged' means that data from multiple delta-T datasets were evaluated point by point to determine the best value to use at each data point in a window. 'Woven' means that the data points from multiple windows were reordered into one contiguous data field for plotting.

Figure 29 and Figure 31 show that the resulting merged and woven PIV data resulted in fairly continuous flowfields. In these velocity contours, the saw tooth patterns indicate velocity discontinuities in the overlapped regions of adjacent windows. The relatively poor quality of the measurements in the C window is evident by the saw tooth patterns surrounding it. The 180° plane had much better agreement window to window and in general appears to be a better set of data than the 0° plane.

Figure 30 and Figure 32 show the corresponding uncertainties. In the uncertainty plots, the strong gradients between the inner and outer rows of windows are due to the different delta-Ts and are not a result of velocity discontinuities. Note the uncertainties near the centerline are acceptable for windows D, B180, C180 and D180. This is because those windows had delta-Ts of 2 and 5 microseconds and sufficient seed particles had diffused into the plume shear layer. Also note the band of greater than 8% uncertainty (in Figure 30) along the top of the 0° plane data. This phenomenon is related to the apparent low velocities in this same area (see Figure 29) and is discussed in Section 3.4.3.

Merged and woven data for the 0° and 180° planes are shown together in Figure 33. Again, the general character of the 0° and 180° planes agree. The 180° plane appears more continuous than the 0° plane and indicates higher velocities near the nozzle exit.

The contours in Figure 33 show there were two regions where the entrained flow was accelerated. These regions of acceleration indicate the location of the flow phenomena that induced the entrained flow. There was a distinct acceleration of the entrained flow near the nozzle exit, and a second more gradual acceleration, with axial station, of the entire entrained flowfield.

Figure 34 shows the velocity vectors in the flowfield near the nozzle exit. The vectors are not scaled by their magnitude.
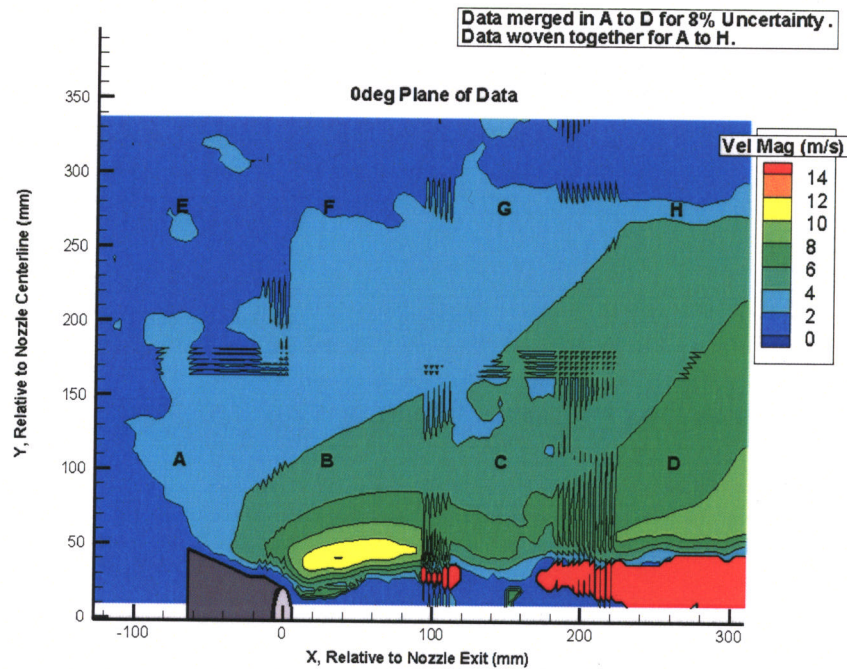
Figure 29. Merged and Woven PIV Velocity for 0° Plane for the Stratford Nozzle.
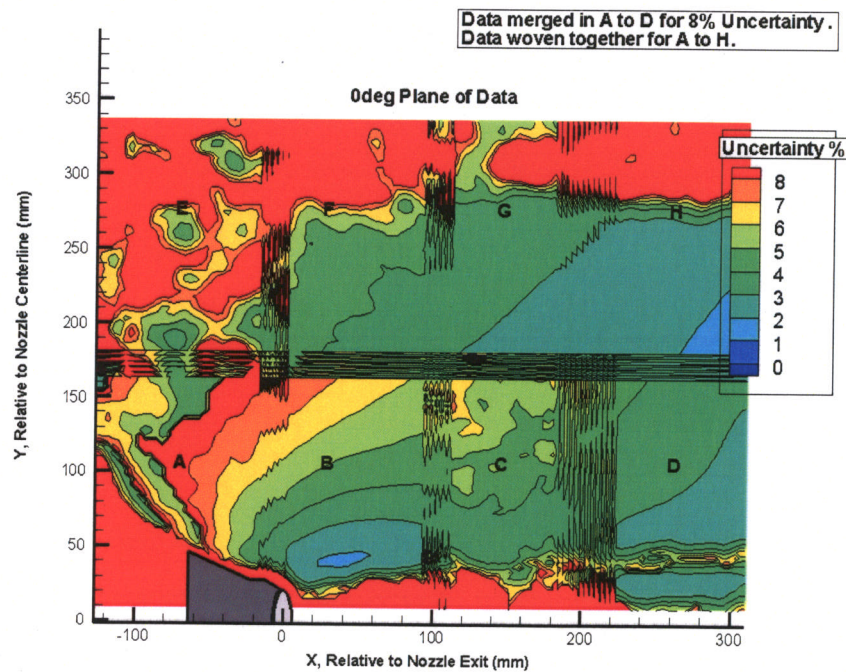
Figure 30. Uncertainty for the Merged and Woven PIV Data for 0° Plane for the
Stratford Nozzle.
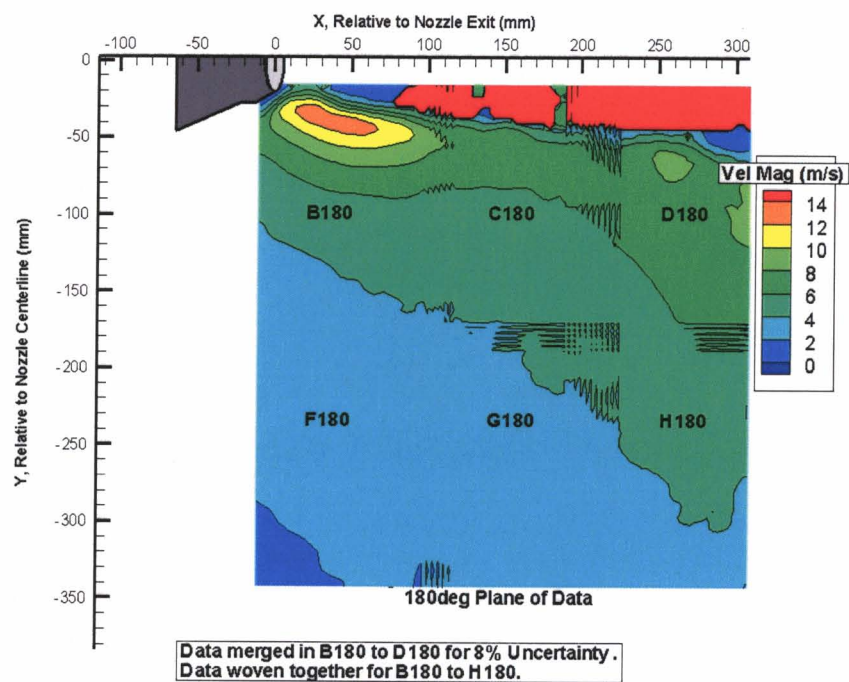
Figure 31. Merged and Woven PIV Velocity for 180° Plane for the Stratford Nozzle.
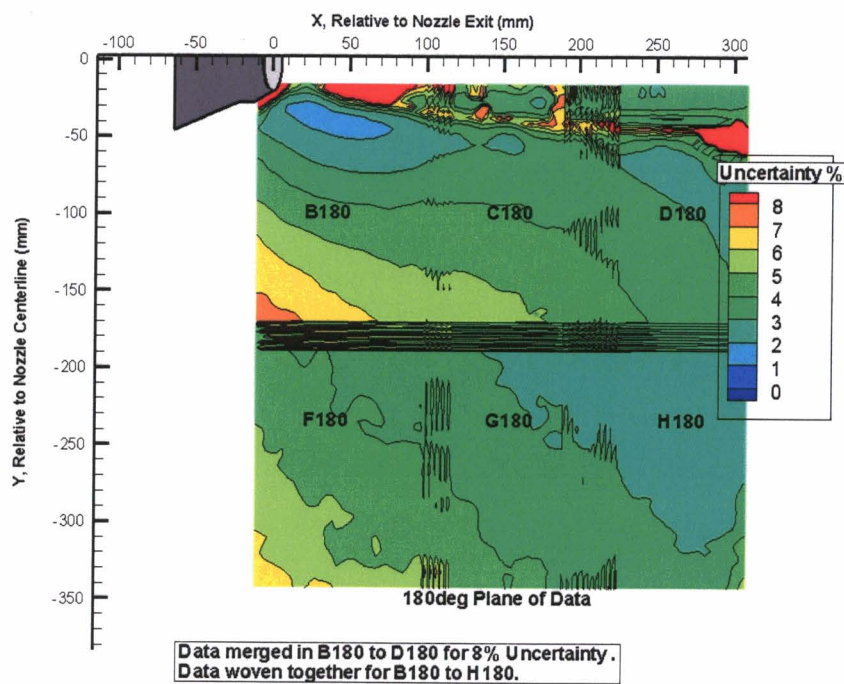
Figure 32. Uncertainties for Merged and Woven PIV Data for 180° Plane for the
Stratford Nozzle.
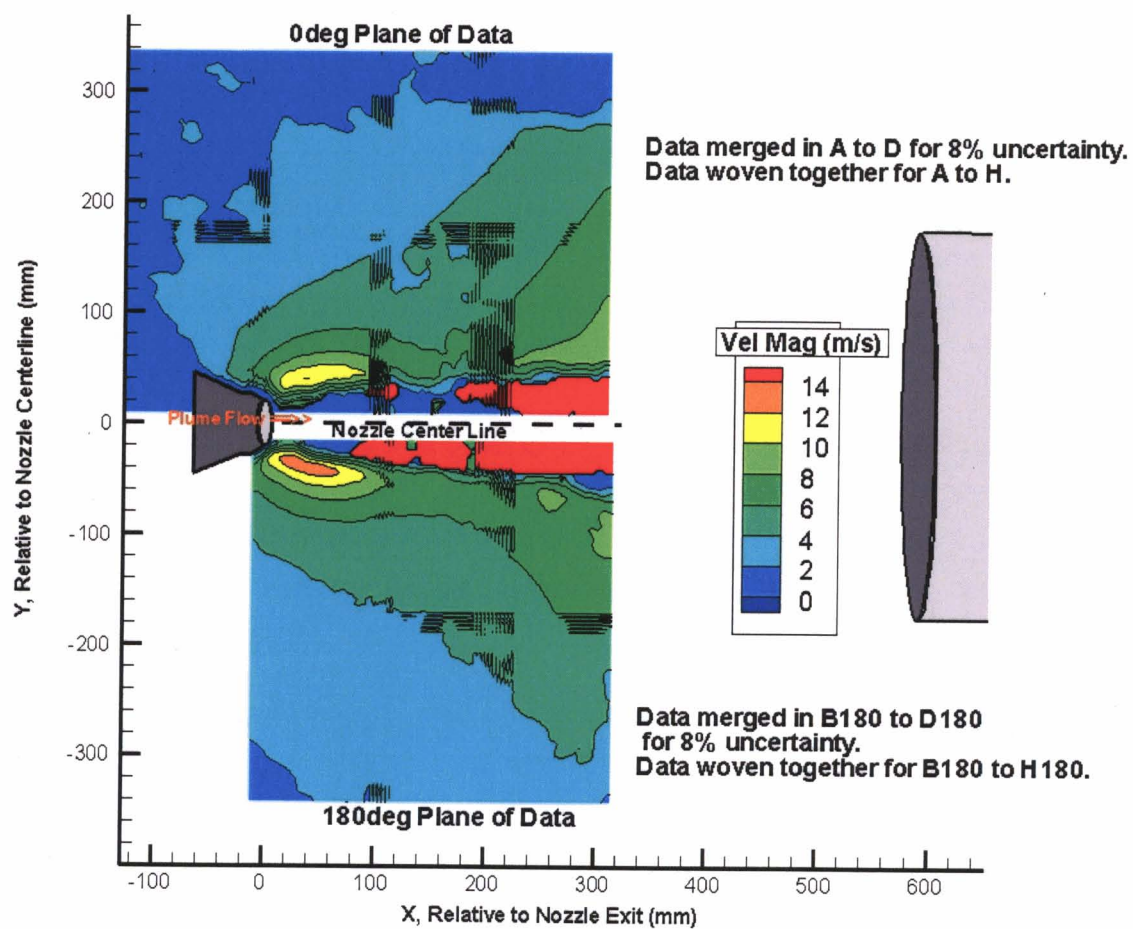
Figure 33. Merged and Woven PIV Velocity for Stratford Nozzle.
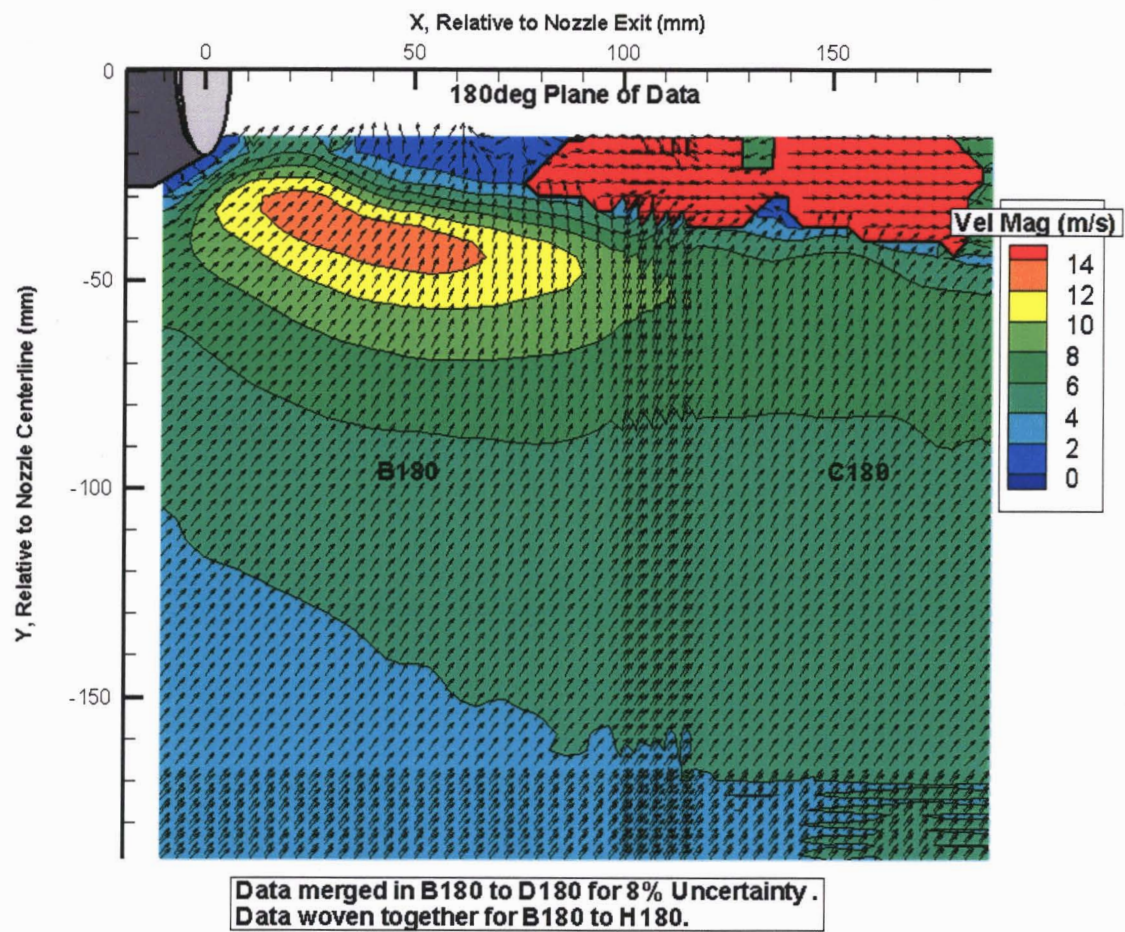
Figure 34. Velocity Vectors from the Merged and Woven PIV Data for the Stratford Nozzle.

Velocity Line Plots

Line plots of velocities at constant radial and axial stations are now discussed to illustrate some of the flowfield characteristics. The radial and axial stations for these line plots are shown in Figure 35. These plots were created in the Excel file that generated the woven data. The data plotted here can be extracted from that Excel file. The Excel file can be used to create additional line plots at alternate radial or axial stations as well.

Figure 36 and Figure 37 show the velocities at five constant radial stations from the merged and woven data in the 0° and 180° planes. The saw tooth patterns in the lines are the overlapping regions of adjacent windows. In Figure 36 the C window data is inconsistent with its neighbors and should be disregarded. The C180 window data in Figure 37 indicates the velocity plots should be smooth across windows B, C and D. The zero velocities in window A of Figure 36 is where those radial stations intersect the nozzle hardware.

These velocity line plots show, as did the velocity contour plots, that there were two regions where the entrained flow was accelerated. The first region was the strong acceleration close to the nozzle exit. The flow phenomenon inducing this acceleration was the viscous pumping of the plume shear layer. The second region of acceleration was the more general acceleration of the entire entrained flowfield with axial station. This second acceleration started at about X=125mm. The primary flow phenomena inducing this second acceleration was the sink created by the interaction of the plume and the plume capture pipe. The cause of the plume capture pipe sink is discussed in Section 3.4.1.2.3.

The peak magnitudes shown in these line plots are approximately, 11.5 and 13m/s for the 0 and 180° planes. The U-velocity component peaked about 25mm downstream of the nozzle exit (X=0mm). The V-velocity component peaked about 50mm downstream of the nozzle exit. The nozzle outer radius at the exit was 20.3mm. The acceleration near the nozzle exit is evident in the profiles out to about 134mm (Y=134mm profile not shown here), or about 114mm above the nozzle lip. The effect of the nozzle exit acceleration extended about 125mm downstream of the nozzle exit. Downstream of X~125mm the entrained flow's velocity increased due (mainly) to the plume capture pipe sink's effect.

The erratic and decreasing values of the Y=44mm profiles starting at X=100mm indicates bad data. In this region, the PIV measurements were affected by the shear layer.

Figure 38 compares three profiles for the 0 and 180° planes. They compare quite well considering the less than satisfactory seeding quality in the first windows of the 0° plane measurements.

Figure 39 and Figure 40 present the 0° plane velocities at constant axial stations. Figure 41 presents the 180° plane velocities at constant axial stations. In Figure 39, the peak velocities near the nozzle exit are illustrated. Note that the X=-100.4, -39.1 and -

1.2mm profiles intersect the nozzle hardware at their lower ends. Hence, the velocities go to zero for these profiles. The X=0.6 and 20.5mm profiles go toward zero due to the absence of seed particles in the plume. The X=-1.2 and 0.6mm profiles indicate there is not a significant difference within the overlapped region of windows A and B. As one would expect, the peak velocities increased closer to the nozzle exit.

The X=200 and ~300mm velocity profiles in Figure 40 and Figure 41 illustrate the acceleration of the bulk of the entrained flow with increasing axial station. Again, this acceleration was primarily due to the plume capture pipe sink. In Figure 40, the poor seeding in the C window was avoided by plotting the X=198.9mm profile from window D data.

Note that the velocities decreased, or trended toward zero, near the centerline – that part of the profile closest to or in the plume shear layer. One would expect the flow to be accelerated by the high velocity shear layer. However, the plume was not seeded. Therefore, any PIV measurements of the shear layer would have required some of the seed material to have diffused from the ambient air into the plume shear layer. In addition, smaller delta-Ts would be required to adequately resolve this high speed shear layer flow. Therefore, the velocities trending to zero in this region should be disregarded.

For the profiles between X=40 and 300mm the peak velocities occurred further from the nozzle centerline with increasing axial station. This was due to the increasing diameter of the plume shear layer with axial station.

The 180° plane velocities have the same general trends as the 0° plane. Figure 42 compares some of the axial profiles for both planes.
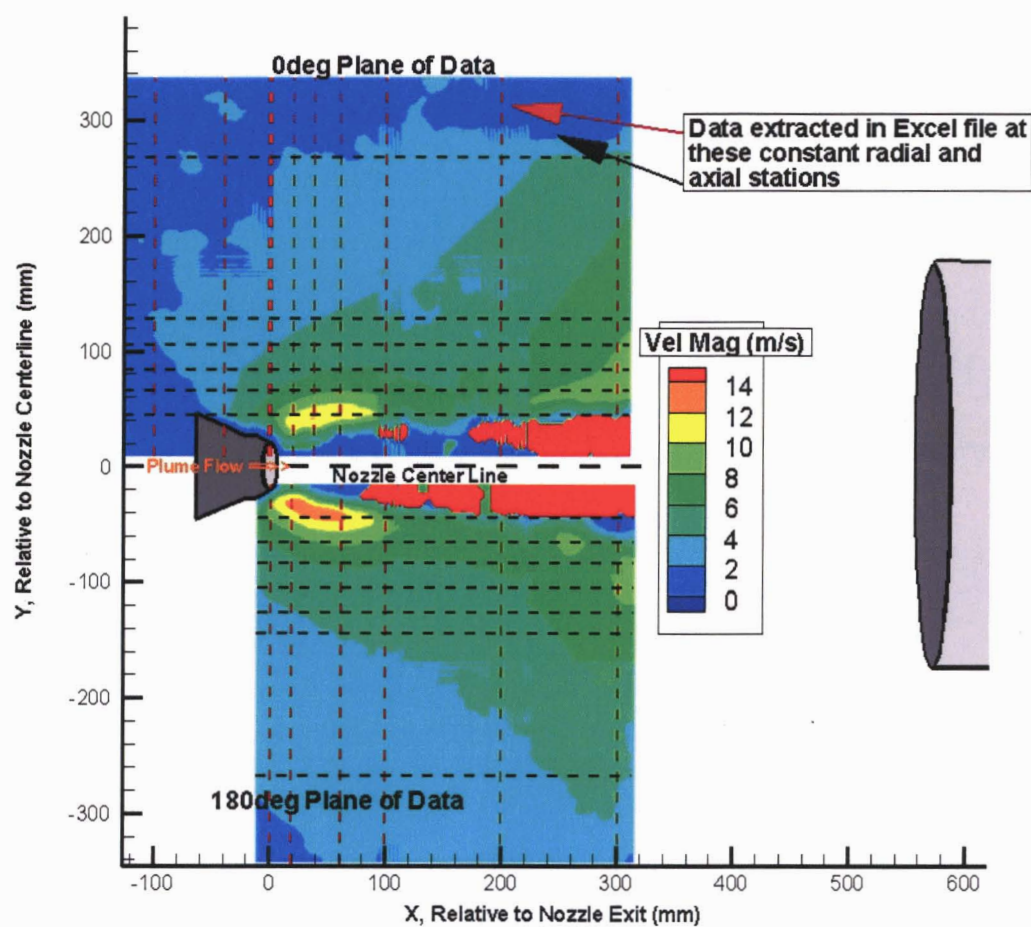
Figure 35. Axial and Radial Stations of Subsequent Velocity Profiles for the Stratford Nozzle.
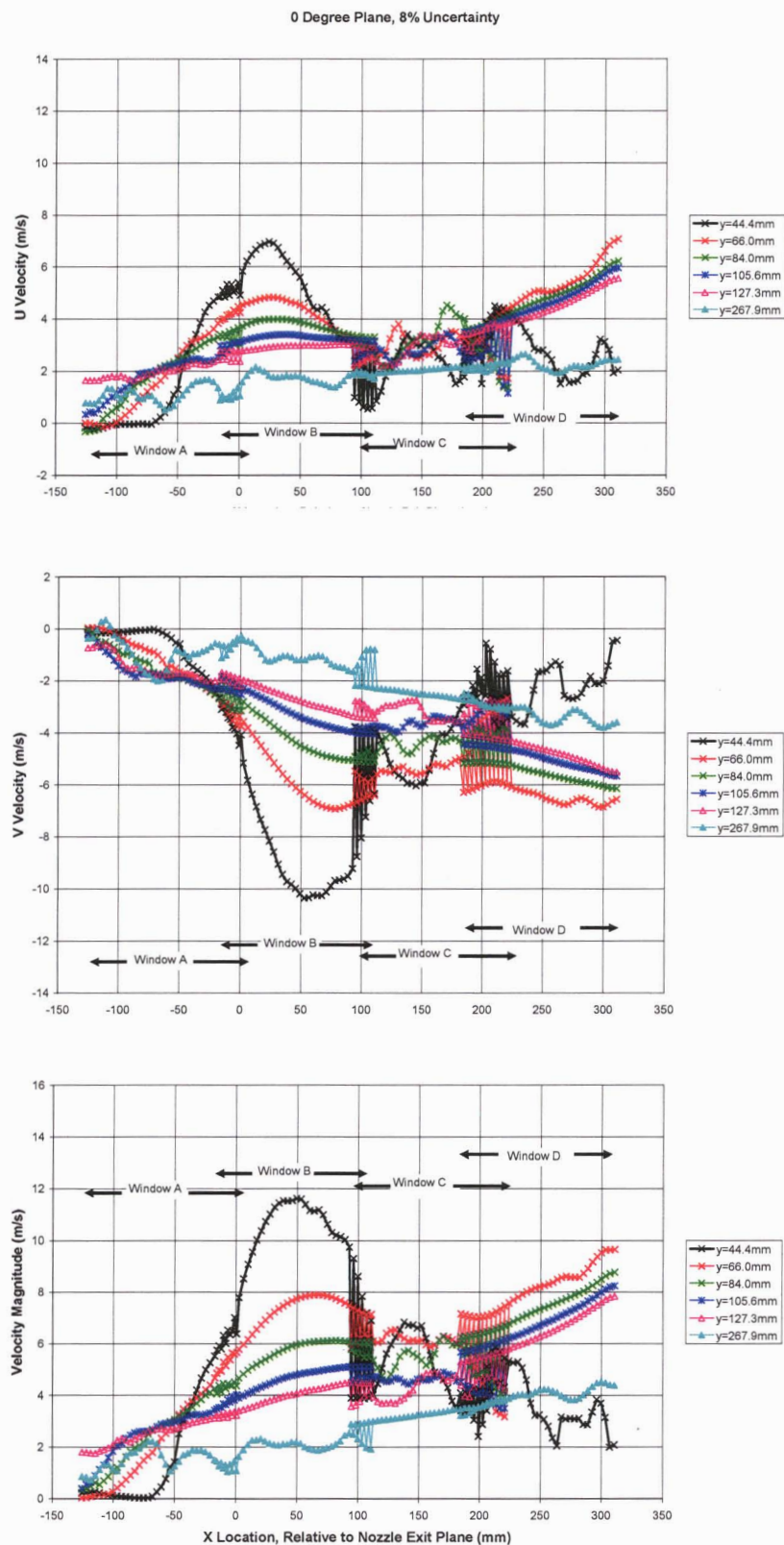
Figure 36. PIV Measured Velocities at Five Radial Stations in the 0° Plane for the Stratford Nozzle.
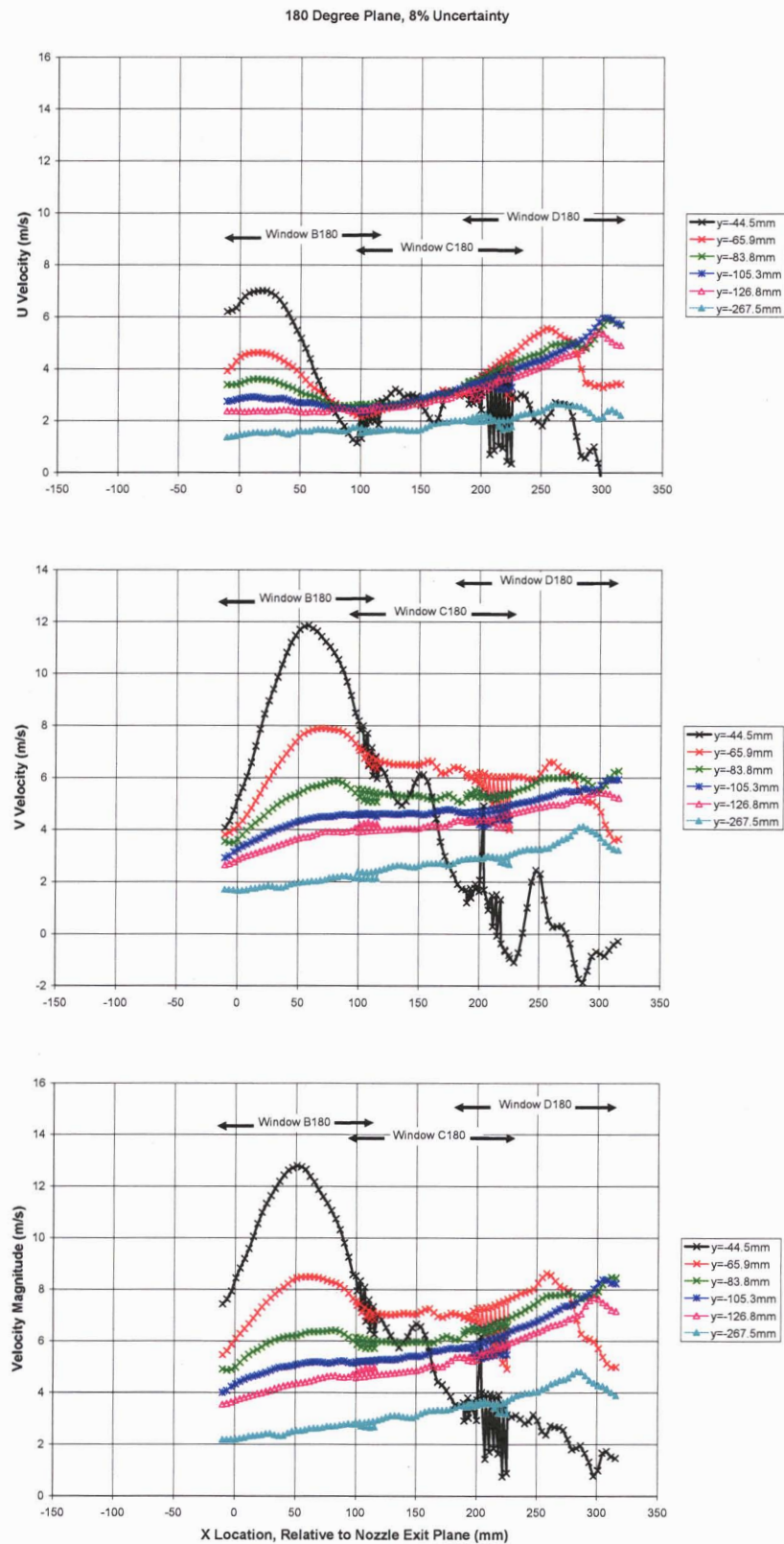
Figure 37. PIV Measured Velocities at Five Radial Stations in the 180° Plane for the
Stratford Nozzle.

0 and 180 Degree Planes, 8% Uncertainty
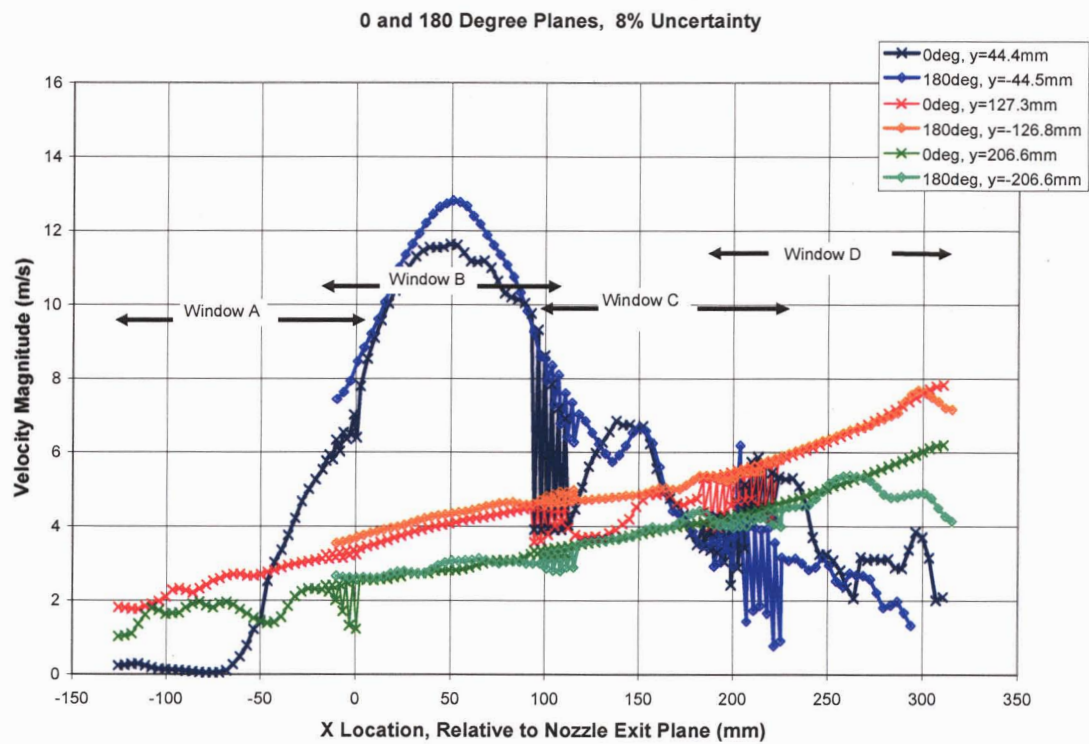
Figure 38. Comparing PIV Measured Velocities for the 0 and 180° Planes at Three Radial Stations for the Stratford Nozzle.
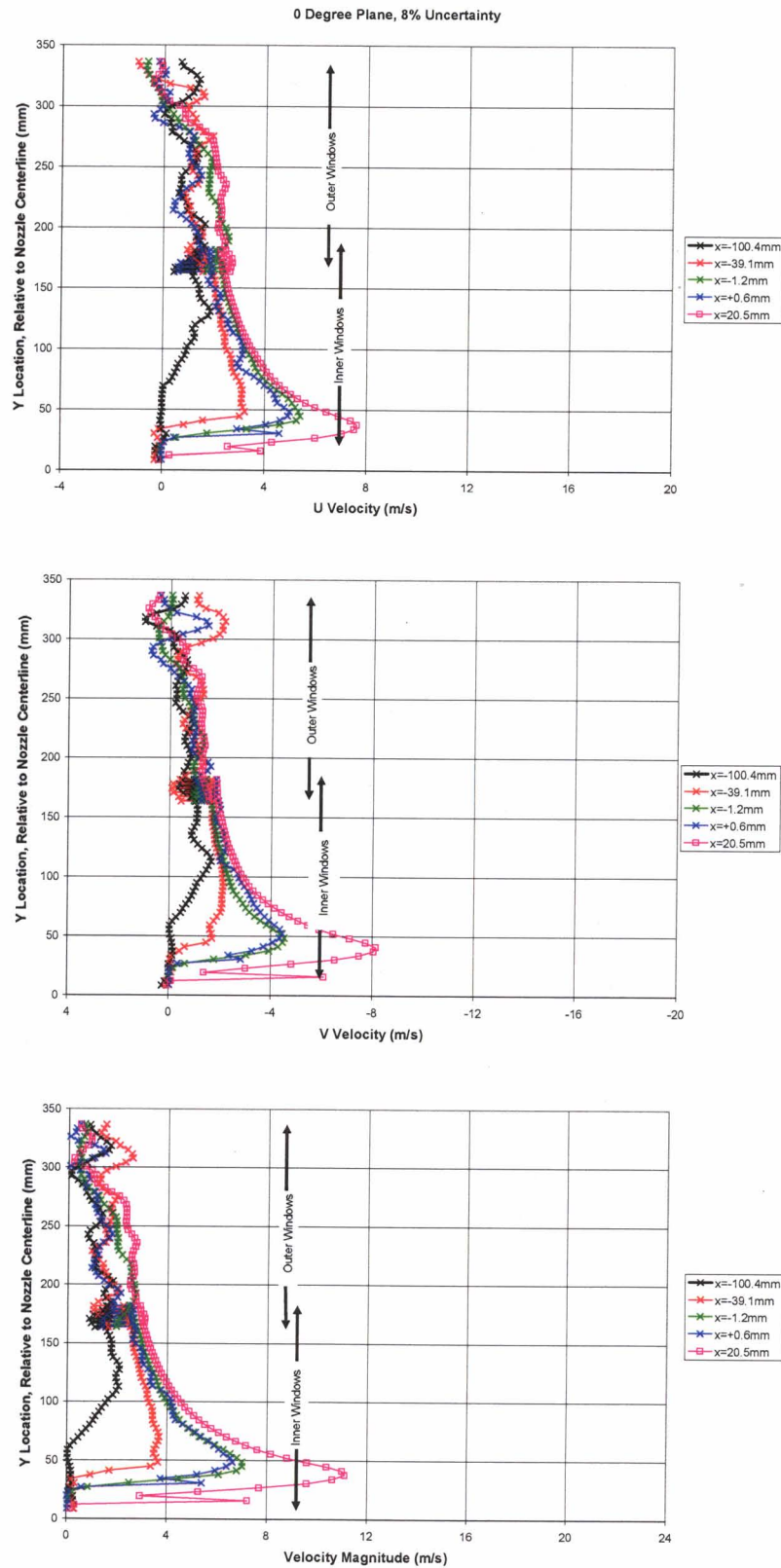
Figure 39. PIV Measured Velocities at Five Axial Stations in the 0° Plane for the
Stratford Nozzle.
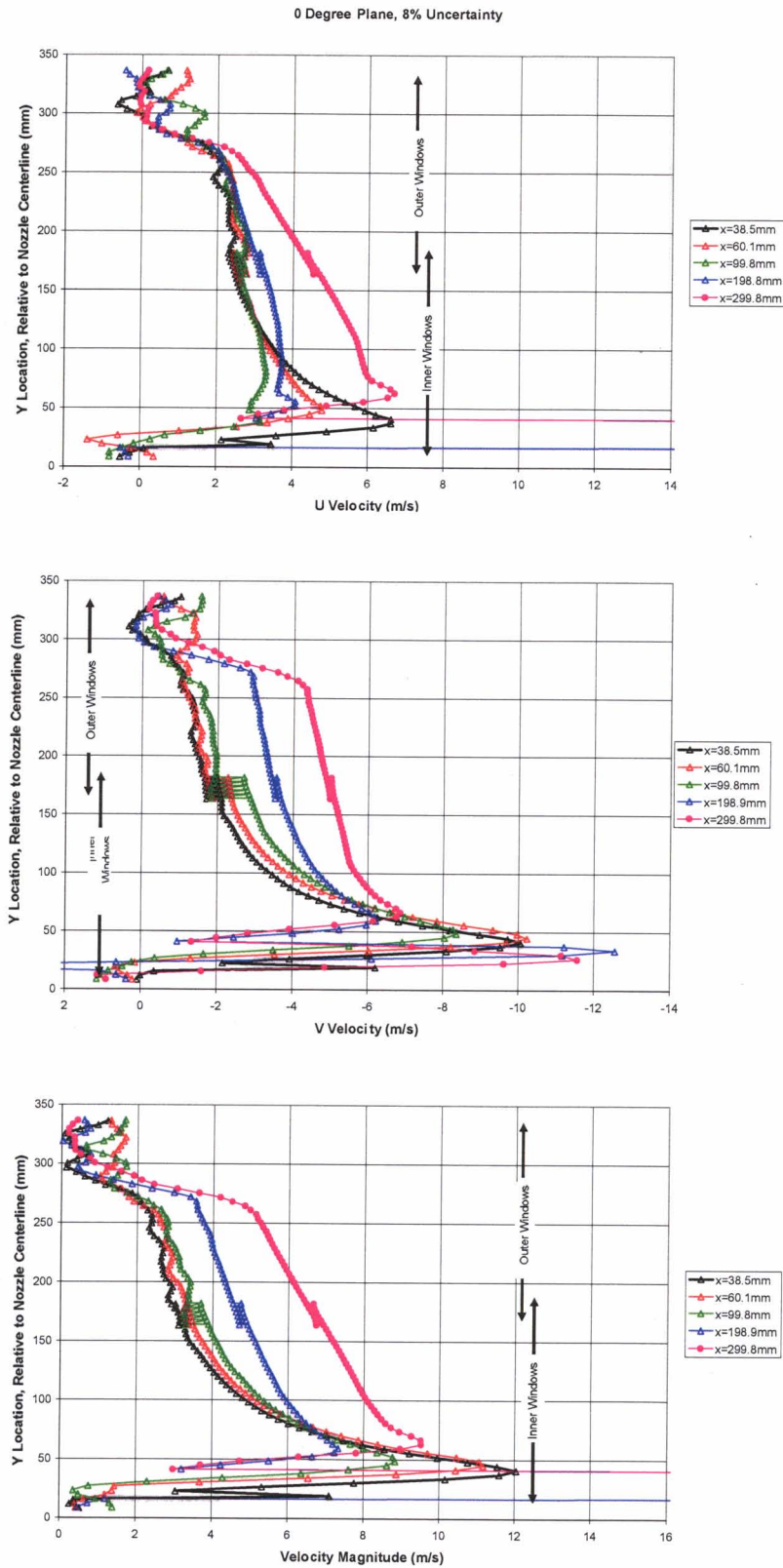
Figure 40. PIV Measured Velocities at Five Additional Axial Stations in the 0° Plane for the Stratford Nozzle.
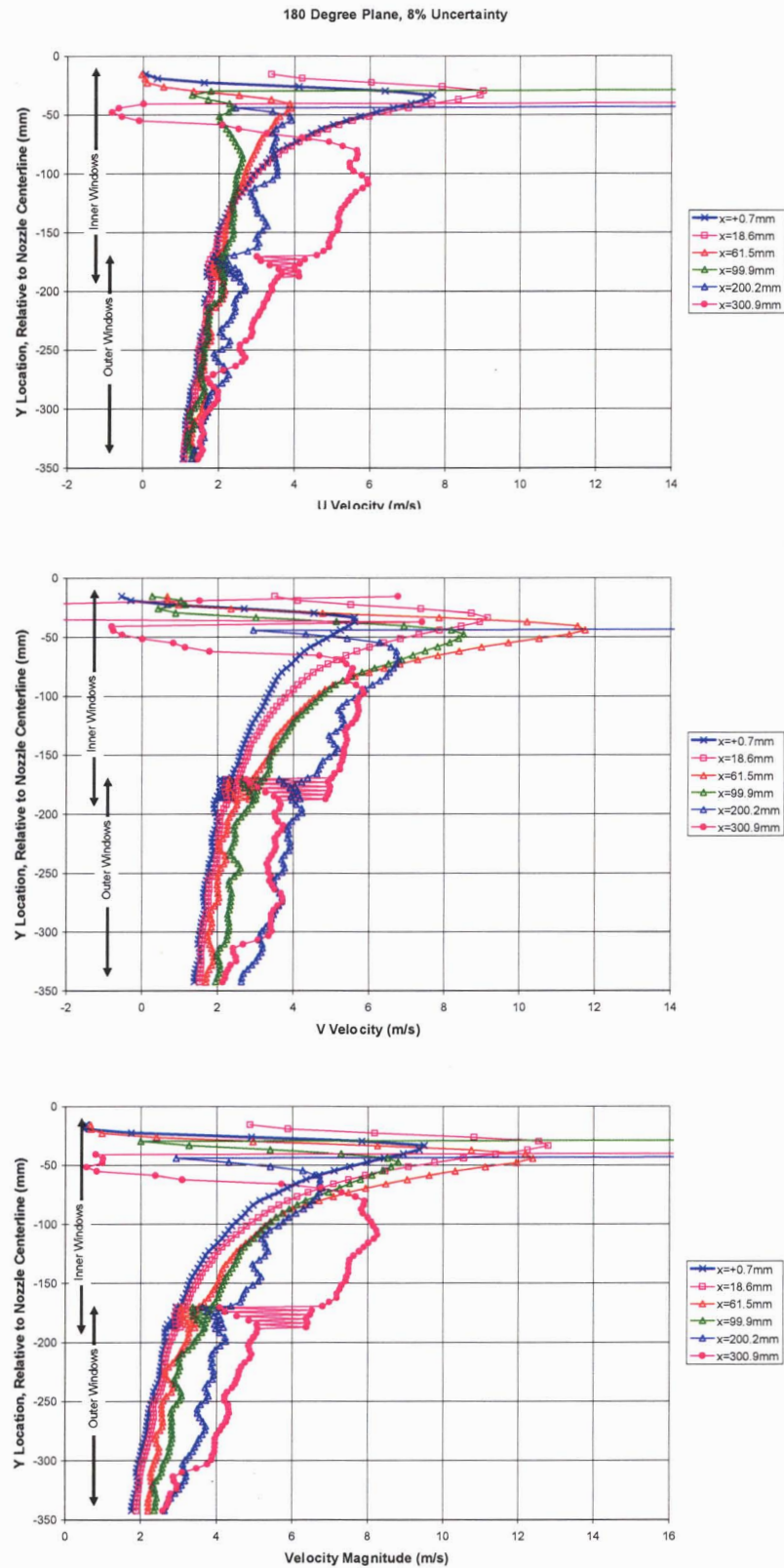
Figure 41. PIV Measured Velocities at Six Axial Stations in the 180° Plane for the Stratford Nozzle.
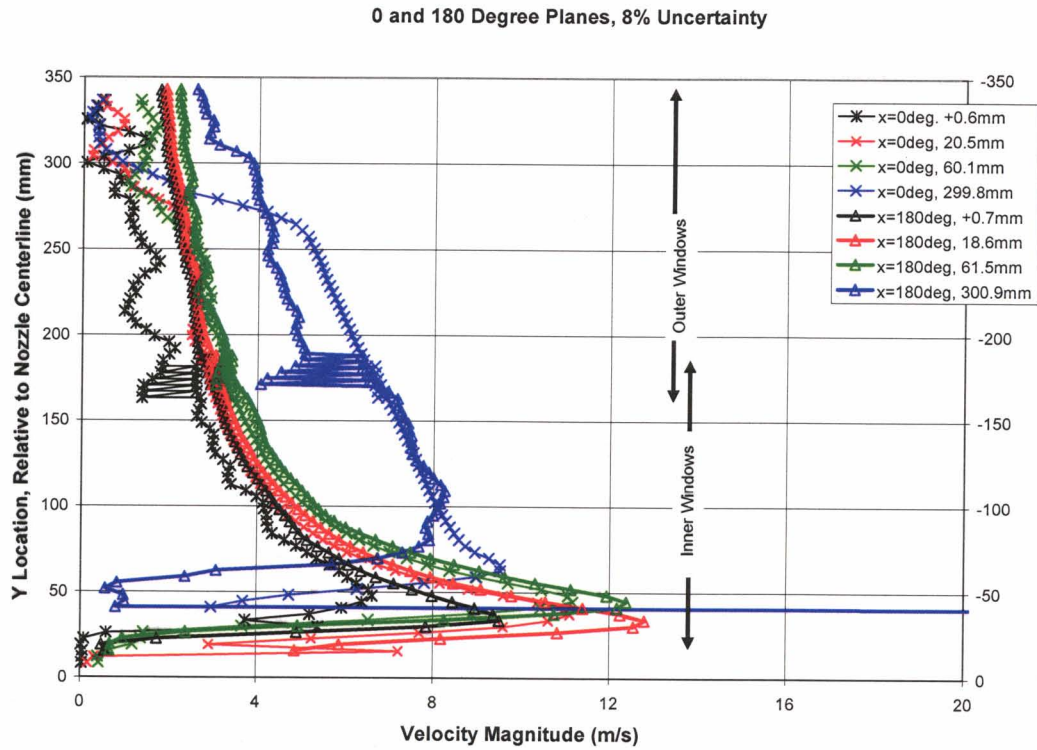
Figure 42. Comparing PIV Measured Velocities for the 0 and 180° Planes at Axial Stations for the Stratford Nozzle.

3.4.1.2.3. Windows I and J – The Plume Capture Pipe Sink

For the Stratford nozzle, two additional windows of PIV data were acquired just above the plume capture pipe. Windows I and J are shown in Figure 43 through Figure 45. The merged data for the I window was created from datasets with significantly different delta-Ts. This explains in the unusual velocity contours above and in front of the pipe inlet. The PIV data resolved maximum velocities of 25m/s above the pipe and 61m/s below the upper lip of the pipe.

These velocities are evidence of sub ambient pressure, or a 'sink', which existed inside the plume capture pipe. This sink was created by the ejector effect of the plume attaching to the inner wall of the plume capture pipe. A viscous, high speed flow, in close proximity to a wall, creates a low pressure region. This sub ambient pressure acted as a pump that sucked ambient air in. The velocity contours and vectors in Figure 45 show flow heading inward from all locations – a classic example of a sink. This sink existed for the full circumference of the plume capture pipe.

The Excel files of the PIV data for I and J windows are included in the electronic media associated with this report. The structure of the Excel files is similar to those for the rest of the PIV windows. These Excel files are described in Section 3.4.6.
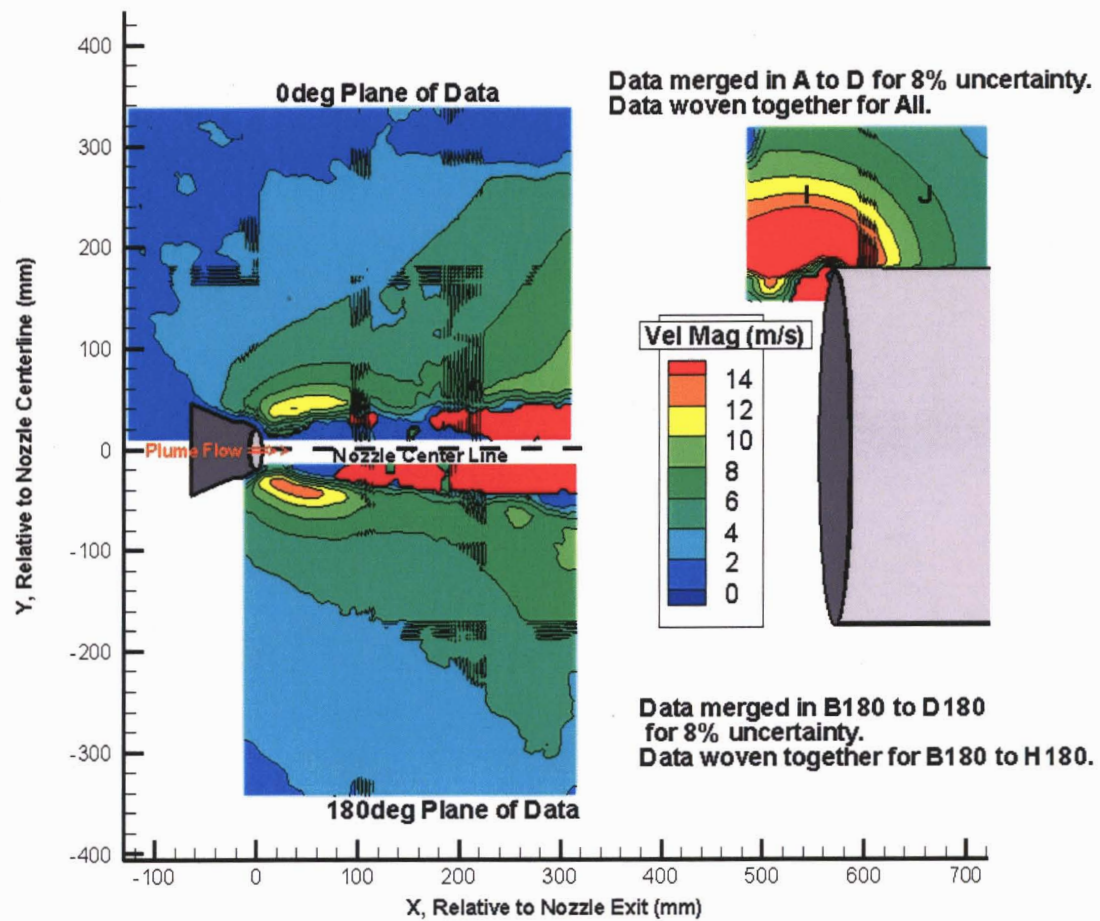
Figure 43. PIV Data Near the Plume Capture Pipe.
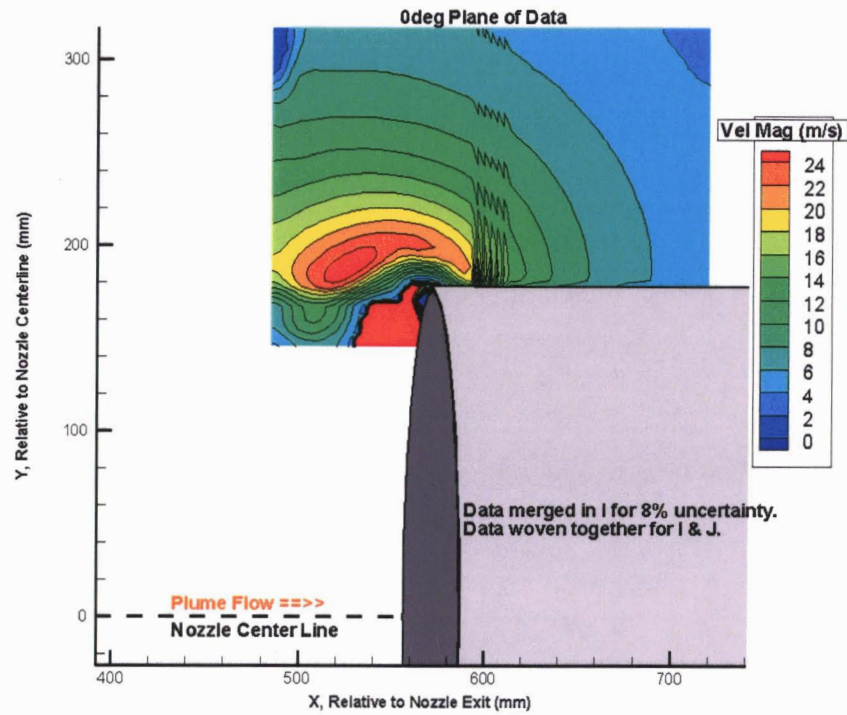
Figure 44. Close up View of PIV Data Near the Plume Capture Pipe.
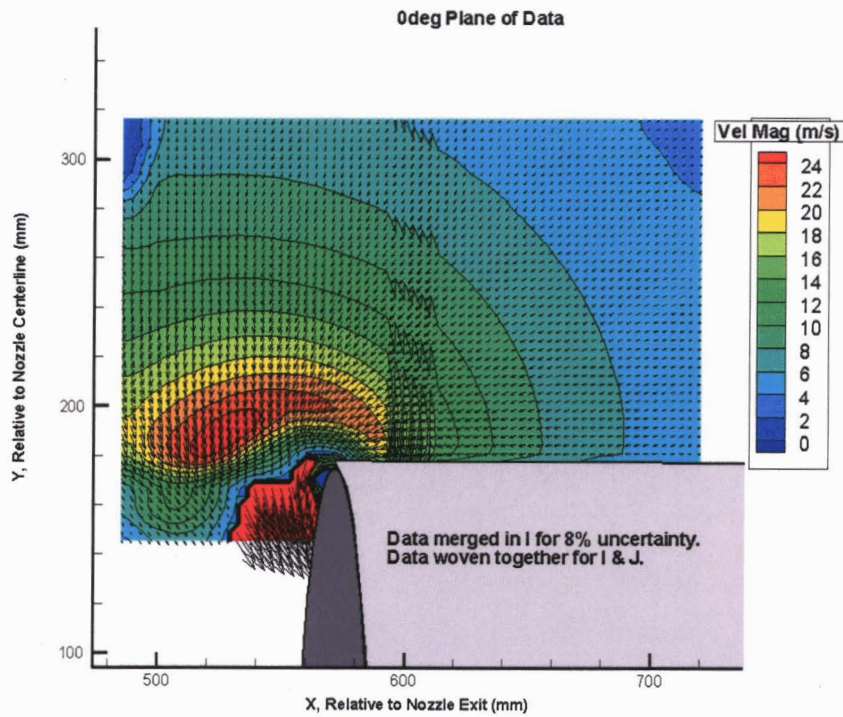
Figure 45. Velocity Vectors from the PIV Data Near the Plume Capture Pipe.

3.4.2. Bell Nozzle

3.4.2.1. Data Taken

Chronological Order with Notes from the Run Logs

All the PIV data could not be taken in one run. Typically, two to four windows of PIV data could be obtained in each run. The limiting factors were the position of the PIV laser sheet generator, the traversing limits of the mechanism that held the PIV camera and the NTF's supply of hot air. The Bell nozzle PIV data were taken in the following order.

Run 50, Windows A and E
Run 51, Windows B and F
Run 52, Windows C and G
Run 53, Windows D, H and K
Run 55, Windows B180, F180, G180, C180, D180 and H180.

Bell Nozzle inlet conditions during PIV data acquisition are shown in Figure 14 and Figure 15. Run 55 was the last possible run of the test series. The intent was to get all data possible even if the nozzle set point could not be maintained (see Figure 15). The nozzle set point was maintained for windows B180, F180 and G180. It began to drift down from ~19.65atm to ~19.4atm during acquisition of window C180. The set point continued to drift down during acquisition of windows D180 (~19.2atm) and H180 (~18.9atm).

Delta-T Matrix and File Naming Convention.

The term 'window' refers to a region in space in which data was collected. This region was function of the camera's field of view. The term 'dataset' refers to a set of PIV data recorded at a specific delta-T in a window. Multiple PIV datasets were obtained at each window. Table 5 documents the different delta-T intervals used to acquire the PIV datasets. Each of these PIV datasets is in the electronic media associated with this report.

Table 5. Matrix of Delta-Ts at Each Window and Names of the Data Files.

WINDOW	2 ms	5 ms	20 ms	50 ms	100 ms	200 ms	300 ms	500 ms
	Laser Pluse Dt							
A				Bell A050.dat		Bell A200.dat	Bell A300.dat	
B		Bell B005.dat		Bell B050.dat		Bell B200.dat		
C		Bell C005.dat		Bell C050.dat		Bell C200.dat		
D		Bell D005.dat		Bell D050.dat		Bell D200.dat		
E				Bell E050.dat		Bell E200.dat		Bell E500.dat
F				Bell F050.dat		Bell F200.dat	Bell F300.dat	Bell F500.dat
G				Bell G050.dat		Bell G200.dat	Bell G300.dat	Bell G500.dat
H			Bell H020.dat	Bell H050.dat		Bell H200.dat	Bell H300.dat	Bell H500.dat
K							Bell K300.dat	Bell K500.dat
B180		Bell B180005.dat		Bell B180050.dat		Bell B180200.dat		
C180		Bell C180005.dat		Bell C180050.dat		Bell C180200.dat		
D180				Bell D180050.dat		Bell D180200.dat		
F180						Bell F180200.dat	Bell F180300.dat	Bell F180500.dat
G180						Bell G180200.dat	Bell G180300.dat	Bell G180500.dat
H180						Bell H180200.dat		Bell H180500.dat

Relative and Absolute Positions of PIV Windows

A schematic of the windows in which PIV datasets were recorded is shown in Figure 46. Nine windows were obtained above the nozzle in the 0° plane. Six windows of PIV data were obtained below the nozzle in the 180° plane.

The position of the nozzle in the camera's FOV in the A, B and B180 windows was used to determine the coordinate transformations required to locate windows A and B180 in the global coordinate system of the Bell nozzle. (Note that the Stratford and Bell nozzle global coordinate systems are different). The data from the rest of the windows were then translated relative to the A and B180 windows based on the commands sent to the traversing mechanism. The translations for each window are provided in Table 6.

Table 6. Window Coordinate Transformations for Bell Nozzle PIV Data.

General Notes
Global Origin is at nozzle exit on nozzle centerline
All dimensions are in millimeters
The nozzle outer lip radii is 81.28

Notes for the 0degree Plane
Windows A through H and K are 133.072 mm wide by 179.8 mm tall

The origin of A was 119.922 to left of nozzle exit plane
B & F were 110 mm to right of A & E. C & G were 110 mm to right of B & F. D, H & K were 90 mm to right of C & G.

The bottom of A through D was 22.87mm below the nozzle lip.
E through H were 155 mm above A through D. K was 250 mm above D

Window Name	K	
	X	Y
Translations	-119.922 +110 +110 +90	-22.87 +81.28 +250
Total Translation	190.078	308.410
Global Coordinates	190.078 to 323.16	308.41 to 488.21

Window Name	E		F		G		H	
	X	Y	X	Y	X	Y	X	Y
Translations	-119.922	-22.87 +81.28 +155	-119.922 +110	-22.87 +81.28 +155	-119.922 +110 +110	-22.87 +81.28 +155	-119.922 +110 +110 +90	-22.87 +81.28 +155
Total Translation	-119.922	213.410	-9.922	213.410	100.078	213.410	190.078	213.410
Global Coordinates	-119.922 to 13.15	213.41 to 393.21	-9.922 to 123.15	213.41 to 393.21	100.078 to 233.15	213.41 to 393.21	190.078 to 323.16	213.41 to 393.21

Window Name	A		B		C		D	
	X	Y	X	Y	X	Y	X	Y
Translations	-119.922	-22.87 +81.28	-119.922 +110	-22.87 +81.28	-119.922 +110 +110	-22.87 +81.28	-119.922 +110 +110 +90	-22.87 +81.28
Total Translation	-119.922	58.410	-9.922	58.410	100.078	58.410	190.078	58.410
Global Coordinates	-119.922 to 13.15	58.41 to 238.21	-9.922 to 123.15	58.41 to 238.21	100.078 to 233.15	58.41 to 238.21	190.078 to 323.16	58.41 to 238.21
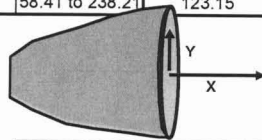
Window Name	B180		C180		D180	
	X	Y	X	Y	X	Y
Translations	-14.700	-160.3 -81.28	-14.7 +110	-160.3 -81.28	-14.7 +110 + 90	-160.3 -81.28
Total Translation	-14.700	-241.580	95.300	-241.580	185.300	-241.580
Global Coordinates	-14.700 to 117.7	-241.58 to - 62.98	95.3 to 227.7	-241.58 to - 62.98	185.3 to 317.7	-241.58 to - 62.98

Window Name	F180		G180		H180	
	X	Y	X	Y	X	Y
Translations	-14.700	-160.3 -81.28 - 155	-14.7 +110	-160.3 -81.28 - 155	-14.7 +110 + 90	-160.3 -81.28 - 155
Total Translation	-14.700	-396.580	95.300	-396.580	185.300	-396.580
Global Coordinates	-14.700 to 117.7	-217.98 to - 396.58	95.3 to 227.7	-217.98 to - 396.58	185.3 to 317.7	-217.98 to - 396.58

Notes for 180degree Plane
Windows B180 through H180 are 132.187 mm wide by 178.6 mm tall
The origin of B180 was 14.7 mm to left of nozzle exit plane
C180 & G180 were 110 mm to right of B180 & F180. D180, H180 were 90 mm to right of C180 & G180.

The bottom of B180 through D180's was 160.3 mm below the nozzle lower lip.
F180 through H180 were 155 mm below B180 through D180.

These translations were applied to the coordinate system of the datasets for each window. Each window's datasets consist of a matrix of 36 by 49 data points. The origin of the coordinate system of each window's data points is that window's lower left hand corner. The fifth and sixth columns in each dataset file (Table 5) are the X and Y positions (in mm) of each data point within that window's datasets. The translations given in Table 6 were applied to these X-Y coordinates to position each window's datasets in the Bell nozzle's global coordinate system.

The internal coordinate systems of the datasets in the 0° plane are identical. That is, the matrix of X-Y locations in the datasets relative to the windows' origin is the same. Likewise all datasets in the 180° plane have the same matrix of X-Y points. There are slight differences between the 0° and 180° planes. See notes in Table 6 for details.
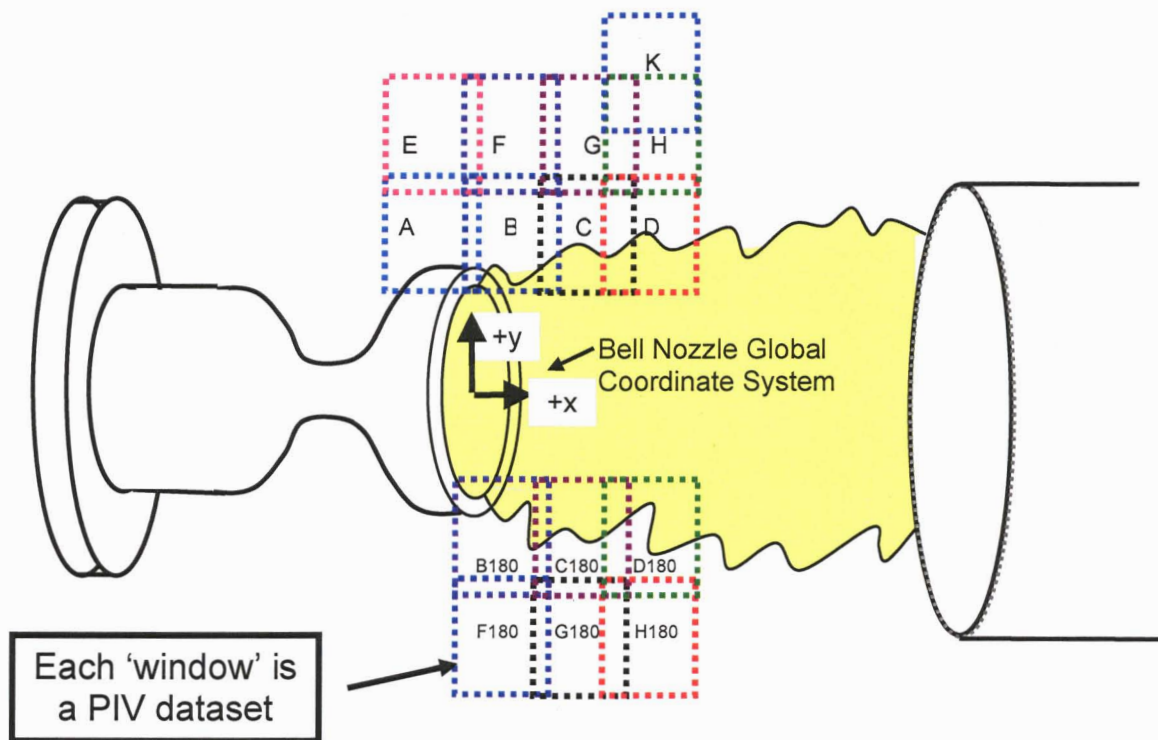
Figure 46. Schematic of PIV Windows for the Bell Nozzle.

3.4.2.2. Velocity Field Discussion

The velocity data is presented in two forms. First, the best dataset for each window, without modification of the datasets, is presented. Second, a single dataset created from the best data available from all datasets of all windows, is presented.

3.4.2.2.1. Best Data Without Manipulation

Table 5 lists the different delta-Ts used to acquire data for each PIV window. The smaller delta-Ts resolved higher velocities better than the larger delta-Ts. Figure 47 illustrates this. The 5 and 50 microsecond delta-Ts resolved the higher velocities close to the nozzle exit. However, these small delta-Ts have higher uncertainty in the lower velocity regions (Figure 48).

Of the data recorded, it was judged that the best representation of the flowfield (without modification of the datasets) is captured by the 200 microsecond delta-T datasets for windows A to D and B180 to H180 and 500 microsecond delta-T datasets for windows E to K. Figure 49 presents these datasets. Note in these TecPlot images that the overlapped regions of adjacent windows are plotted, but only the window that is 'on top' is visible.

The datasets in Figure 49 are the best compromise between capturing the high velocity regions, acceptable uncertainty levels and smooth velocity gradients between adjacent windows. These datasets show the high velocity near the nozzle exit and the general acceleration of the entrained flow with axial position. The character of the flow is symmetric, but the 180° plane has lower peak velocities. The indicated low velocity near the centerline is the plume flow. The plume velocity was not measurable with the delta-Ts presented here. Also, the plume was not seeded as the objective of this test was to measure the entrained flow. The apparent low velocities at the outer edge of windows E to H and F180 toH180 are discussed in Section 3.4.3.
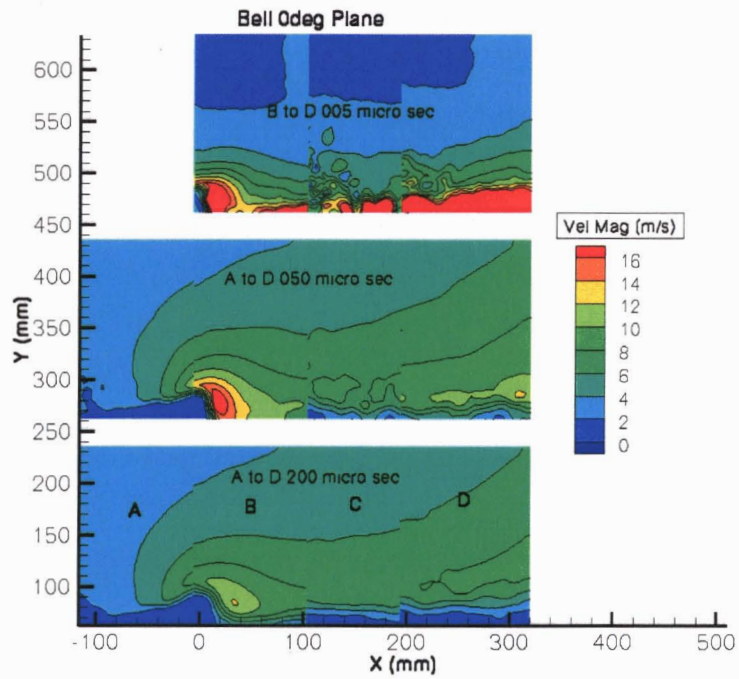
Figure 47. Velocities Resolved with Different Delta-Ts.
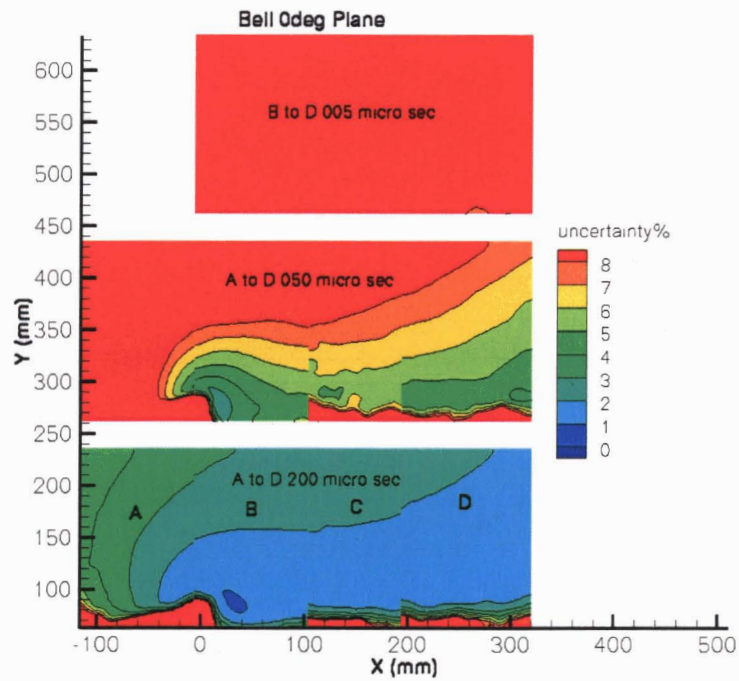
Figure 48. Uncertainty Resulting from Different Delta-Ts.
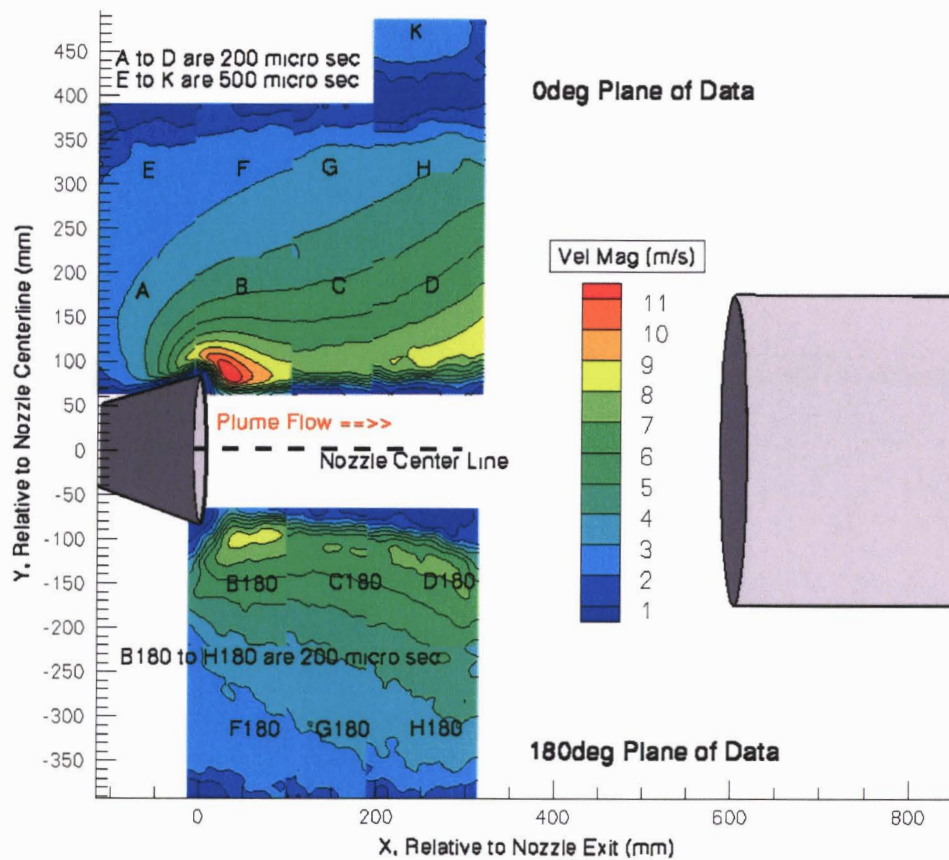
Figure 49. Best Representation of Bell Nozzle Entrainment Flowfield without
Modification of the PIV Datasets.

3.4.2.2.2. Merged Data Files

Velocity Contour Plots

A more accurate representation of the entrained flow was created by combining the data from the multiple delta-T datasets available for each window. The high velocity regions from the small delta-T datasets were 'merged' into the larger delta-T datasets that captured the general entrained flowfield better. Merging of multiple delta-T datasets was only required for the inner row of windows (A to D and B180 to D180) where there were large gradients in measured velocity.

Figure 47 and Figure 48 are used to explain the merging of multiple delta-T datasets. Note in the 5 and 50 microsecond datasets that higher velocities were resolved near the nozzle exit. The 50 microsecond delta-T dataset had relatively low uncertainty in this region. If one were willing to accept 8% uncertainty, much of the 50 microsecond delta-T dataset is acceptable near the plume shear layer and nozzle exit. These higher velocities were captured in the merged data shown in Figure 50.

The merging was done by assessing the data, point by point. The logic for merging was that the data from the smallest delta-T dataset was used if the uncertainty at that data point was 'acceptable' – in this example – an uncertainty of less than 8%. Because the calculation of PIV data uncertainty is somewhat subjective (as described in Section 2.4.3) an uncertainty was chosen that resulted in a fairly continuous velocity flowfield. For the Bell nozzle data, 8% uncertainty was deemed a good compromise between accuracy and resolution of the flowfield. Lower uncertainty levels (2 and 5% were assessed) resulted in noticeable flowfield discontinuities or flowfields that failed to capture the higher velocities near the plume shear layer and nozzle exit.

The merging of data within each window was done in an Excel spreadsheet. These Excel files are provided in the electronic media associated with this report. The structure of these files is discussed in Section 3.4.6. If an alternate uncertainty is desired, these files can be manipulated to produce merged data with the alternate uncertainty as the criterion.

After the data was merged within each window, the merged data were then joined or 'woven' together (by sorting on the radial and axial stations in the spreadsheet). Thus, creating a single data field that encompassed all of windows A to F (Figure 50) and a second that encompassed windows B180 to H180 (Figure 52). These woven data fields allow the overlapped regions to be seen when plotting contours in TecPlot. They also enable extracting line plots through the entire flowfield. (See Section 3.4.6 for discussion of the Excel files).

To clarify the terminology used here: 'merged' means that data from multiple delta-T datasets were evaluated point by point to determine the best value to use at each data point in a window. 'Woven' means that the data points from multiple windows were reordered into one contiguous data field for plotting.

Figure 50 and Figure 52 show that the resulting merged and woven PIV data resulted in fairly continuous flowfields. The saw tooth patterns indicate velocity discontinuities in the overlapped regions of adjacent windows. Figure 51 and Figure 53 are the corresponding uncertainties. For the uncertainties, the strong gradients between the inner and outer rows of windows are due to the different delta-Ts, not flow discontinuities.

Merged and woven for the 0° and 180° planes are shown together in Figure 54. Again, the general character of the 0° and 180° planes agree, but the peak magnitudes are lower in the 180° plane.

The contours in Figure 54 show there were two regions where the entrained flow was accelerated. These regions of acceleration indicate the location of the flow phenomena that induced the entrained flow. There was a distinct acceleration of the entrained flow near the nozzle exit, and a second more gradual acceleration, with axial station, of the entire entrained flowfield.

Figure 55 shows the velocity vectors near the nozzle exit. The vectors are not scaled by their magnitude. The effect of the reverse flow into the separated region of the Bell nozzle is evident in the vectors just downstream of the nozzle exit.
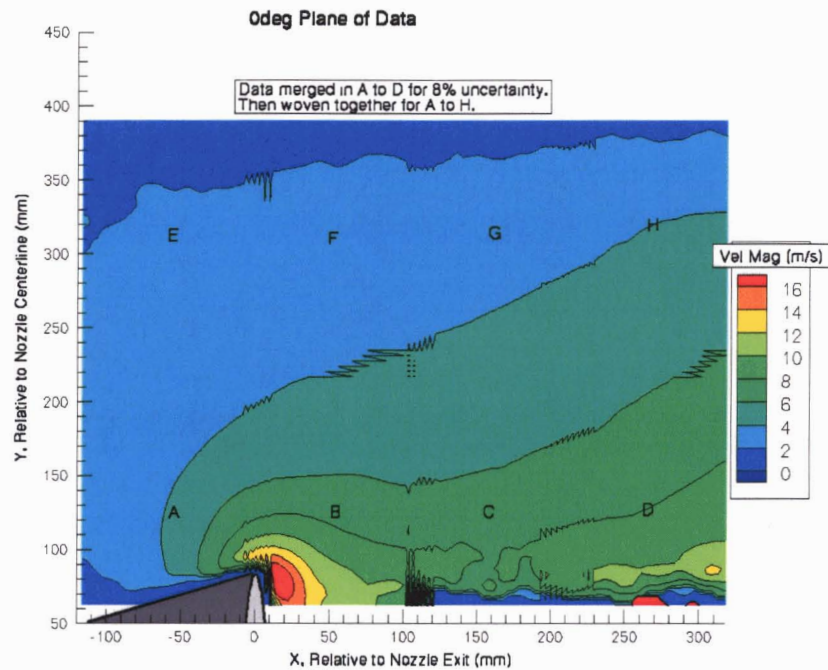
Figure 50. Merged and Woven PIV Velocity for 0° Plane for the Bell Nozzle.
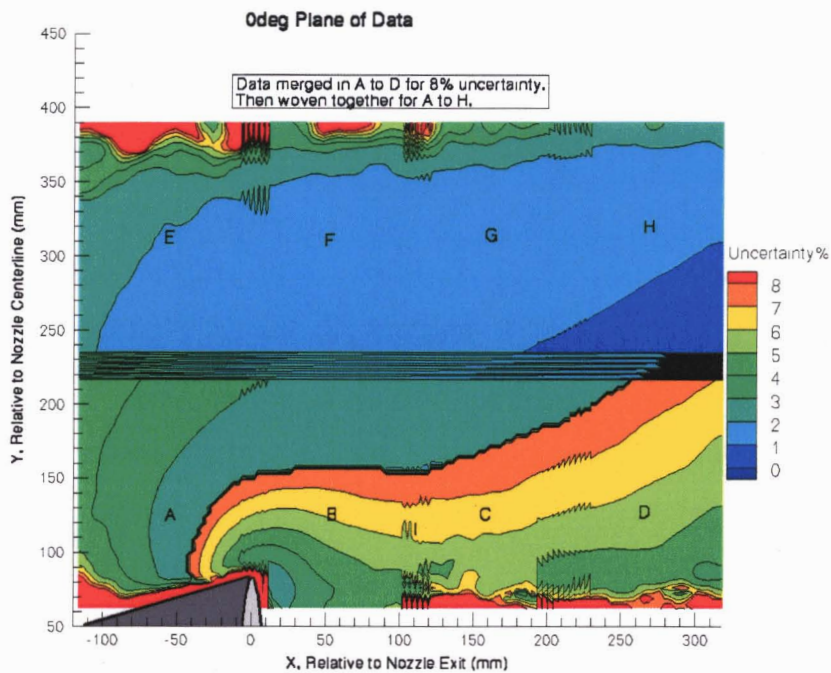
Figure 51. Uncertainty for the Merged and Woven PIV Data for 0° Plane for the Bell Nozzle.
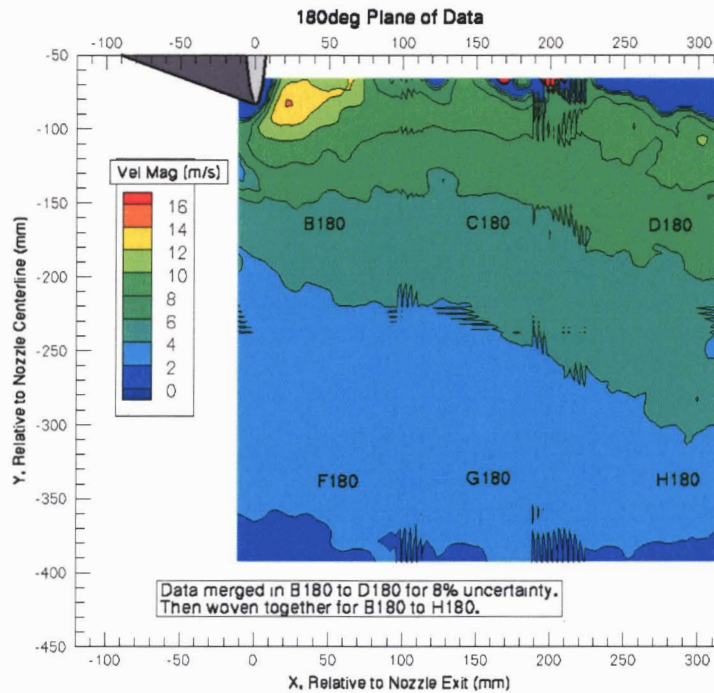
Figure 52. Merged and Woven PIV Velocity for 180° Plane for the Bell Nozzle.
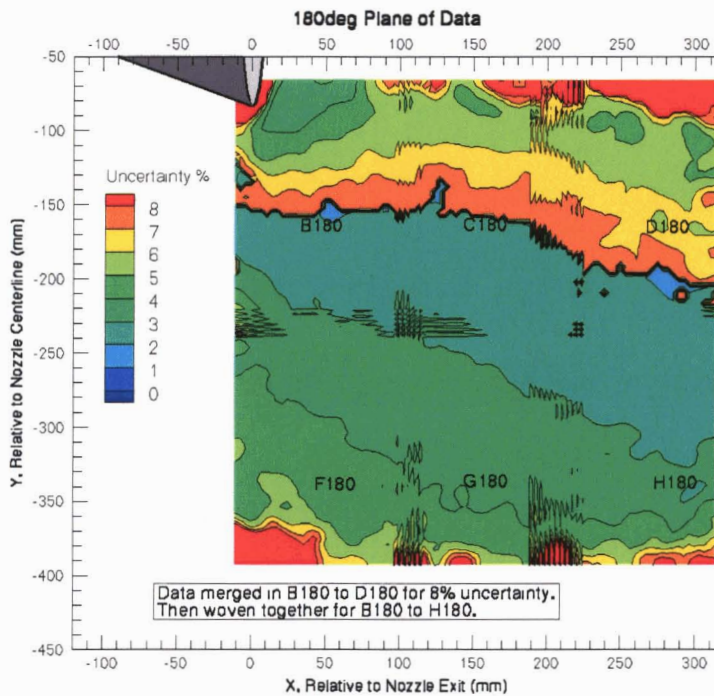
Figure 53. Uncertainty for the Merged and Woven PIV Data for 180° Plane for the Bell Nozzle.
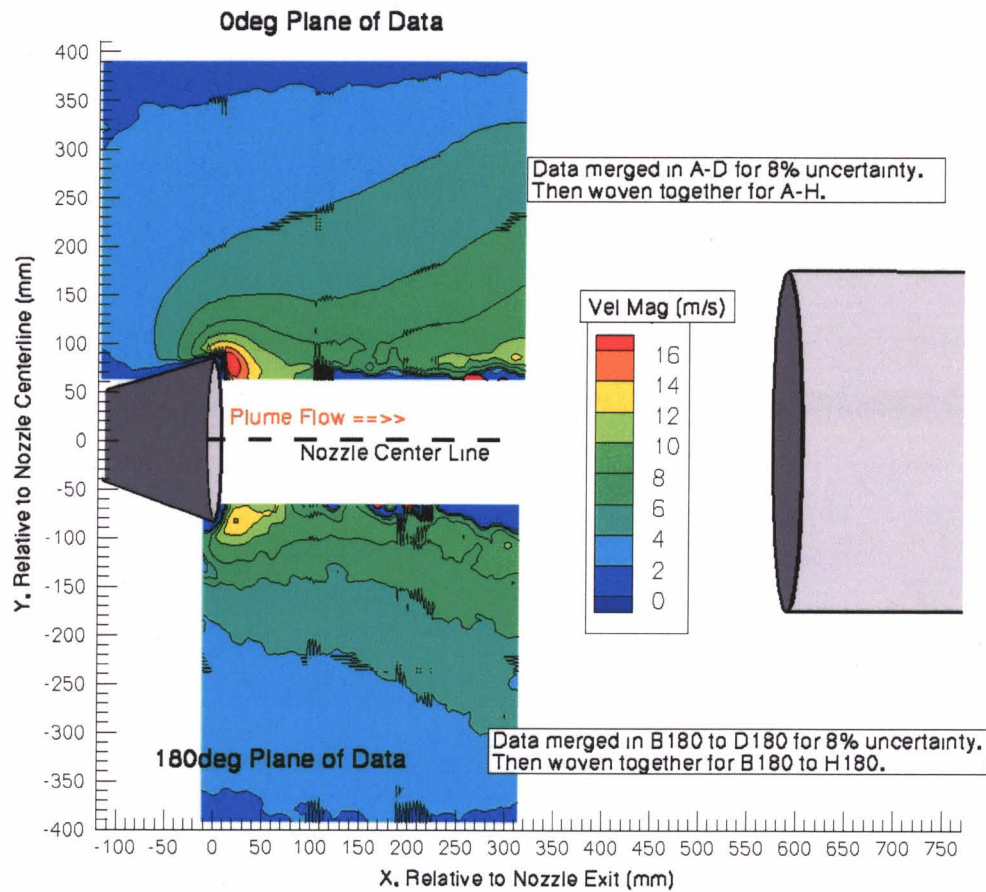
Figure 54. Merged and Woven PIV Velocity for Bell Nozzle.
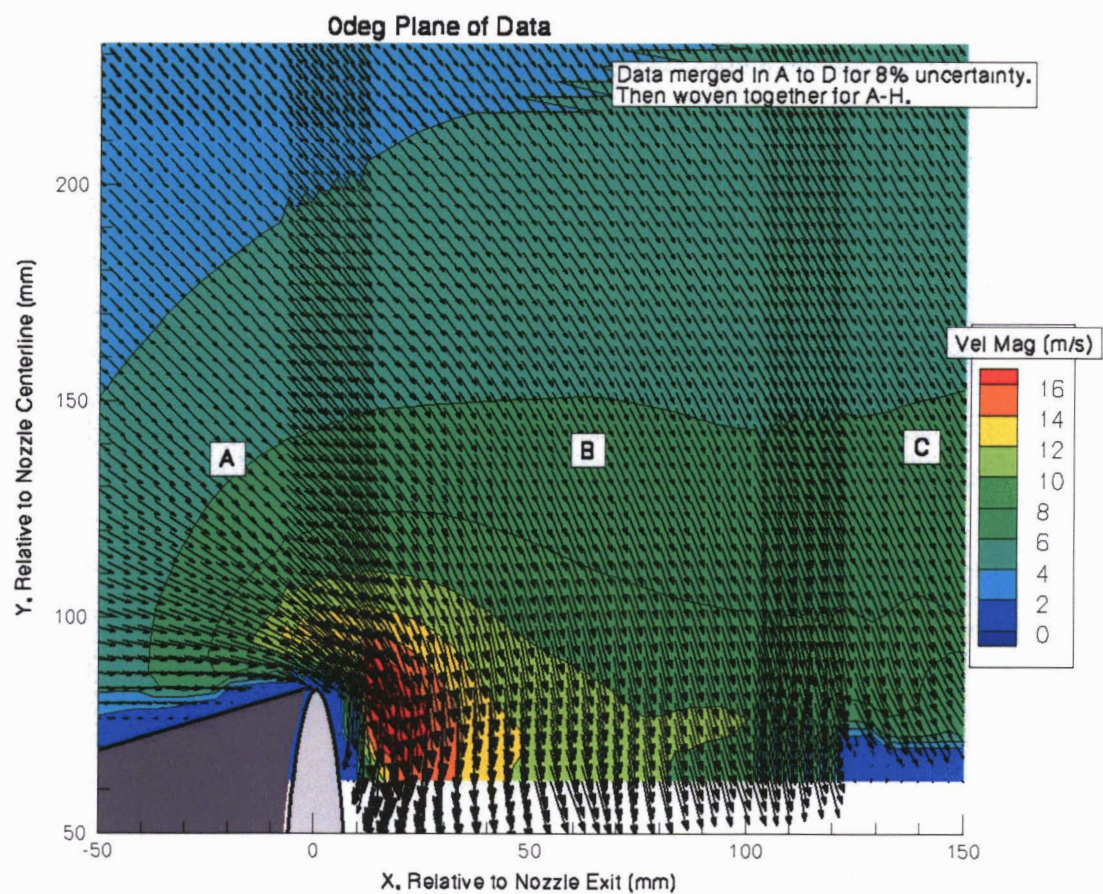
Figure 55. Velocity Vectors from the Merged and Woven PIV Data for Bell Nozzle.

Velocity Line Plots

Line plots of velocities at constant radial and axial stations are now discussed to illustrate some of the flowfield characteristics. The radial and axial stations for these line plots are shown in Figure 56. These plots were created in the Excel file that generated the woven data fields. The data plotted here can be extracted from that Excel file. The Excel file can be used to create additional line plots at alternate radial or axial stations as well.

Figure 57 shows the velocities at five constant radial stations from the merged and woven data field in the 0° plane. The saw tooth patterns in the lines are the overlapping regions of adjacent windows.

These velocity line plots show, as did the velocity contour plots, there were two regions where the entrained flow was accelerated. The first region was the strong acceleration close to the nozzle exit. For the Bell nozzle this acceleration was due to two phenomena, the nozzle flow separation and the viscous pumping of the plume shear layer. The second region of acceleration was the more general acceleration, with axial station, of the entire entrained flowfield. This second acceleration started at about X=125mm. The primary flow phenomena inducing the second, more general, acceleration was the sink created by the interaction of the plume and the plume capture pipe. The cause of the plume capture pipe sink is discussed in Section 3.4.1.2.3.

The acceleration near the nozzle exit is evident in all five profiles shown but most dramatically in the Y=94mm profile. The U-velocity component peaked just upstream, X~-10mm, of the nozzle exit (X=0mm) and the V-velocity component peaked just downstream of it, X~+10mm. The rapid decrease of the U-velocity component was a result of the reverse flow into the bell nozzle. The nozzle outer radius at its exit was 81.28mm. Although not shown in these line plots the effect of the nozzle exit was seen out to a radius of Y=~227mm in the 0° plane (and Y=~213mm in the 180° plane). The effect of the nozzle exit acceleration extended about 125mm downstream of the nozzle exit.

Downstream of X~125mm, the entrained flow's velocity increased due to (mainly) the plume capture pipe sink's effect. The slight erratic shape of the Y=94mm profile in the C window was caused by the difficulty in getting good PIV seeding for that window.

The same five radial stations are presented for the 180° plane in Figure 58. These profiles are not as smooth but exhibit the same general trends as the 0° plane. Figure 59 compares profiles for the 0 and 180° planes. Other than the velocity magnitudes close to the nozzle exit they agree well.

Figure 60 presents the 0° plane velocity at constant axial stations from the left hand side of windows A and E to just downstream of the nozzle exit. The peak velocities near the nozzle exit are illustrated. Note that the X=-40.8 and -1.2mm profiles intersect the nozzle hardware at their lower ends. Hence, the velocities go to zero for these

profiles. The X=-1.2 and 0.9mm profiles agree well and indicate there is not a significant difference within the overlapped region of windows A and B. They both show zero velocity at their lower ends because of the proximity of the nozzle hardware. Note that the 19mm profile contains negative U-velocity component. This resulted from the reverse flow induced by the separated nozzle flow.

Figure 61 plots 0° plane velocities at constant axial stations between X=40 and 300mm. The U-velocity components at X=40.4 and 62.0mm show the affect of the reverse flow near the nozzle exit. They both reached a maximum at Y~125mm then decreased to a local minimum at Y~75mm. Downstream of X=125mm, the bulk of the entrained flow began to accelerate. This acceleration was in part due to the shear layer but mainly a result of the plume capture pipe sink.

For the velocity measurements between X=0 and ~100mm the uncertainties (in Figure 51) indicate these velocities were valid. Sufficient seeding mixed into the plume shear layer in the nozzle separation induced recirculation. However, downstream of X=100mm, the velocities trending to zero should be disregarded. For example, the velocities at the lower end of the X=200.8 and 301.6mm profiles decreased rapidly. One would expect the flow to be accelerated in this area by the high velocity plume shear layer. But the PIV did not capture these velocities due to low seeding or the delta-Ts being too large.

Figure 62 plots entrained flowfield velocities at constant axial stations for the 180° plane. The lines are not as smooth as the 0° plane. However, the characteristics just discussed about the flow in the 0° plane were all present in the 180° plane. Figure 63 compares axial profiles from both planes to show the similarities.
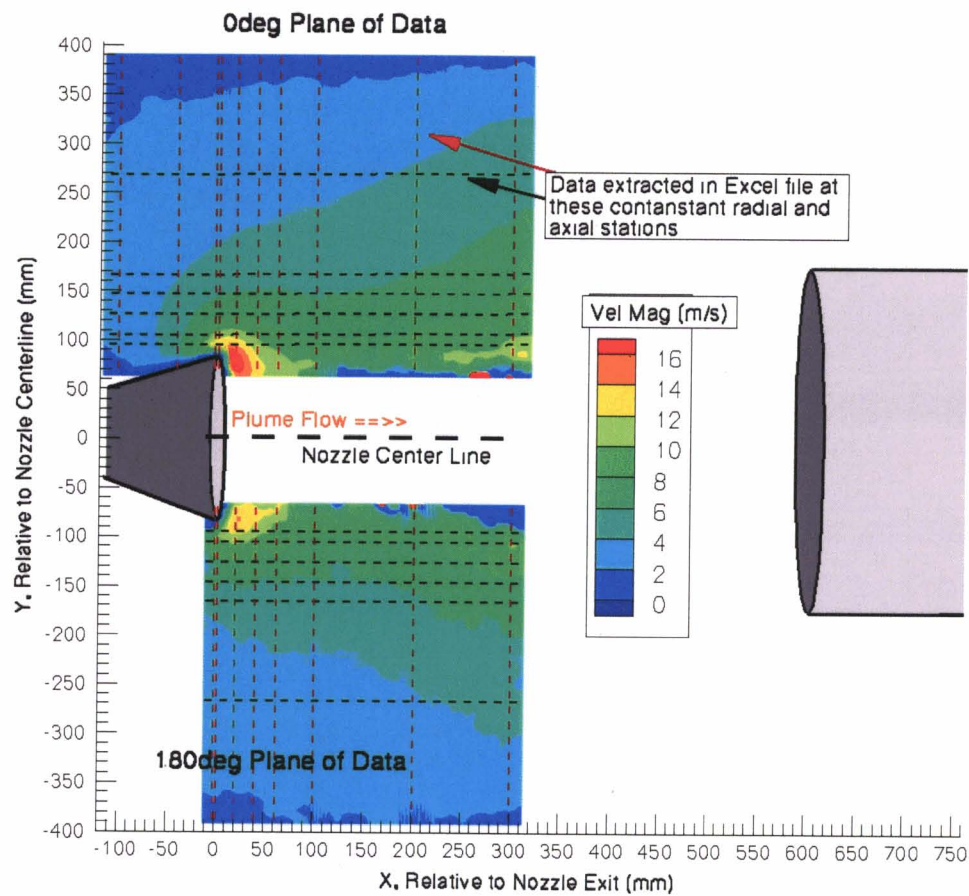
Figure 56. Axial and Radial Stations of Subsequent Velocity Profiles for the Bell Nozzle.
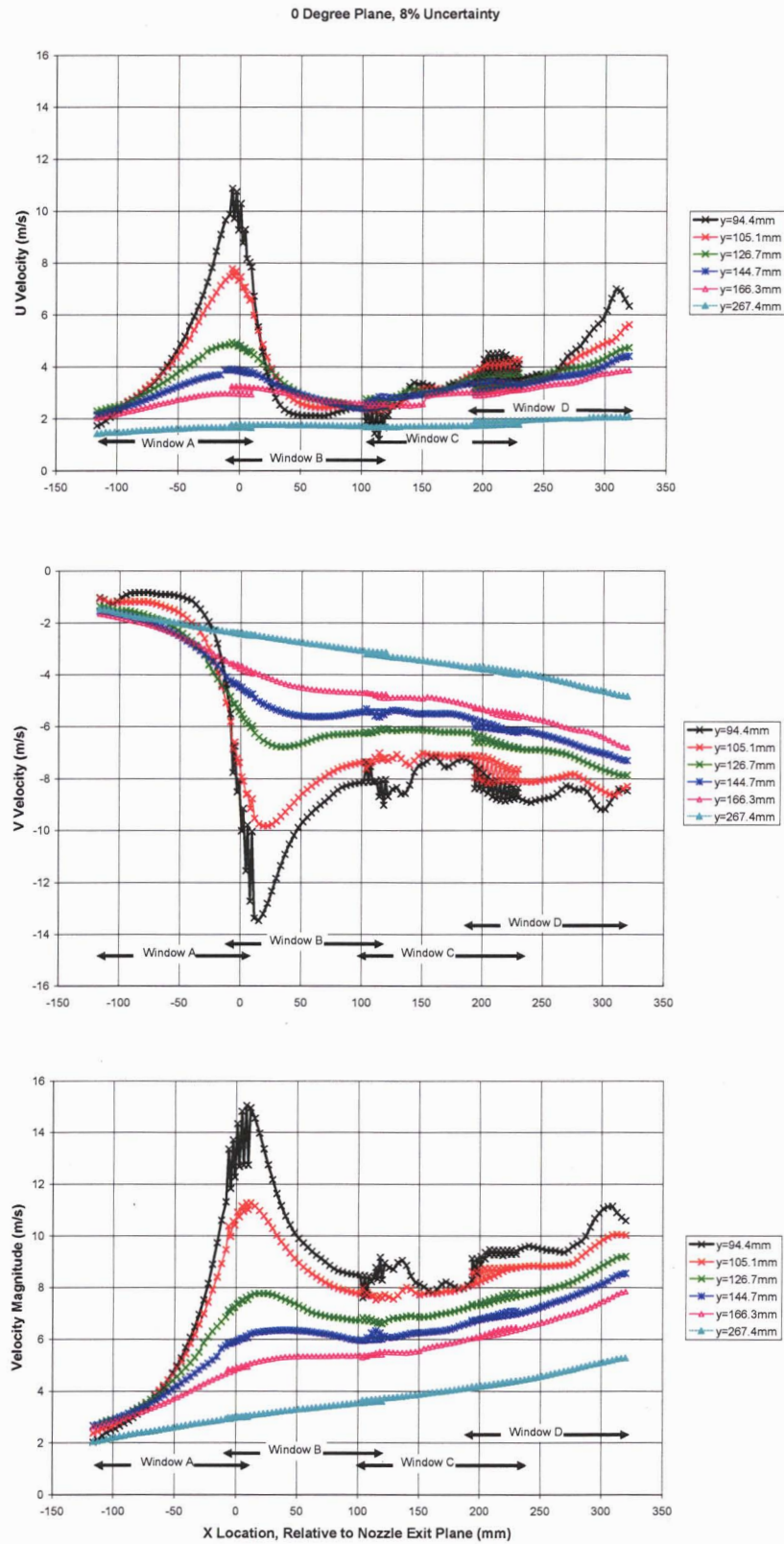
Figure 57. PIV Measured Velocities at Five Radial Stations in the 0° Plane for the Bell Nozzle.
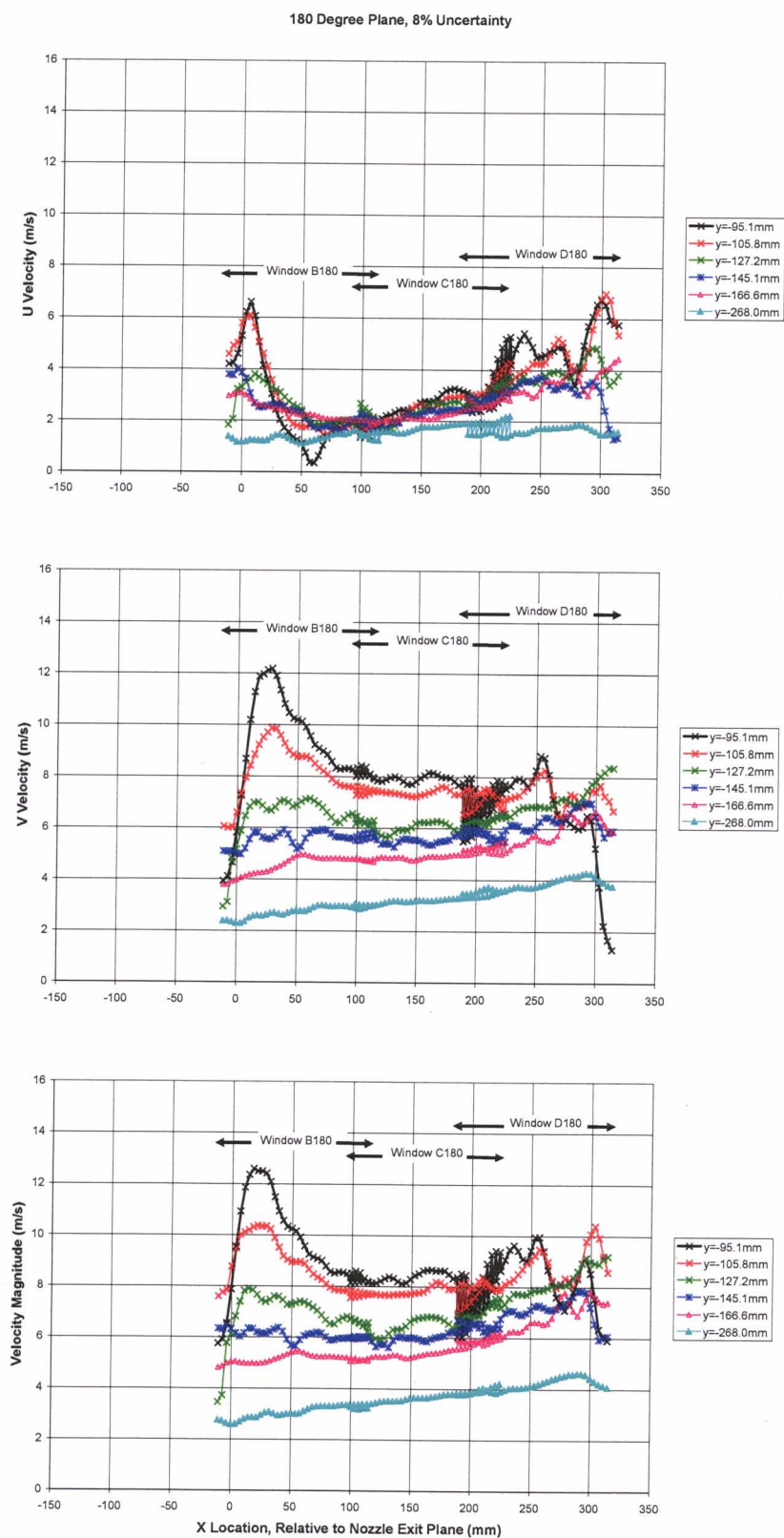
Figure 58. PIV Measured Velocities at Five Radial Stations in the 180° Plane for the Bell Nozzle.
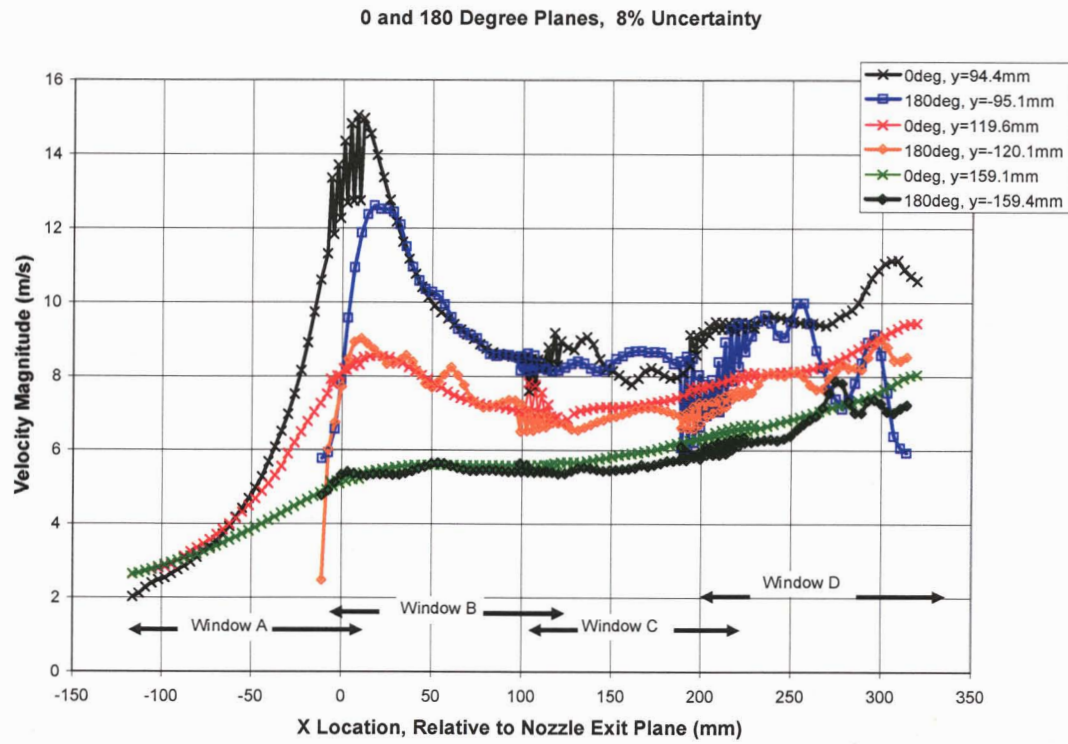
Figure 59. Comparing PIV Measured Velocities for the 0 and 180° Planes at Three Radial Stations for the Bell Nozzle.
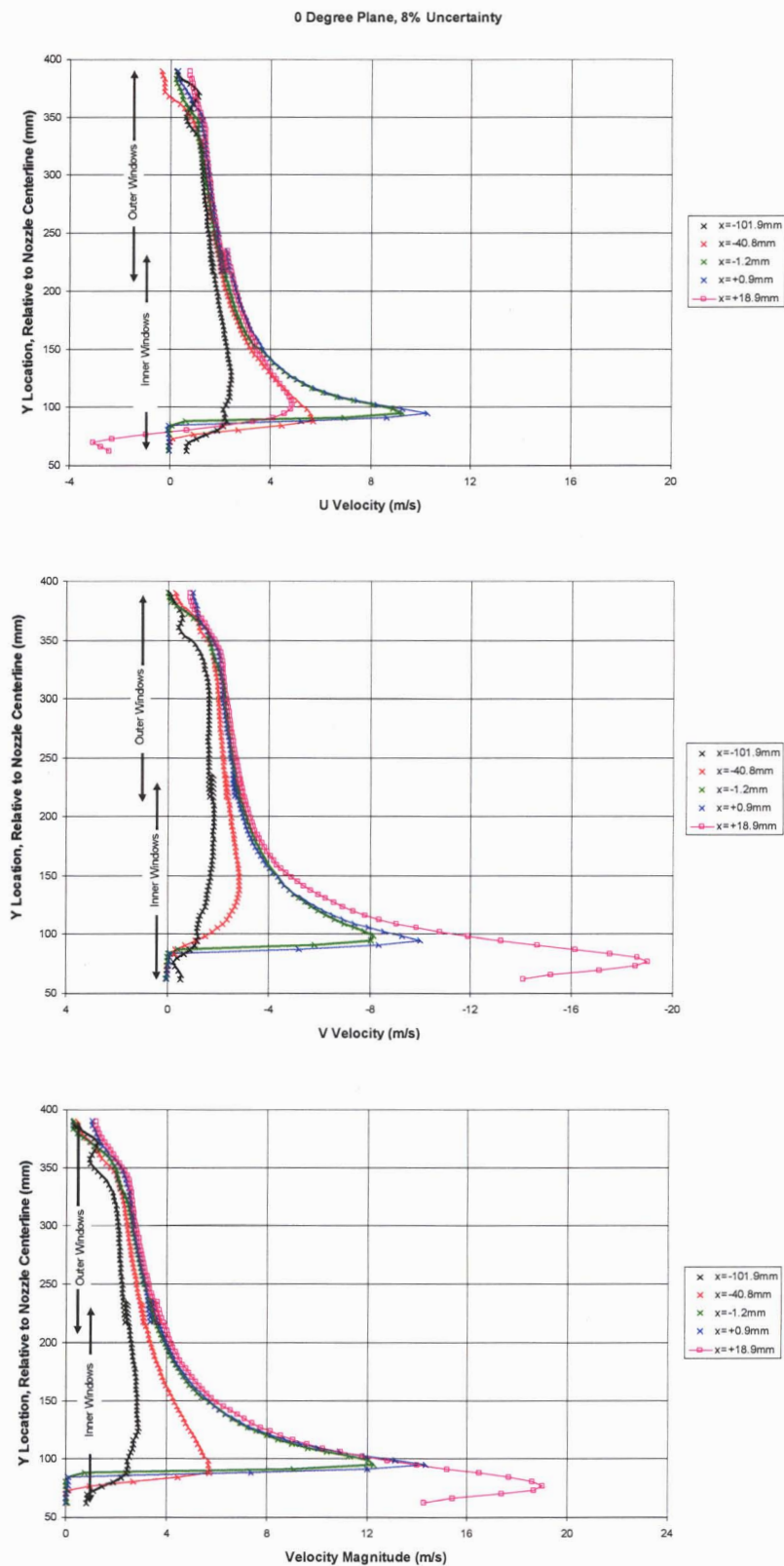
Figure 60. PIV Measured Velocities at Five Axial Stations in the 0° Plane for the Bell Nozzle.
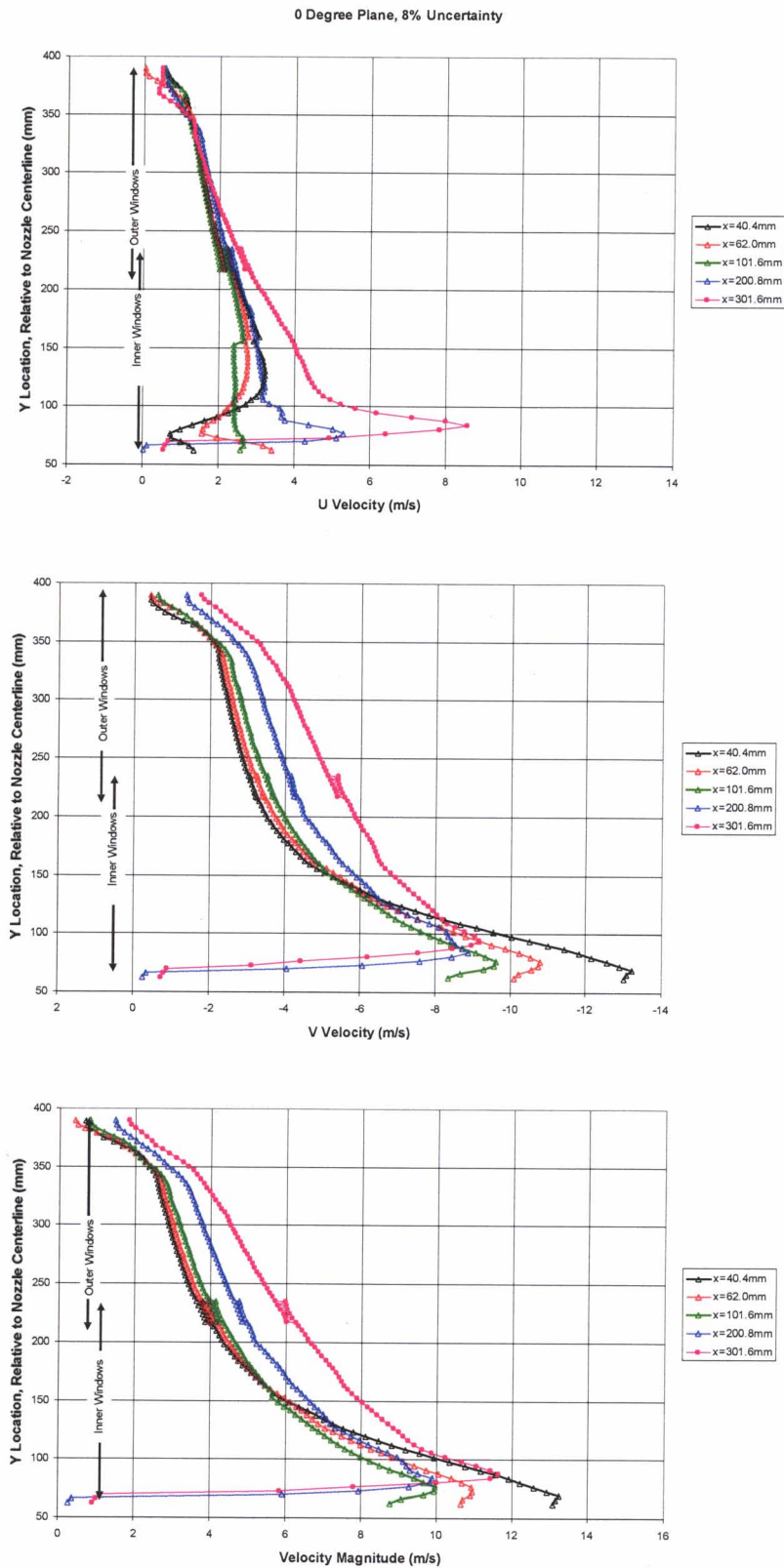
Figure 61. PIV Measured Velocities at Five Additional Axial Stations in the 0° Plane for the Bell Nozzle.
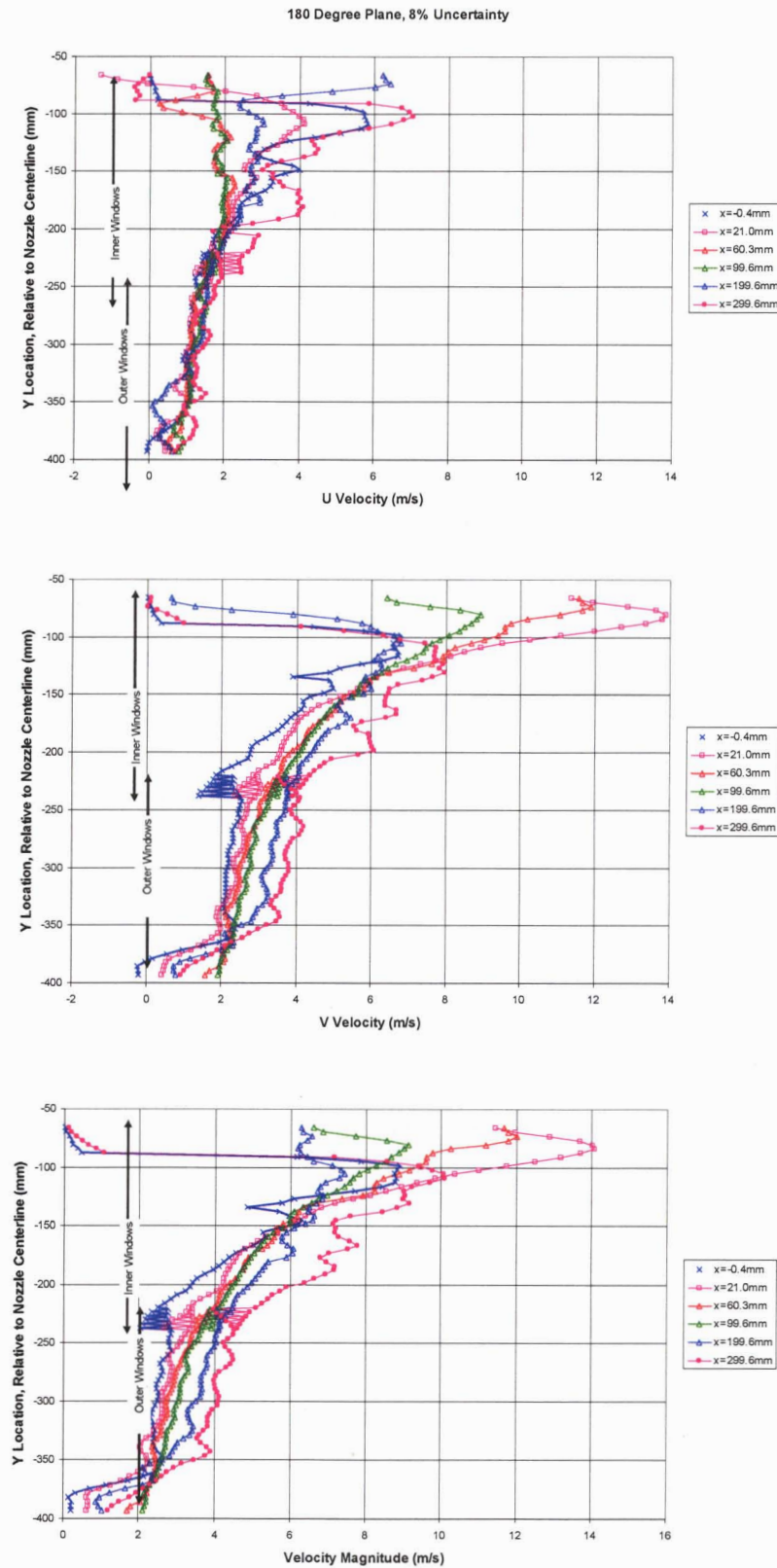
Figure 62. PIV Measured Velocities at Six Axial Stations in the 180° Plane for the Bell Nozzle.
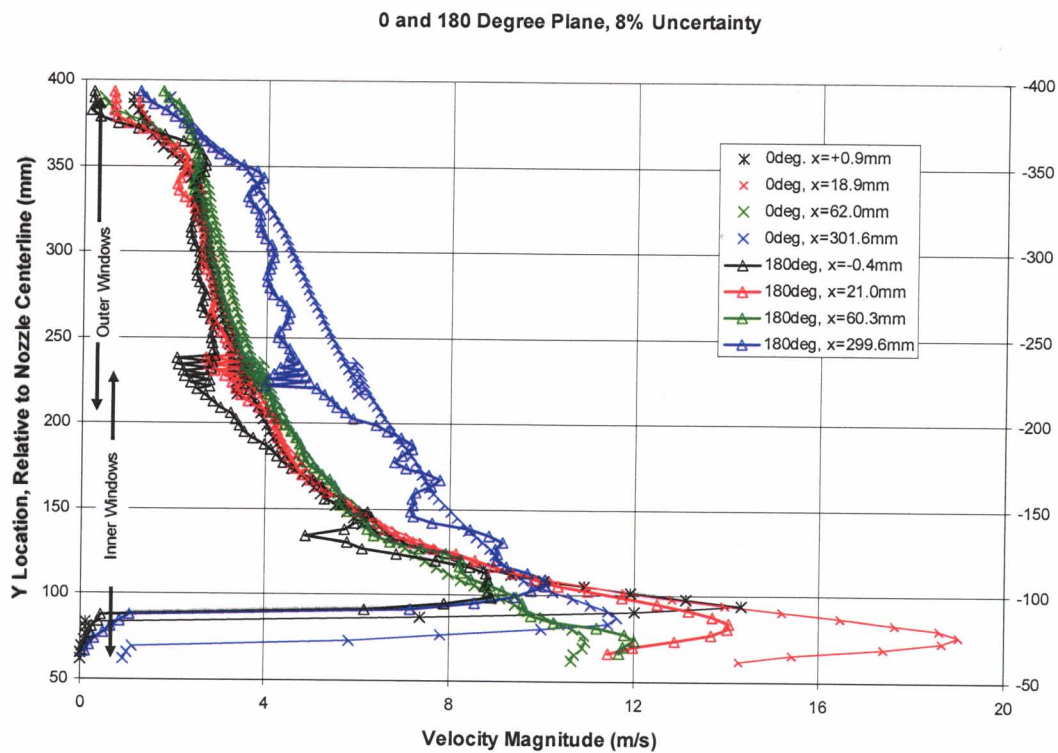
Figure 63. Comparing PIV Measured Velocities for the 0 and 180° Planes at Axial Stations for the Bell Nozzle.

3.4.3. Unsteady Layer

During testing, a region of unsteady flow was observed at the top of windows E to H in the Bell nozzle PIV data. In the average velocity plots, the unsteady layer appears as a low velocity region because the randomness of the velocity components drives the average toward zero. This low velocity region is seen at the top of windows E to H and the middle of window K in Figure 49 (and the top of Figure 33 for the Stratford nozzle). Evidence of it is also visible in the Bell nozzle velocity profiles in Figure 60 through Figure 63. An inflection exists in the velocity profiles at Y=350 and -350mm. This inflection marks the inner edge of the unsteady layer.

This unsteadiness was evident in every delta-T dataset for these windows. Window K captured the entire width of this unsteady region. Six frames of instantaneous velocity vectors for window K are presented in Figure 64. The electronic media associated with this report contains an animation of velocity vectors for all 300 frames from one dataset for window K.

During testing the unsteady layer was observed to be regular in its location and characteristics. The regions both above and below the layer had very steady uniform velocity vectors inward toward the plume; see Figure 64. Another unsteady layer appeared to be at the bottom of the F180 – H180 windows as well, although it was not as clearly delineated. Note that the layer was at the same radius at every axial station. It was not pulled toward the centerline by the radial inflow as one might expect.

This unsteady layer is present in the Stratford PIV data as well. In the Stratford PIV data the unsteady layer was at a radius of approximately 260mm in the 0° plane and was only detected sporadically in the 180° plane.

No explanation was found for this unsteady layer. Vortex shedding was considered. However, there was no hardware immediately upstream of the measurement windows that would induce vortex shedding. There were some flanges well upstream of the nozzle. But fog based flow visualization around the flanges did not indicate there was any vortex shedding off the flanges

No indication of the unsteady layer was found in the hot film anemometer data for either the Stratford or Bell nozzles.
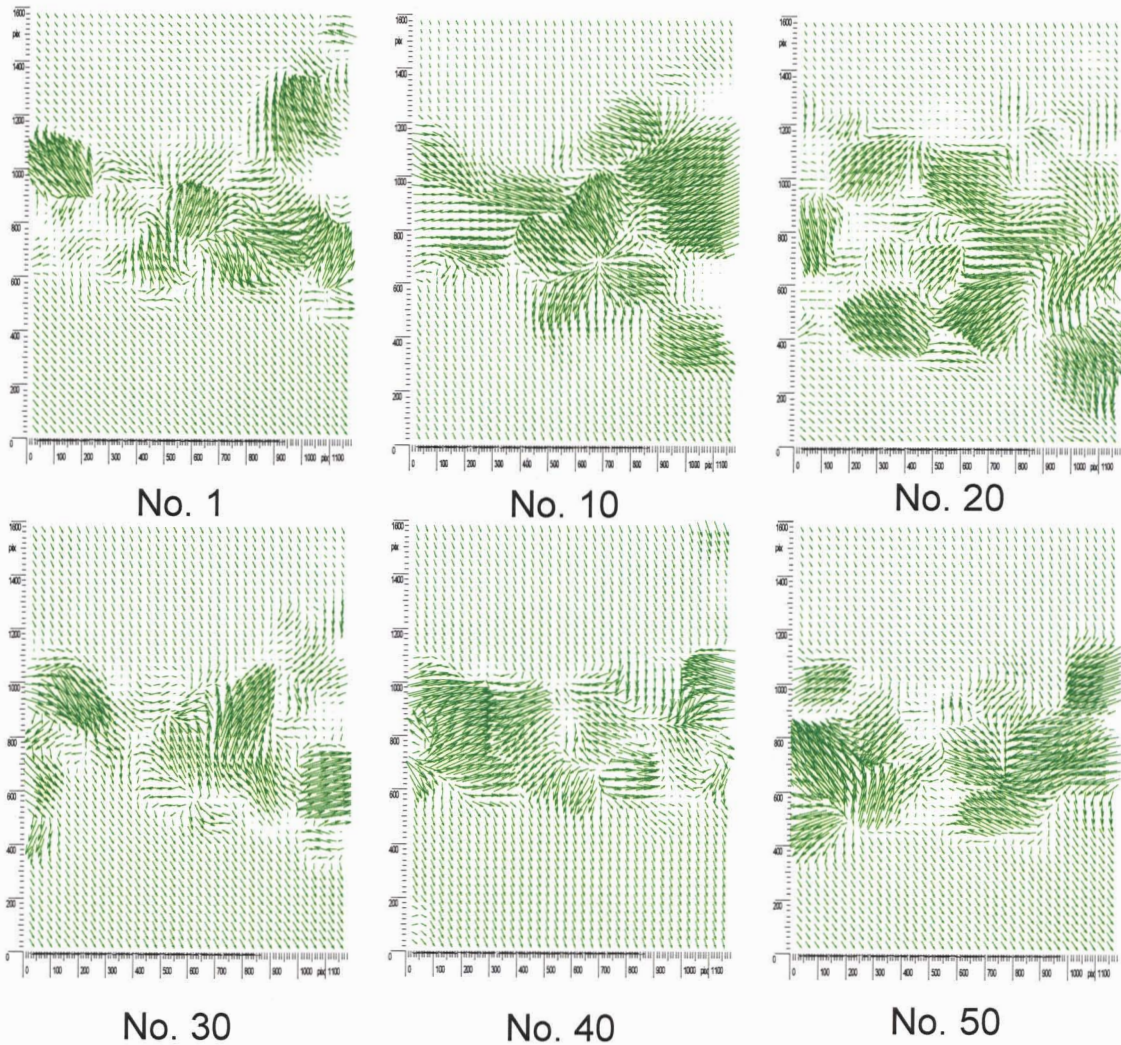
Figure 64. Velocity Vectors for Six of the 300 Instantaneous Frames of PIV Data from One Dataset of K Window.

3.4.4. PIV Measurement Repeatability

The test schedule did not allow repeating PIV measurements in any of the windows. However, the overlapped regions of neighboring windows are effectively five regions where PIV data was obtained multiple times. Therefore, the repeatability of the PIV measured velocities was assessed by comparing the velocities in these overlapped regions. The difference in time between acquisition of the datasets was as little as a minute (within the same NTF run), or as much as a full day (in another NTF run). The repeatability of the PIV measurements were affected by at least the following: the variation of seeding quality, the accuracy of the camera positioning and the consistency of the test conditions (nozzle inlet and ambient).

Repeatability was assessed by using the data from the regions where four windows overlapped. Five overlapped regions were analyzed for both nozzles. The overlapped regions were the coincident corners of the following sets of windows (see Figure 25 and Figure 46); A-B-E-F, B-C-F-G, C-D-G-H, B180-C180-F180-G180, and C180-D180-G180-H180.

For the Stratford nozzle, the repeatability was assessed by comparing the 100 microsecond delta-T datasets in the inner windows (A through D and B180 through D180) and 200 microsecond datasets in the outer windows (E through H and F180 through H180). For the Bell nozzle, repeatability was assessed for the 0° plane by comparing the 200 microsecond delta-T datasets in the inner windows and the 500 microsecond datasets for the outer windows. For the 180° plane 200 microsecond delta-T datasets were used for all windows. These delta-Ts were selected because they reflected the data selected by the merging technique discussed in Sections 3.4.1.2.2 and 3.4.1.2.2.

Because the data points from the four windows of an overlapped region were not at the same locations in the global coordinate systems, the velocity data for each window's dataset was linearly interpolated on to a common grid for that overlapped region. Therefore, each point in the common grid had four velocity values associated with it. A 95% confidence interval[5] was computed for this four sample set at each point. The confidence interval was then normalized by the average value at each point of the common grid. The minimum, maximum and average normalized confidence intervals for all the points in the common grids are presented in Table 7 through Table 10. The dimensional value of the average velocity components of the overlapped regions is also provided.

Table 7. Stratford Nozzle U-Velocity Repeatability Summary

Stratford Nozzle Overlapping Windows	Normalized 95% Confidence Interval			Average U Velocity (m/sec)
	MIN	MAX	Average	
A-B-E-F	7.01%	70.97%	28.65%	1.859 ± 0.53
B-C-F-G	3.33%	26.57%	8.08%	2.566 ± 0.21
C-D-G-H	25.78%	60.46%	40.68%	2.807 ± 1.14
B180-C180-F180-G180	3.27%	19.89%	10.40%	2.084 ± 0.22
C180-D180-G180-H180	7.27%	38.44%	22.27%	2.554 ± 0.57

Table 8. Stratford Nozzle V-Velocity Repeatability Summary

Stratford Nozzle Overlapping Windows	Normalized 95% Confidence Interval			Average V Velocity (m/sec)
	MIN	MAX	Average	
A-B-E-F	43.23%	101.94%	62.17%	-1.291 ± 0.80
B-C-F-G	23.77%	37.41%	31.16%	-2.615 ± 0.82
C-D-G-H	4.14%	28.50%	19.77%	-3.344 ± 0.66
B180-C180-F180-G180	15.95%	40.25%	23.64%	2.751 ± 0.65
C180-D180-G180-H180	8.91%	39.80%	18.84%	3.462 ± 0.65

Table 9. Bell Nozzle U-Velocity Repeatability Summary

Bell Nozzle Overlapping Windows	Normalized 95% Confidence Interval			Average U Velocity (m/sec)
	MIN	MAX	Average	
A-B-E-F	10.24%	12.58%	10.96%	2.121 ± 0.23
B-C-F-G	10.07%	16.00%	11.79%	2.058 ± 0.24
C-D-G-H	9.84%	12.01%	10.57%	2.279 ± 0.24
B180-C180-F180-G180	15.37%	66.92%	52.77%	1.433 ± 0.76
C180-D180-G180-H180	13.77%	36.57%	24.45%	1.912 ± 0.47

Table 10. Bell Nozzle V-Velocity Repeatability Summary

Bell Nozzle Overlapping Windows	Normalized 95% Confidence Interval			Average V Velocity (m/sec)
	MIN	MAX	Average	
A-B-E-F	1.32%	5.91%	4.12%	-2.730 ± 0.11
B-C-F-G	1.32%	6.49%	2.79%	-3.634 ± 0.10
C-D-G-H	1.68%	3.00%	2.41%	-4.27 ± 0.10
B180-C180-F180-G180	5.81%	39.06%	21.00%	3.249 ± 0.67
C180-D180-G180-H180	1.60%	8.65%	4.39%	3.845 ± 0.17

The Stratford nozzle PIV data was less repeatable than the Bell nozzle data. The Bell nozzle PIV data in the 0° plane was the most repeatable data. This is consistent with the general observations made elsewhere in this report.

3.4.5. Comparison of Stratford and Bell PIV Data

In this section, observations made in previous sections from the PIV data plotted independently, are summarized first. Further observations are then made from concurrent plotting of the PIV data.

3.4.5.1. Summary of Observations from PIV Data Plotted Independently

The Stratford nozzle PIV data from the 180° plane was smoother than that from the 0° plane. The C window measurements were particularly poor due to seeding difficulties. The Bell nozzle PIV data from the 0° plane was smoother than that measured in the 180° plane. The Bell nozzle's C window's measurement quality was much improved relative to the Stratford's C window, but is still of relatively lower quality than the neighboring windows within the Bell data. The highest PIV measured entrained flow velocity for the Stratford nozzle was in the 180° plane. For the Bell nozzle it was in the 0° plane.

Qualitatively the entrainment flowfields were similar. Both exhibit an acceleration of the entrained flow near the nozzle exit and a more gradual acceleration of the entire flowfield with axial station (as the flowfield approaches the plume capture pipe).

In the regions near the nozzle exit, the maximum PIV measured entrained flow velocity for the Stratford nozzle was lower than the Bell nozzle. The Stratford PIV data indicates the U and V-velocity components of the entrained flow peaked about 25 and 50mm downstream of the nozzle exit, respectively. The Bell PIV data indicates the U and V-velocity components peaked at about X=-10 and 10mm, respectively. The Bell nozzle flow separated just upstream of the nozzle exit inducing reverse flow into the nozzle. This reversed flow is the reason the Bell nozzle's entrained flow velocities peaked closer to the nozzle exit than the Stratford.

The effect of the acceleration near the nozzle exits on entrained flow is discernable in the PIV data in both the axial and radial directions. In the axial direction it is visible to about 125mm downstream of the nozzles. In the radial direction it is visible; for the Stratford, out to a radius of about 134mm, or 114mm beyond the nozzle outer diameter; for the Bell, out to a radius of about 227mm, or 145mm beyond the nozzle outer diameter.

3.4.5.2. Observations from PIV Data Plotted Concurrently

The following paragraphs show that the two different nozzles induced different entrained flows near the nozzle exits, but the entrainment flowfield for the majority of area within the PIV measurement field was very similar.

Figure 65 compares the Stratford 180° plane and the Bell 0° plane PIV data at four similar distances ('dy') from the respective nozzle outer diameters. The comparison was

done at these dy distances to compensate, approximately, for the different nozzle sizes. The Stratford 0° plane data is used in two places to compensate for bad or missing data from the 180° plane.

The differences in the entrained flows near the nozzle exits are apparent between X=-100 and 125mm. The different axial locations of the peak measured velocities are clearly visible. Although not indicated by these curves, the Bell nozzle's entrained flow velocities were, in fact, higher than the Stratford's. These differences can be attributed to the following list of differences in expansion of nozzle flow by the Stratford and Bell nozzles.

- The Stratford and Bell nozzles had inlet pressures of 10.35 and 19.65atm, respectively.
- When expanded to ambient pressure (with isentropic equations), the plume Mach numbers were 2.2 and 2.6, respectively.
- The Bell nozzle mass flow was approximately 2.3 times that of the Stratford nozzle.
- The Bell nozzle's plume cross-sectional and surface areas were 1.8 and 1.33 times that of the Stratford nozzle's plume.
- The Stratford nozzle was underexpanded, whereas, the Bell nozzle was overexpanded to the point of causing its flow to separate from the nozzle wall. This separation induced a sub ambient pressure region which induced a reverse flow into the Bell nozzle.

Figure 65 also shows the similarities of the entrained flowfields for the majority of the area measured (i.e., outside of the region near the respective nozzle exits). At the second and third radii plotted (the red and green lines, respectively), the entrained flow velocities were very similar downstream of X=125mm. By the third radii the entrained flow velocities were becoming more similar upstream of X=125mm. These third radii are approaching the outer radii to which the Stratford and Bell nozzles affected the flow near the nozzle exit. At the fourth radii (the blue lines), well off the centerline and out of the nozzle exit effect, the entrained flow velocities were nearly identical.

Figure 65, and this previous discussion of it, clearly shows that the Stratford and Bell nozzles did induce different entrained flows near the nozzle exit. But outside that region, the entrained flows were strikingly similar, especially, considering the long list of differences (given above) between the nozzles and their plumes.

Now, in Figure 66, the entrained flow velocities for both nozzles are compared at constant axial stations. The Stratford PIV data is plotted on the right hand ordinate axis which was scaled to put both nozzles' outer diameters at the same relative Y location. The peak velocities were different near the plume shear layer but the entrained flow velocities further from the centerline were quite similar (the differences at the outer edge of the profiles is discussed later in this subsection). The velocity profiles become more similar as they approach the plume capture pipe.

One exception was the X=300mm profile. Because the nozzle exits were not in the same axial location with respect to the plume capture pipe (the Stratford nozzle exit was 31.75mm closer), the axial stations shown are not the same distance upstream from the plume capture pipe. To compensate for this for the 300mm profile, an additional profile was plotted from the Stratford nozzle data that was at the same location, relative to the plume capture pipe, as the Bell's X=300mm profile. The agreement improved significantly.

Figure 66 has again shown the entrained flow velocities, outside the plume shear layer, were strikingly similar. The velocity profiles became more similar as they approached the plume capture pipe.

From these observations about the entrained flow's velocities relative to the plume capture pipe, it appears the plume capture pipe sink was a fairly strong influence on the entrained flowfield. And that its effect on the entrained flow was similar for the two nozzles.

Unsteady Layer Not From Vortex Shedding

The unsteady layer's effect on the PIV measured velocity magnitude is visible in the lower image of Figure 66. The inflection near the top of the velocity profiles marks the radial location of the unsteady layer's lower edge. For the Stratford nozzle, in its global coordinate system, this was a radius of approximately 260mm; for the Bell nozzle, in its global coordinate system, approximately 340mm. Note, as indicated in Figure 66, this was at roughly the same radial distance relative to the nozzles' outer diameters. This is further indication that the unsteadiness was not due to vortex shedding from some upstream hardware, but was due to some other, as of yet unexplained, flow instability.
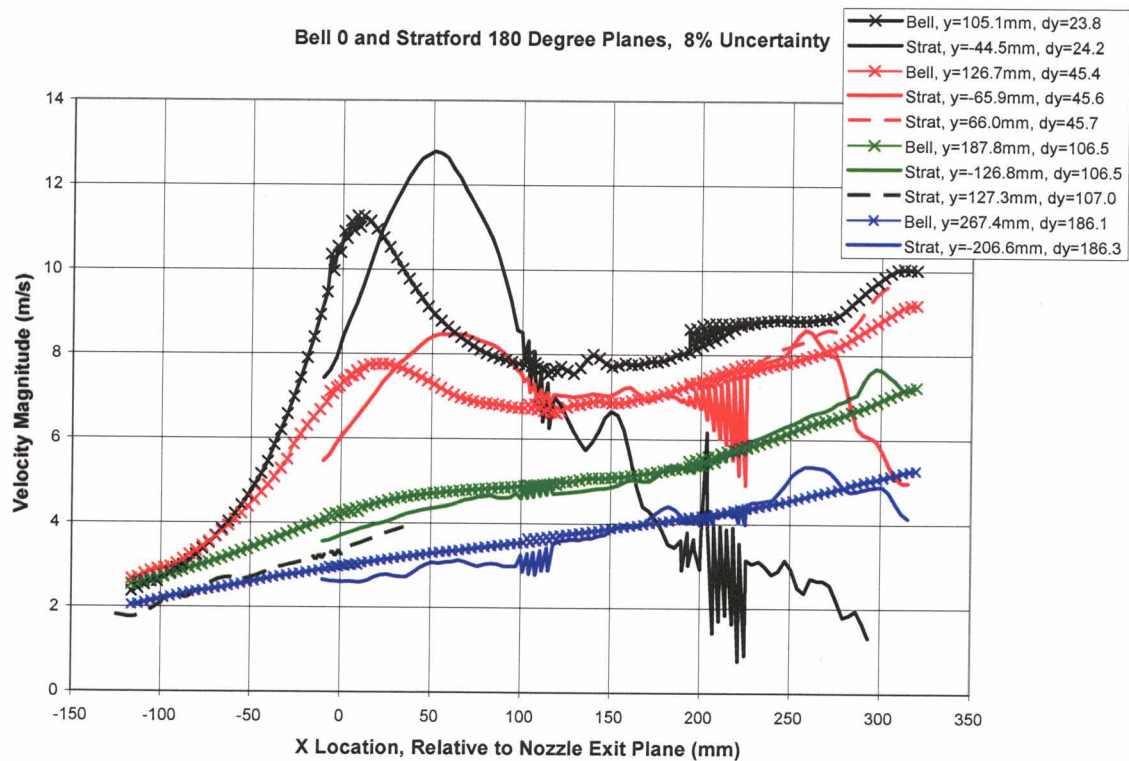
Figure 65. Comparison the Stratford and Bell Nozzle PIV Measured Velocities, for Constant Radial Stations, at Common Distances from the Nozzle Outer Diameter.
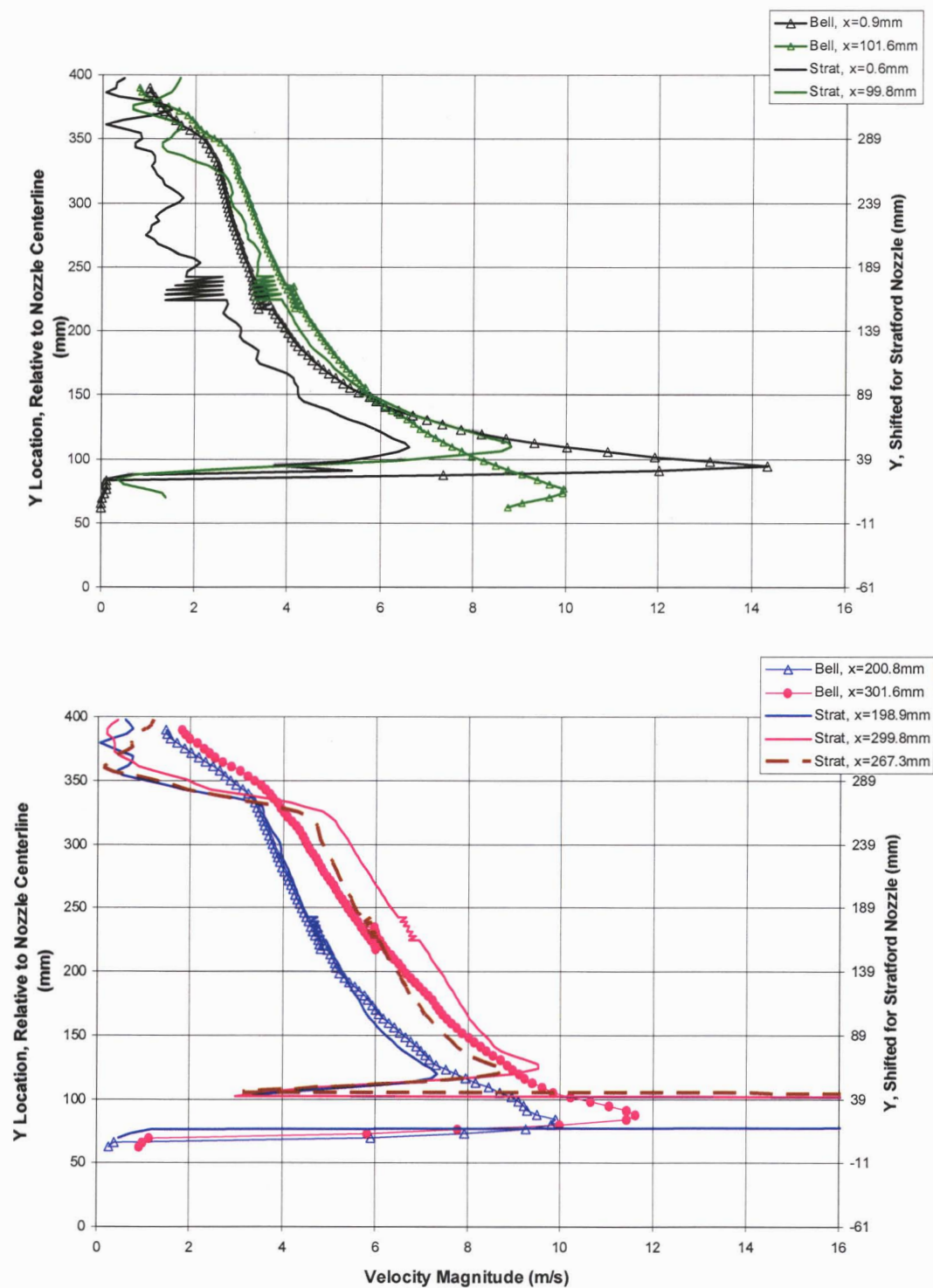
Figure 66. Comparison the Stratford and Bell Nozzle PIV Measured Velocities, at
Constant Axial Stations, at Common Distances from the Nozzle Outer Diameter.

3.4.6. PIV Data Files

The electronic media associated with this report contains all PIV datasets and associated Excel files used to manipulate it. It also contains a few key TecPlot 'layout' files for plotting the data. The Bell and Stratford data structure and processing was very similar. The Bell nozzle files are described here. In these files the Stratford nozzle is at times referred to as the 'Sonic' nozzle.

The PIV data for each nozzle is in its own folder. The majority of it was imported into Excel for processing, for either merging within a window or weaving an entire plane of data together. The top level Excel files 'BellPIVDataSorted8.8pct.xls (and SonicPIVDataSorted8.8pct.xls) contain the merged and woven data for the 0°and 180° planes. It has worksheets containing the data and worksheets containing plots of the data. The data worksheets sort the PIV data at both constant axial and radial stations. This is the 'woven' data. The cells in those data worksheets reference another file, BellPIVData5.8pct.xls (SonicPIVData5.8pct.xls). It is in this file where the merging of the data in the inner rows of windows is preformed. The uncertainty criterion is set in cell U8 in the BellPIVData5.8pct.xls file.

The worksheets containing plots in BellPIVDataSorted8.8pct.xls were used to create the line plots used within this report. They will be updated automatically if the uncertainty criterion is changed.

The data worksheets of BellPIVDataSorted8.8pct were exported to create the TecPlot '.dat' data files. These .dat data files are included as well.

3.5.   Hot Film Anemometer Velocity Data

The hot film anemometer (HFA) data was pursued as a second set of data on the flow entrainment. The intent of the HFA was to:

- To provide a dataset to fall back on if the PIV measurements were not successful.
- To assist in interpreting the PIV measurement.
- Obtain data over a larger area than was possible with the PIV technique. The measurement area in each plane was larger and data in the 90° plane was also obtained.

The hot film anemometer wire was aligned to measure the radial component of velocity. No measurements were made with the HFA wire aligned to measure the horizontal, or U, component of velocity. The HFA technique only indicates a velocity magnitude. Direction of the velocity must be inferred from the probe orientation. The HFA velocity magnitude is presented as a positive value in all three planes. It is not assigned a direction (+ or -) based on the global coordinated systems Y axis. The HFA velocity data for the Stratford nozzle is discussed first. The HFA velocity data for the Bell nozzle is then discussed. The order and format in which the data are presented is very similar for both nozzles and is as follows. First, notes about the test data and the relative positions of the 'windows' are discussed. The HFA velocity field is then discussed. The HFA data for the two nozzle flowfields are compared. Then the HFA data is compared to the PIV V-velocity data.

The HFA velocity data agreed well with the PIV data. The HFA data provided additional insight to the plume capture pipe sink's effect on the entrained flow.

3.5.1. Data Taken

Position of Stratford Nozzle HFA Measurement Windows

A schematic of the HFA measurement regions, or windows, for the Stratford nozzle is shown in Figure 67. Four windows were obtained in the 0°, 90° and 180° planes.

Each window is 300 by 300mm. Measurements were taken every 20mm for a total of 256 measurement points in each window. Between runs the traverse was manually translated to the next window position, allowing for 100mm of overlap between the adjacent windows.

The net HFA measurement area was much larger than the PIV measurement area. For comparison, Figure 69 indicates the PIV measurement area on a set of HFA data.

The A window in each plane was positioned relative to the nozzle exit. The lower edge of the measurement region was set to be 25.4mm above the outer diameter of the nozzle at its exit. The left most edge of window A was limited by the Stratford nozzle shape. The left most edge of the A (and D) window was 40mm upstream of the nozzle

exit. The remaining windows in each plane were located by moving the traversing (and/or the rail system supporting it) a known distance relative to the A window.

Coordinate transformation were performed to locate each windows in the Stratford nozzle's global coordinate system. The transformations are noted in the Excel data files which contain the Stratford HFA test data. This Excel data files are described in Section 3.5.7. Note that the Stratford and Bell nozzle global coordinate systems are different.

Position of Bell Nozzle HFA Measurement Windows

A schematic of the HFA measurement regions, or windows, for the Bell nozzle is shown in Figure 68. Five windows were obtained in the 0° and 90° planes and four were obtained in the 180° plane. Each window is 300 by 300mm. Measurements were taken every 20mm for a total of 256 measurement points in each window. Between runs the traverse was manually translated to the next window position, allowing for 100mm of overlap between the adjacent windows.

The net HFA measurement area was much larger than the PIV measurement area. For comparison, Figure 73 indicates the PIV measurement area on a set of HFA data.

The A window in each plane was positioned relative to the nozzle exit. The lower edge of the measurement region was set to be 25.4mm above the outer diameter of the nozzle at its exit. The left most edge of the A (and D) window was 140mm upstream of the nozzle exit. The remaining windows in each plane were located by moving the traversing (and/or the rail system supporting it) a known distance relative to the A window. The right hand edge of the C window was 30mm from the plume capture pipe.

Coordinate transformations were performed to locate each window in the Bell nozzle's global coordinate system. The transformations are noted in the Excel data files which contain the Bell nozzle HFA test data. These Excel data files are described in Section 3.5.7. Note that the Stratford and Bell nozzle global coordinate systems are different.

Notes from Run Logs

Table 11 is a summary of the HFA test log. It was easier to change the nozzle test articles than it was to change the hot film traverse system and the rail system supporting it. Therefore, the test and instrumentation setup are listed in a chronological order instead of by nozzle.

Table 11. Summary of HFA Run Log

Date	Time	Nozzle	Window	Plane	Comment
2/22/2005	2:40	Bell	A	0	initial set-up with traverse on top of horizontal rail
2/23/2005	10:00	Bell	B	0	slide traverse, rail doesn't move
2/23/2005	1:50	Bell	C	0	slide traverse, rail doesn't move
2/24/2005	9:30	Bell	E	0	raise rail and slide traverse
2/24/2005	12:45	Bell	D	0	slide traverse
2/25/2005	10:20	Bell	A	180	lower rail and slide traverse
2/25/2005	12:30	Bell	B	180	slide traverse
2/28/2005	10:00	Bell	D	180	flip traverse to underside of rail to get planes close to floor
2/28/2005	1:30	Bell	E	180	slide traverse
3/1/2005	8:45	Stratford	A	180	install sonic nozzle - start with upside down traverse for all 180
3/1/2005	9:20	Stratford	B	180	OSC warning light at top 2 rows (Y=-45.7 and -65.7) in the 5 most downstream positions (X=380 to 460)
3/1/2005	1:00	Stratford	E	180	lower rail
3/1/2005	1:30	Stratford	D	180	slide traverse
3/2/2005	9:30	Stratford	A	0	probe wire broke while reconfiguring for 0 deg plane - calibrate new wire
3/2/2005	10:30	Stratford	B	0	slide traverse
3/2/2005	12:30	Stratford	E	0	raise rail
3/2/2005	1:00	Stratford	D	0	slide traverse
3/3/2005	8:30	Stratford	A	90	reconfigure for 90 deg plane - OSC warning light at (X=260, Y=45.7) position
3/3/2005	10:00	Stratford	B	90	OSC warning light at (X=440, Y=45.7) & (X=460, Y=45.7) positions
3/3/2005	11:00	Stratford	E	90	move rail
3/3/2005	1:00	Stratford	D	90	slide traverse
3/4/2005	10:30	Bell	A	90	install bell nozzle - facility data inadvertently not recorded for this run
3/4/2005	12:40	Bell	B	90	slide traverse
3/4/2005	2:15	Bell	C	90	slide traverse - OSC warning at (X=540, Y=106.6)
3/7/2005	9:00	Bell	E	90	move rail
3/7/2005	11:00	Bell	D	90	slide traverse

The 'OSC' warning light mentioned in the comment column in Table 11 for several runs refers to a feature of the TSI Intelligent Flow Analyzer that indicated when the probe was in a highly oscillatory flow. It served as a warning to look at the turbulent intensity for those data points as well as real-time feedback to avoid damaging the probe. The warning light only went off when the probe was in or near the plume shear layer.

The most significant item from the run logs was the probe change that occurred on 3/2/2005. The delicate wire of the hot film probe broke during a configuration change and had to be replaced. The replacement probe tip was calibrated in the same probe shaft and using the same calibration procedure. Testing proceeded without any noticeable problems. Unfortunately, differences between the probes later turned out to be significant. This only became apparent post test when comparing HFA and PIV data (Section 3.5.6). With nothing suspicious about the calibration of this second probe, its

disagreement with the rest of the data is attributed to the stack up of uncertainties associated with this HFA measurement technique.
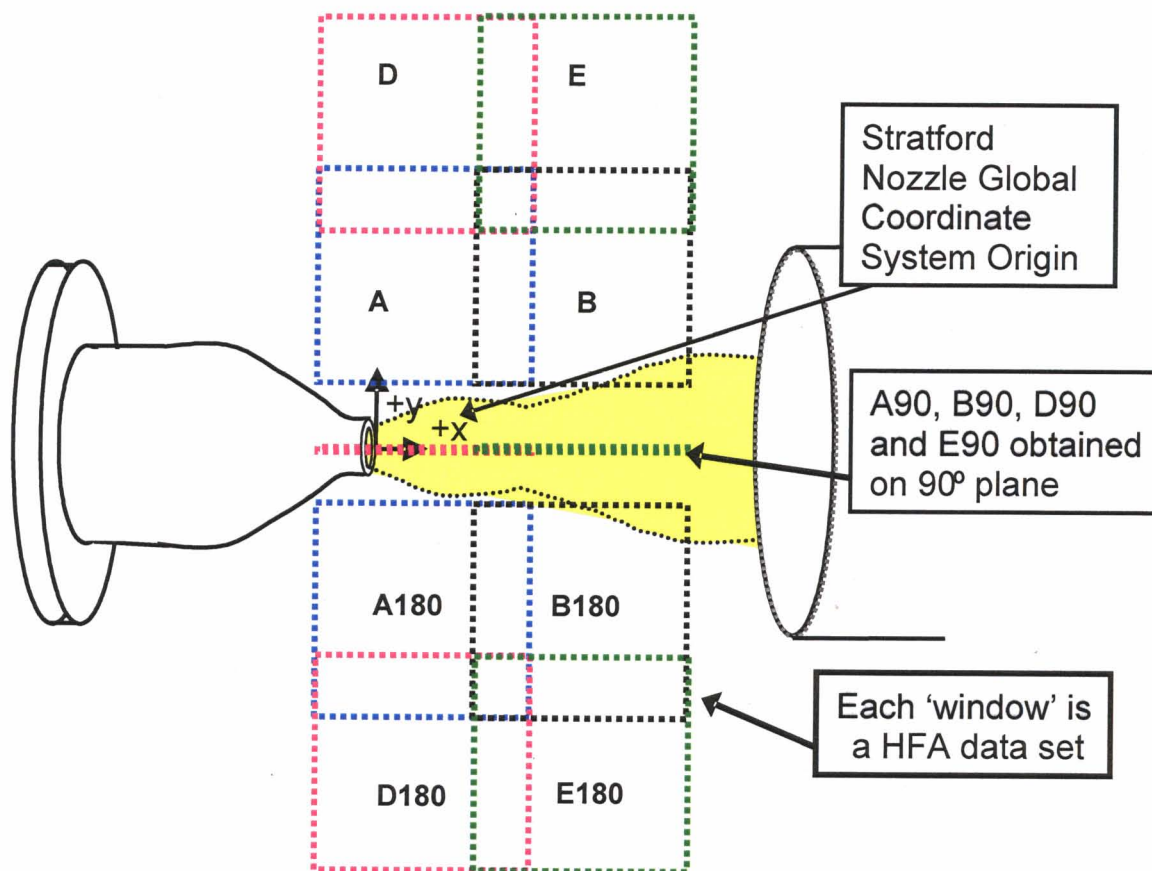
Figure 67. Schematic of HFA Datasets Acquired for the Stratford Nozzle.
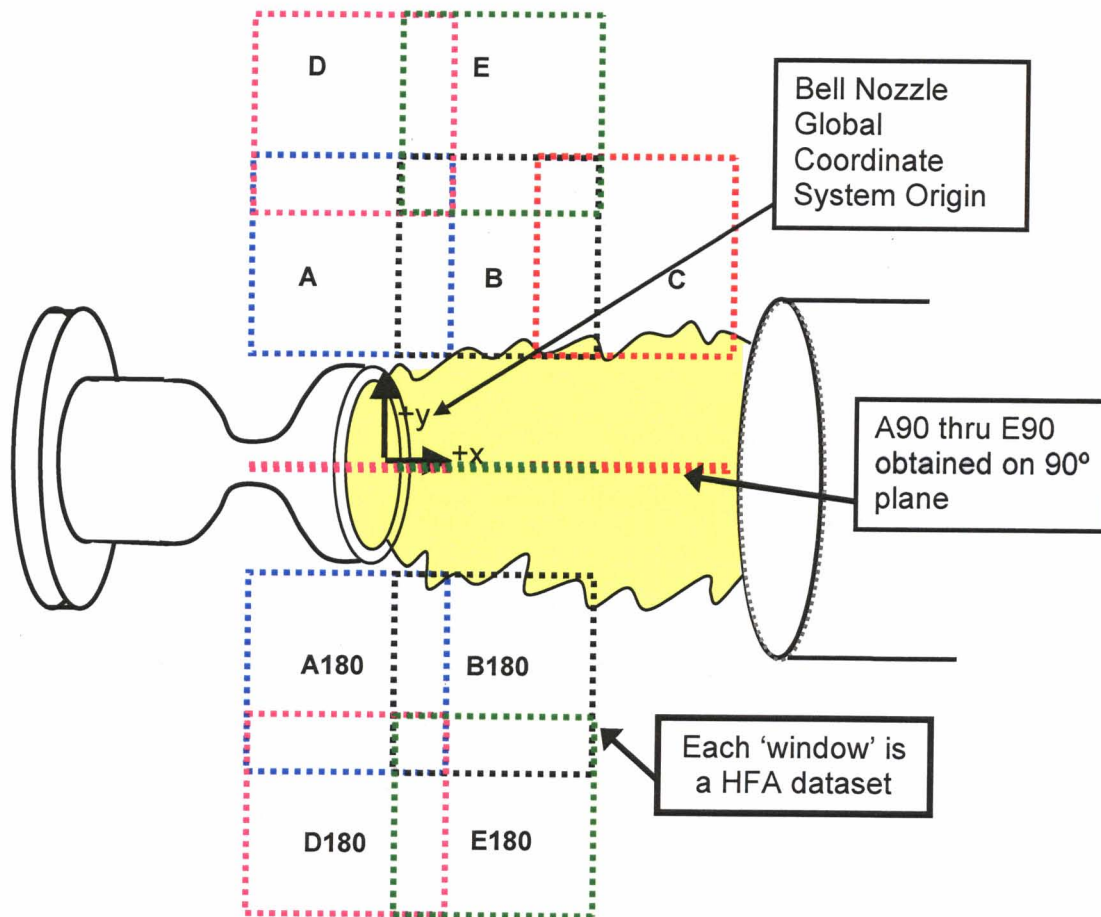
Figure 68. Schematic of HFA Datasets Acquired for the Bell Nozzle.

3.5.2. Stratford Nozzle HFA Velocity Data

Only one set of HFA measurements were made for each window. The HFA data from all windows was sorted in Excel to 'weave' the data together into one continuous set of data. The spacing of the HFA windows and data points within the windows was such that data points in the overlapped regions were at the same physical locations. For those coincident data points, an average value was calculated.

Velocity Contour Plots

Figure 69 presents the Stratford nozzle data for the 0 and 180° plane and Figure 70 presents the same 0° plane of data but with the 90° plane of data. The HFA velocity magnitude contours appear quite similar in all three planes, particularly the 0 and 90° planes. The contours indicate the 180° plane had consistently lower velocities. As will be explained in Section 3.5.6, the velocities shown in the 180° plane are probably a more accurate representation of the entrained radial velocity component and the 0 and 90° plane HFA velocity magnitudes were probably higher than the true radial velocity.

The indicated high velocity near the centerline is the plume shear layer. The indication of high velocity is correct, but the velocity magnitude indicated by the HFA probe is not accurate data. The probe was aligned to measure the radial component, but the axial component of the shear layer was two orders of magnitude larger than the radial component. See the vectors in Figure 34. With such large cross flows, the single wire HFA probe hardware used in this experiment could not provide accurate velocity data.

The indicated high velocity on the right hand side of the measurements is the plume capture pipe sink. Figure 45 shows vectors of the sink flow near the pipe. The sink induced flow was predominately radial velocity flow in this location; therefore, these high indicated velocity magnitudes were not a result of axial cross flow.

Velocity Line Plots

Line plots of the HFA velocity magnitude at constant radial stations are now presented. The radial stations for these line plots are shown in Figure 71. The following line plots were created in an Excel file that is included in the electronic media associated with this report. The data plotted here can be extracted from that Excel file. This Excel file can be used to create additional line plots at alternate radial stations. Section 3.5.7 discussed HFA Excel data files.

Figure 72 plots the HFA velocity magnitude along several constant radial stations for the 0, 90 and 180° planes. The saw tooth patterns in the lines are the overlapping regions of adjacent windows. For the line plots, all values at overlapped points were plotted instead of an average value. As with the color contours above, the profiles in the 0 and 90° planes were fairly similar. The profiles in the 180° plane had the same character as those in the 0 and 90 but the magnitude was consistently lower. Again, as explained in Section 3.5.6, the velocities shown in the 180° plane are probably a more accurate representation of the entrained radial velocity component and the 0 and 90°

plane HFA velocity magnitudes were probably higher than the true entrainment radial velocities.

The Y=65.7 and 85.7mm profiles both show the acceleration near the nozzle exit. In the Y=65.7mm profiles, the higher indicated velocities to the right of X=250mm were a result of the shear layer cross flow and are suspect. The rest of the profiles show increasing velocity magnitude with axial station. For the outer profiles this acceleration was apparent over their entire length. This acceleration was mainly due to the sink created by the interaction of the plume and the plume capture pipe. The cause of the plume capture pipe sink is discussed in Section 3.4.1.2.3.
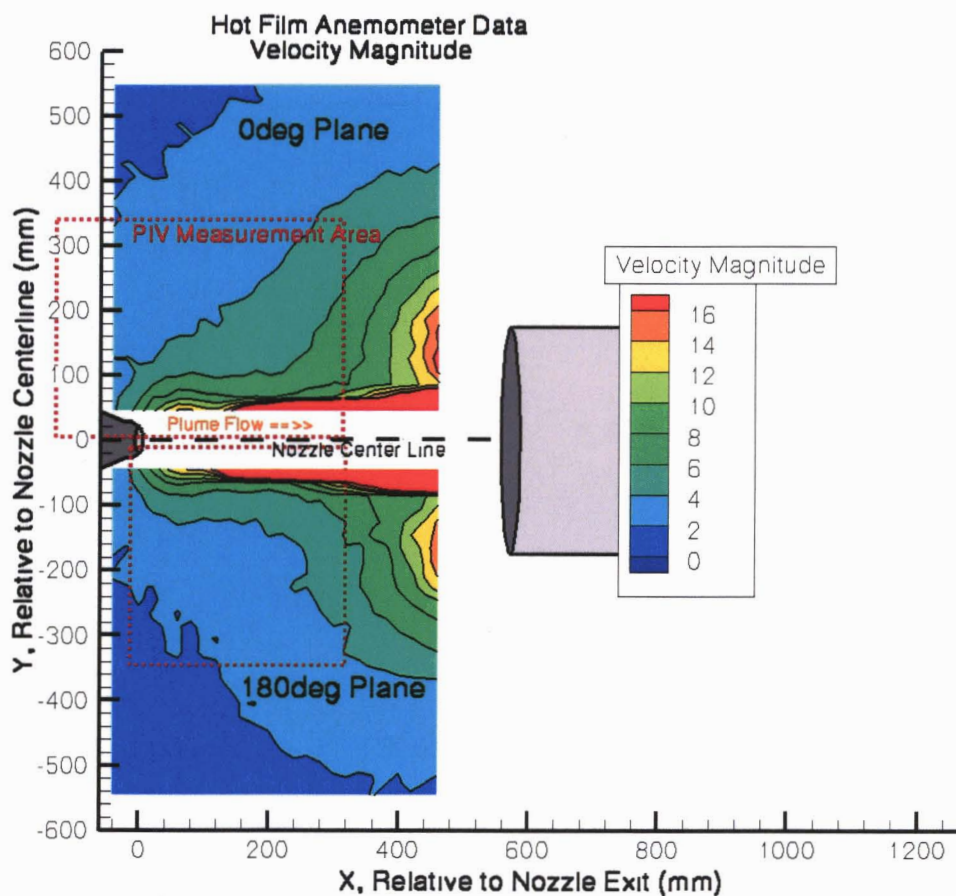
Figure 69. HFA Velocity Magnitude for Stratford Nozzle in the 0° and 180° Plane.
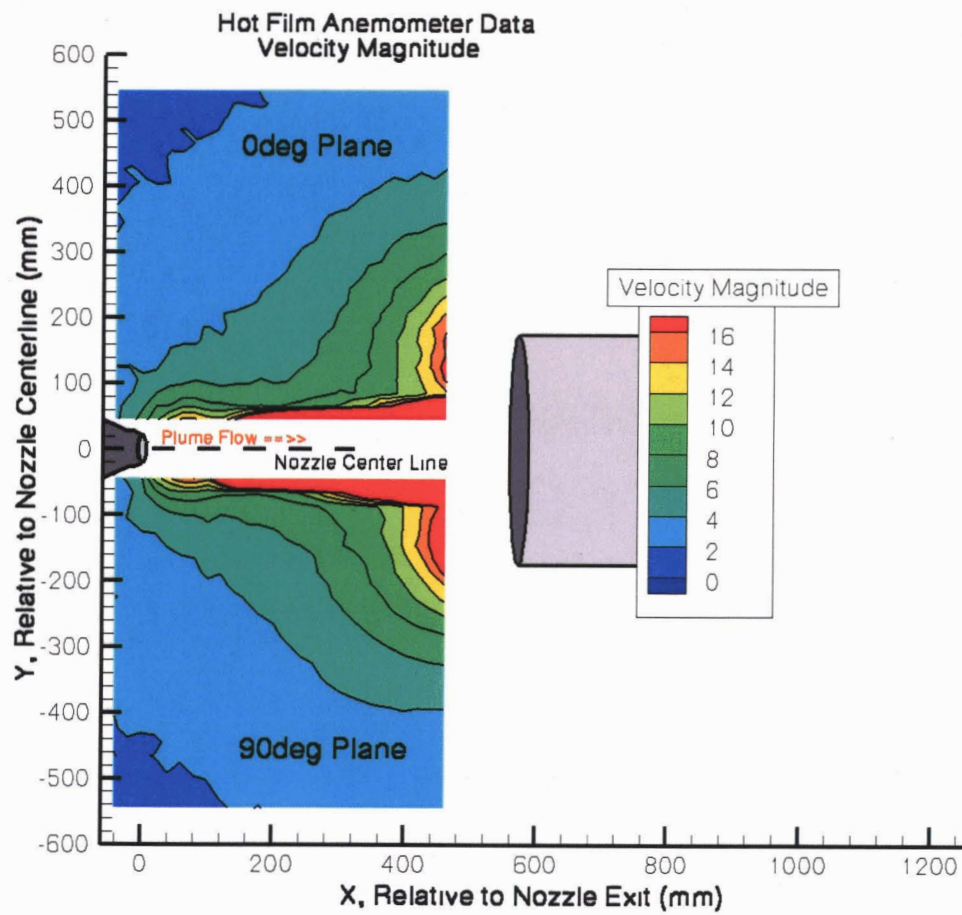
Figure 70. HFA Velocity Magnitude for Stratford Nozzle in the 0° and 90° Plane.
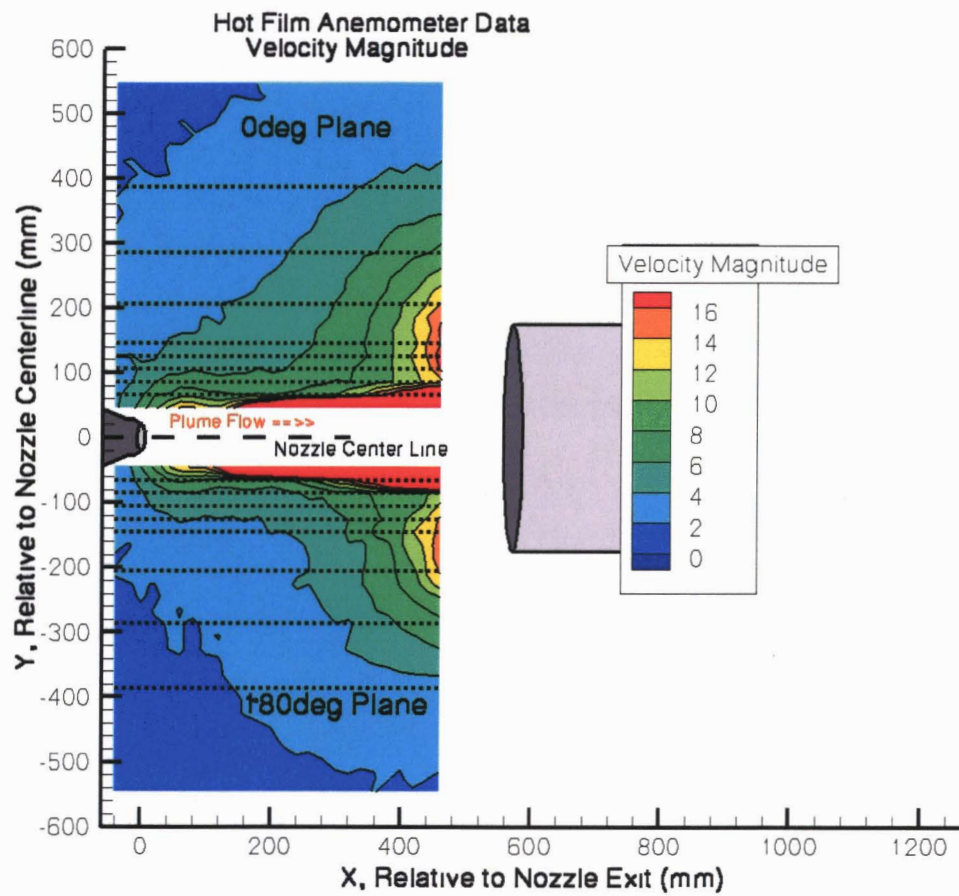
Figure 71. Radial Stations of HFA Velocity Profiles for the Stratford Nozzle.
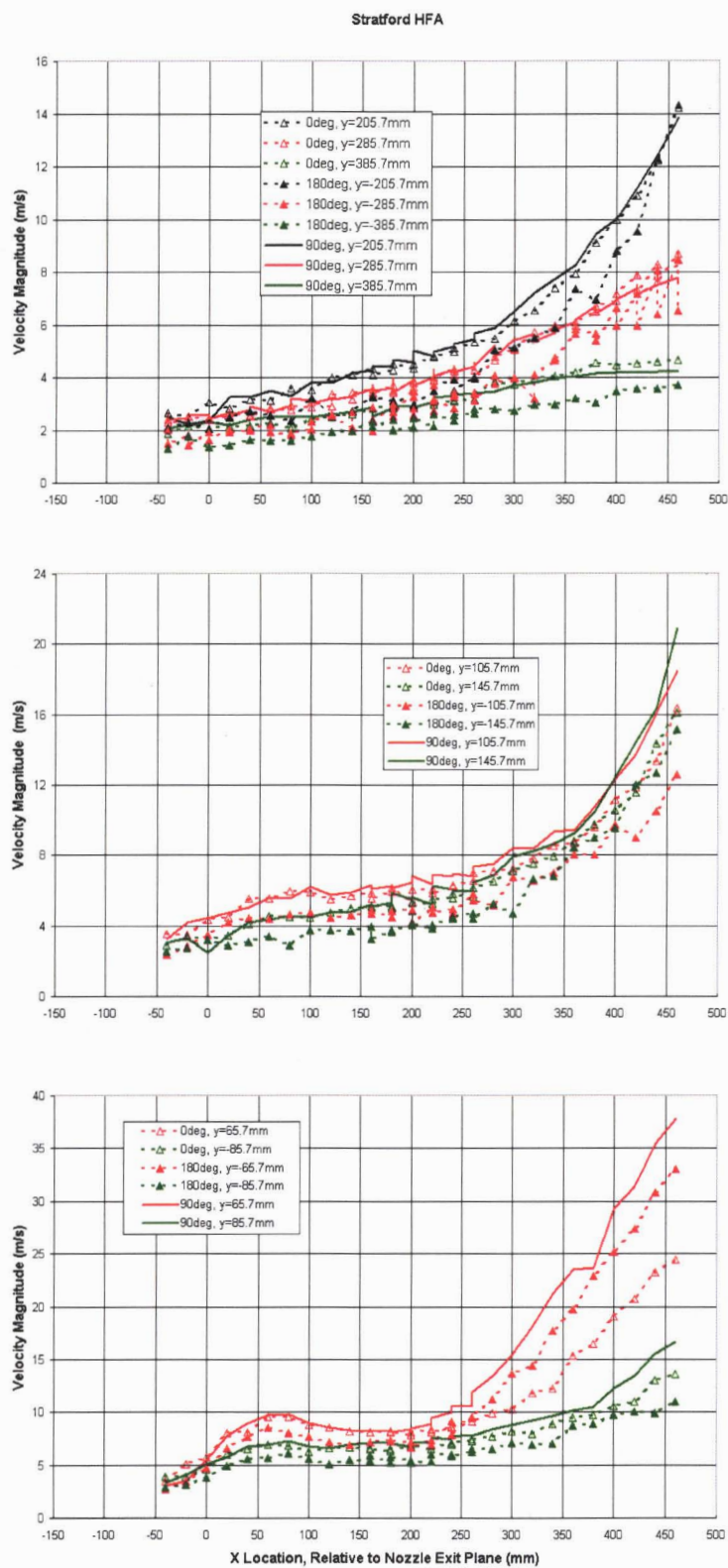
Figure 72. HFA Velocity Magnitude at Constant Radial Stations for the Stratford
Nozzle.

3.5.3. Bell Nozzle HFA Velocity Data

Only one set of HFA measurements were made for each window. The HFA data from all windows was sorted in Excel to 'weave' the data together into one continuous set of data. The spacing of the HFA windows and data points within the windows was such that data points in the overlapped regions were at the same physical locations. For those coincident data points, an average value was calculated.

Velocity Contour Plots

Figure 73 presents the Bell nozzle data for the 0 and 180° plane and Figure 74 presents the same 0° plane of data but with the 90° plane of data. The dark blue in the right hand corners in these figures are regions where no data was taken. The HFA velocity magnitude contours appear quite similar in all three planes. The contours indicate the 90° plane consistently had slightly higher velocity than the 0 and 180° planes. As will be explained in Section 3.5.6, the velocities shown in the 0 and 180° plane are probably a more accurate representation of the entrained radial velocity component and the 90° plane HFA velocity magnitudes were probably higher than the true radial velocity.

In the Bell HFA data the plume shear layer was less of an influence than with the Stratford nozzle data. On the right hand side of data, near the centerline, a small portion of the plume shear layer was captured. The indication of high velocity in the shear layer is correct, but the velocity magnitude indicated by the HFA probe is not accurate data. The probe was aligned to measure the radial component, but the axial component of the shear layer in this region was significantly larger than the radial component. With large cross flows, the single wire HFA probe hardware used in this experiment could not provide accurate velocity data.

The red bubble of high velocity on the right hand side of the measurements is the plume capture pipe sink. Figure 45 shows the vectors of the sink flow near the pipe. The sink induced flow was predominately radial velocity flow in this location, therefore, these high indicated velocity magnitudes were not a result of axial cross flow.

Velocity Line Plots

Line plots of the HFA velocity magnitude at constant radial stations are now presented. The radial stations for these line plots are shown in Figure 75. The following line plots were created in an Excel file that is included in the electronic media associated with this report. The data plotted here can be extracted from that Excel file. This Excel file can be used to create additional line plots at alternate radial stations. Section 3.5.7 discussed HFA Excel data files.

Figure 76 plots the HFA velocity magnitude along several constant radial stations for the 0, 90 and 180° planes. The saw tooth patterns in the lines are the overlapping regions of adjacent windows. For the line plots, all values at overlapped points were plotted instead of an average value. As with the color contours above, the profiles in the 0 and 180° planes were fairly similar. The profiles in the 90° plane had the same

character as those in the 0 and 180 but the magnitude was consistently higher. Again, as explained in Section 3.5.6, the velocities shown in the 0 and 180° plane are probably a more accurate representation of the entrained radial velocity component and the 90° plane HFA velocity magnitudes are probably higher than the true entrainment radial velocity.

The Y=106.7 and 126.7mm profiles both show the acceleration near the nozzle exit. In the Y=106.7mm profiles, the higher indicated velocities to the right of X=275mm were a result of the shear layer cross flow and are suspect. The right hand side of the Y=126.7mm profiles show rapidly increasing velocity. This is not a shear layer effect, but is the plume capture pipe induced radial flow. The rest of the profiles show increasing velocity magnitude with axial station. For the outer profiles this acceleration was apparent over their entire length. This acceleration was mainly due to the sink created by the interaction of the plume and the plume capture pipe. The cause of the plume capture pipe sink is discussed in Section 3.4.1.2.3.
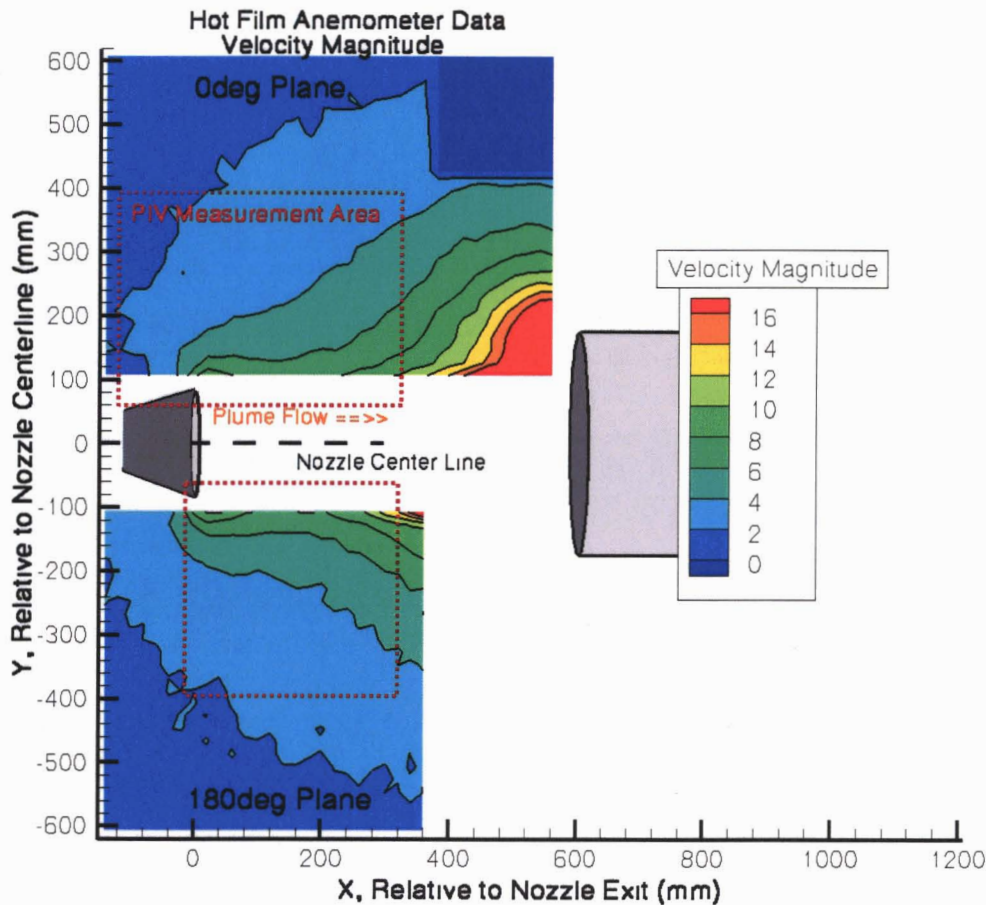
Figure 73. HFA Velocity Magnitude for Bell Nozzle in the 0° and 180° Plane.
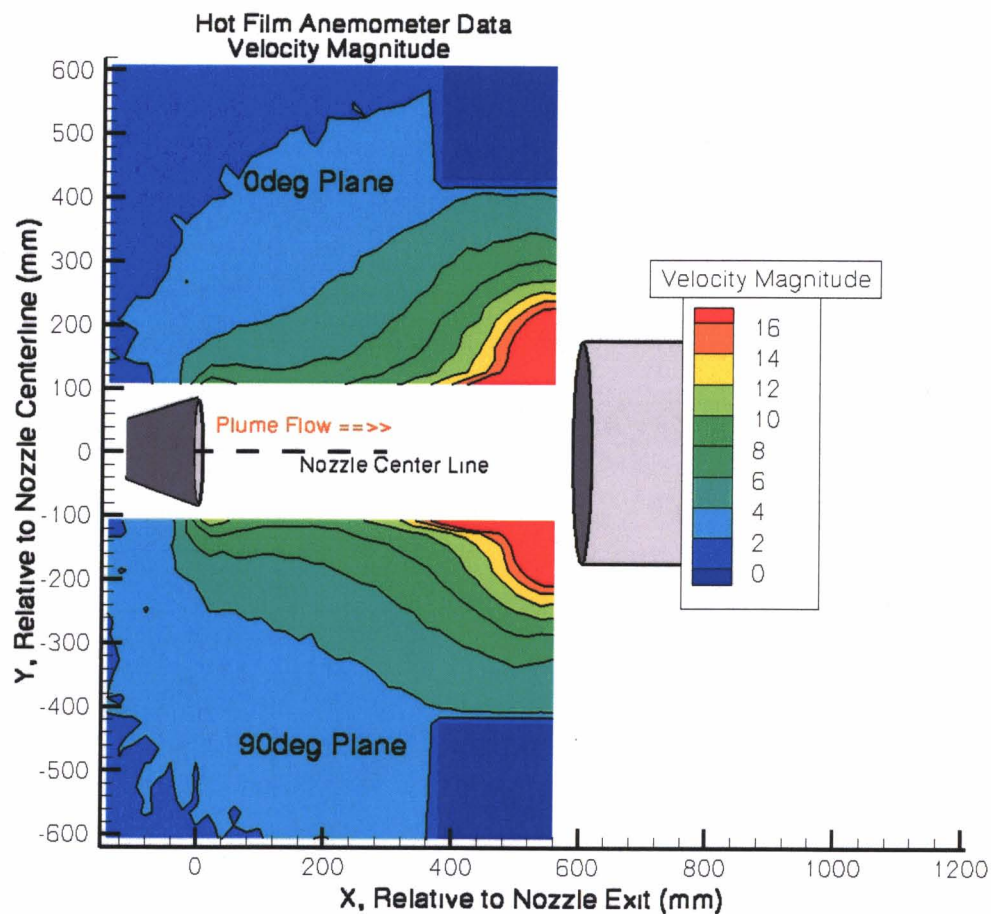
Figure 74. HFA Velocity Magnitude for Bell Nozzle in the 0° and 90° Plane.
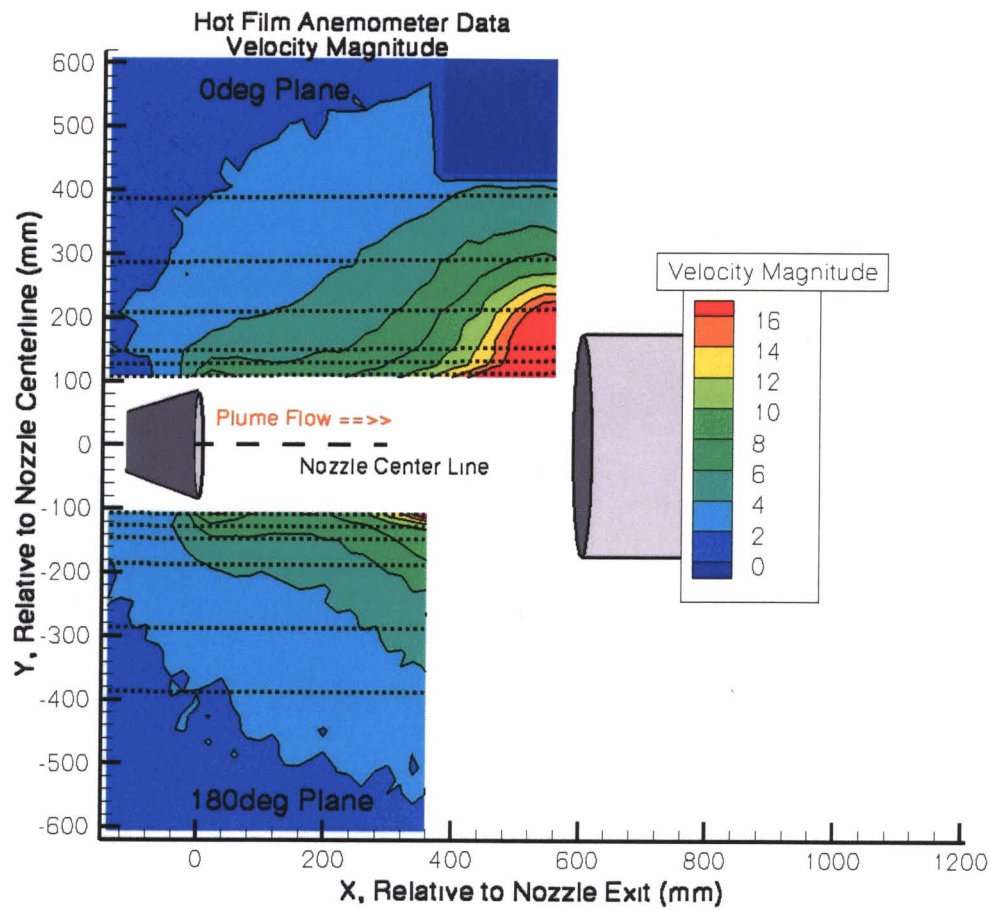
Figure 75. Radial Stations of HFA Velocity Profiles for the Bell Nozzle.
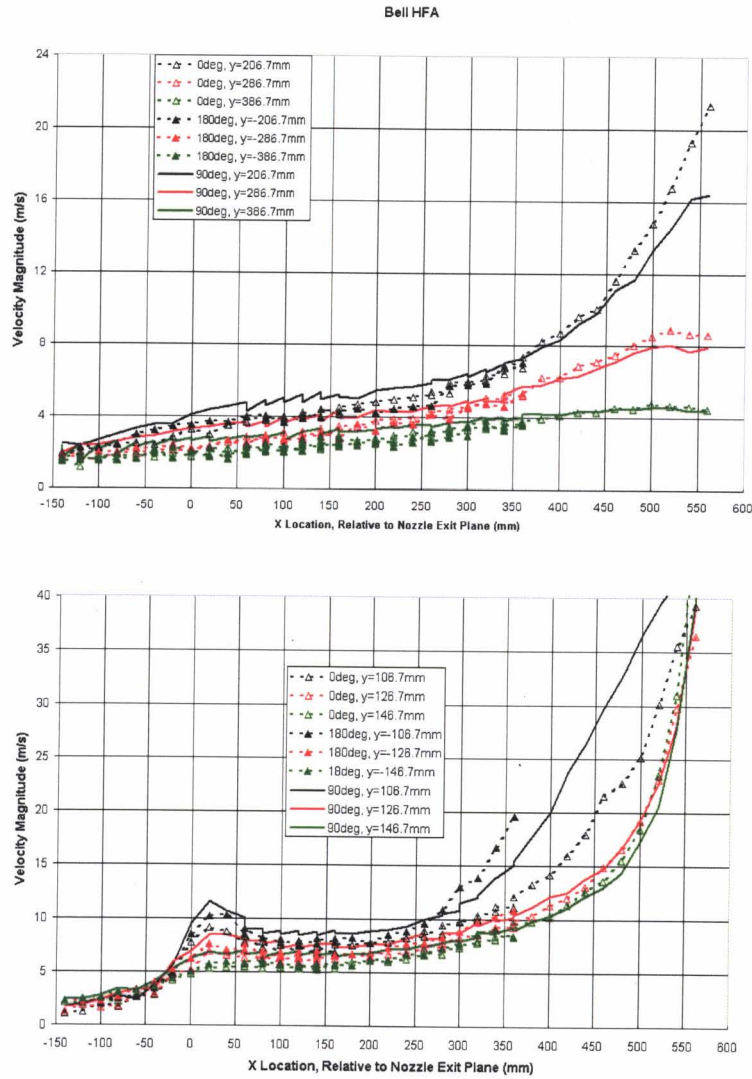
Figure 76. HFA Velocity Magnitude at Constant Radial Stations for the Bell Nozzle.

3.5.4. HFA Measurement Repeatability

The test schedule did not allow repeating HFA measurements in any of the windows. However, the overlapped regions of neighboring windows are effectively five regions where HFA data was obtained multiple times. Therefore, the repeatability of the HFA measured velocities was assessed by comparing the velocities in these overlapped regions of the neighboring HFA datasets. Each window of data was acquired in a separate run of the NTF. The difference in time between acquisition of the datasets was as little as 30 minutes, or as much as a several days. The repeatability of the HFA measurements were affected by at least the consistency of the test conditions (nozzle inlet and ambient) and positional accuracy of the HFA hardware.

Repeatability was assessed by using the data from the regions where three or four windows overlapped. Three overlapped regions were analyzed for Stratford nozzle and five for the Bell nozzle. The Stratford nozzle overlapped regions were the coincident corners of the following sets of windows (see Figure 67); A-B-D-E, A90-B90-D90-E90, and A180-B180-D180-E180. The Bell nozzle overlapped regions were the coincident corners of the following sets of windows (see Figure 68); A-B-D-E, B-C-E, A90-B90-D90-E90, B90-C90-E90, and A180-B180-D180-E180.

Because the data points from the four windows of an overlapped region were at the same locations in the global coordinate systems, the velocity data for each window was compared with the positionally identical values of the other windows. Therefore, each data point location in the overlapping portion had three or four velocity values associated with it respectively. A 95% confidence interval[5] was computed for these three or four sample sets at each point, depending on the number of overlapping windows at each point. The confidence interval was then normalized by the average value at each point. The minimum, maximum and average normalized confidence intervals for all the points in the overlapping regions are presented in Table 12 and Table 13. The dimensional value of the average velocity magnitude of the overlapped regions is also provided.

Table 12. Stratford Nozzle HFA Velocity Magnitude Repeatability Summary

Stratford Nozzle Overlapping Windows	Normalized 95% Confidence Interval			Average Velocity Magnitude (m/sec)
	MIN	MAX	Average	
A-B-D-E	6.81%	43.60%	19.92%	-3.774 ± 0.75
A90-B90-D90-E90	9.65%	106.35%	25.66%	-3.905 ± 1.00
A180-B180-D180-E180	9.61%	72.28%	36.10%	-2.928 ± 1.06

Table 13. Bell Nozzle HFA Velocity Magnitude Repeatability Summary

Bell Nozzle Overlapping Windows	Normalized 95% Confidence Interval			Average Velocity Magnitude (m/sec)
	MIN	MAX	Average	
A-B-D-E	21.08%	66.40%	36.32%	-2.566 ± 0.93
B-C-E	6.61%	60.61%	34.84%	-3.821 ± 1.33
A90-B90-D90-E90	6.14%	42.07%	24.50%	-3.179 ± 0.78
B90-C90-E90	7.87%	79.09%	26.69%	-4.145 ± 1.11
A180-B180-D180-E180	3.47%	91.36%	37.23%	-2.489 ± 0.93

3.5.5. Comparison of Stratford and Bell HFA Data

Although not shown here, the HFA data showed the acceleration of the entrained flow near the nozzle exits were different for the Stratford and Bell nozzles. These differences were similar to the differences shown by the PIV data (Section 3.4.5) for the near nozzle exit region of the Stratford and Bell nozzles.

Figure 77 compares the outer radii profiles of the HFA velocities for the two nozzles. These outer profiles are quite similar in all three planes. The differences due to the acceleration of the entrained flow near the nozzle exits cannot be seen in these outer profiles. Both flowfields show the effect of the plume capture pipe sink; the acceleration of the entire field toward the plume capture pipe.
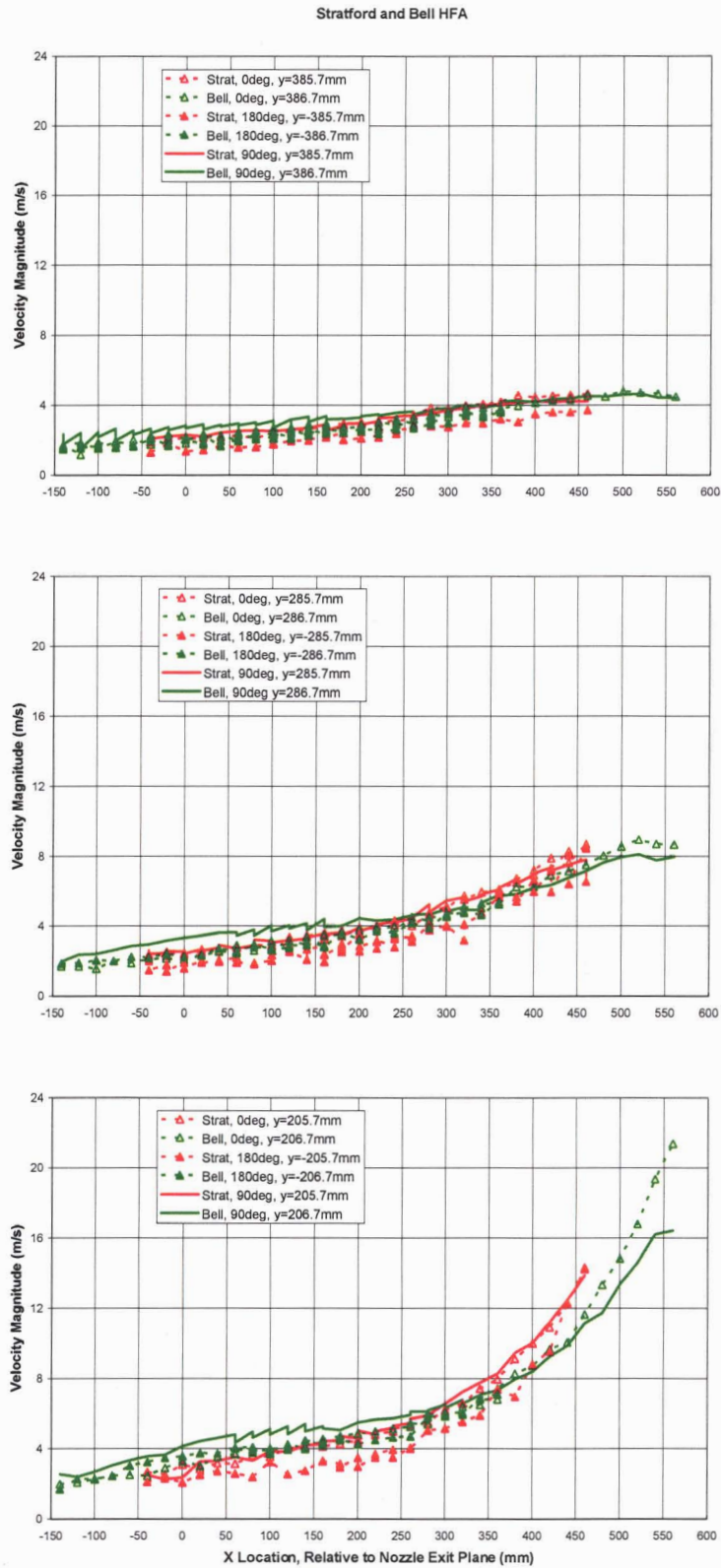
Figure 77. Comparison of Stratford and Bell Nozzle HFA Velocity Magnitude at the
Outer Profiles.

3.5.6. Comparison of HFA Velocity Magnitude and PIV V-Velocity

The HFA and PIV data are compared in the 0 and 180° planes for the Stratford and Bell nozzles. PIV data was not acquired on the 90° planes. Figure 78 plots the HFA velocity magnitude and PIV V-velocity for the Stratford nozzle 0° plane. The trends agree well but the HFA velocity is significantly higher than the PIV V-velocity. This is the only plane in which the two techniques do not agree. The other three planes agree exceptionally well (see Figure 79 through Figure 81).

Two sets of HFA hardware (probe and wire combinations) were used to obtain the HFA data. The particular set used on the Stratford 0° plane was also used to acquire the Stratford nozzle's 90° plane and the Bell nozzle's 90° plane. The velocities recorded with this set of HFA hardware were consistently higher than those recorded (with the other set of HFA hardware) in the other three planes; the Stratford nozzle's 180° and the Bell nozzle's 0 and 180° planes. This is evident in the color contours; Figure 69 and Figure 70, and Figure 73 and Figure 74; and the line plots, Figure 72 and Figure 76.

It appears that HFA velocity magnitudes for the Stratford 0 and 90° plane and the Bell's 90° plane are higher than the true entrainment radial velocities for these planes. This supposition is made because the HFA data in the Stratford nozzle's 180° plane (Figure 79) and the Bell nozzle's 0 and 180° planes (Figure 80 and Figure 81), all made with the other set of HFA hardware, were in excellent agreement with the PIV data.

In these three planes, the only difference between results of the HFA and PIV techniques was at the outer most radial profiles of the Bell nozzle, where the PIV measurements captured the unsteady layer (see Section 3.4.3.) and the HFA did not. One hypothesis for this is that the frequency of the unsteadiness was relatively low. Sufficiently low such that the acquisition rate of the HFA technique, 1024 samples per second, was too high to capture the unsteadiness. The PIV technique acquired data at sufficiently slow rate, 15 samples per second, to capture some of the unsteadiness.
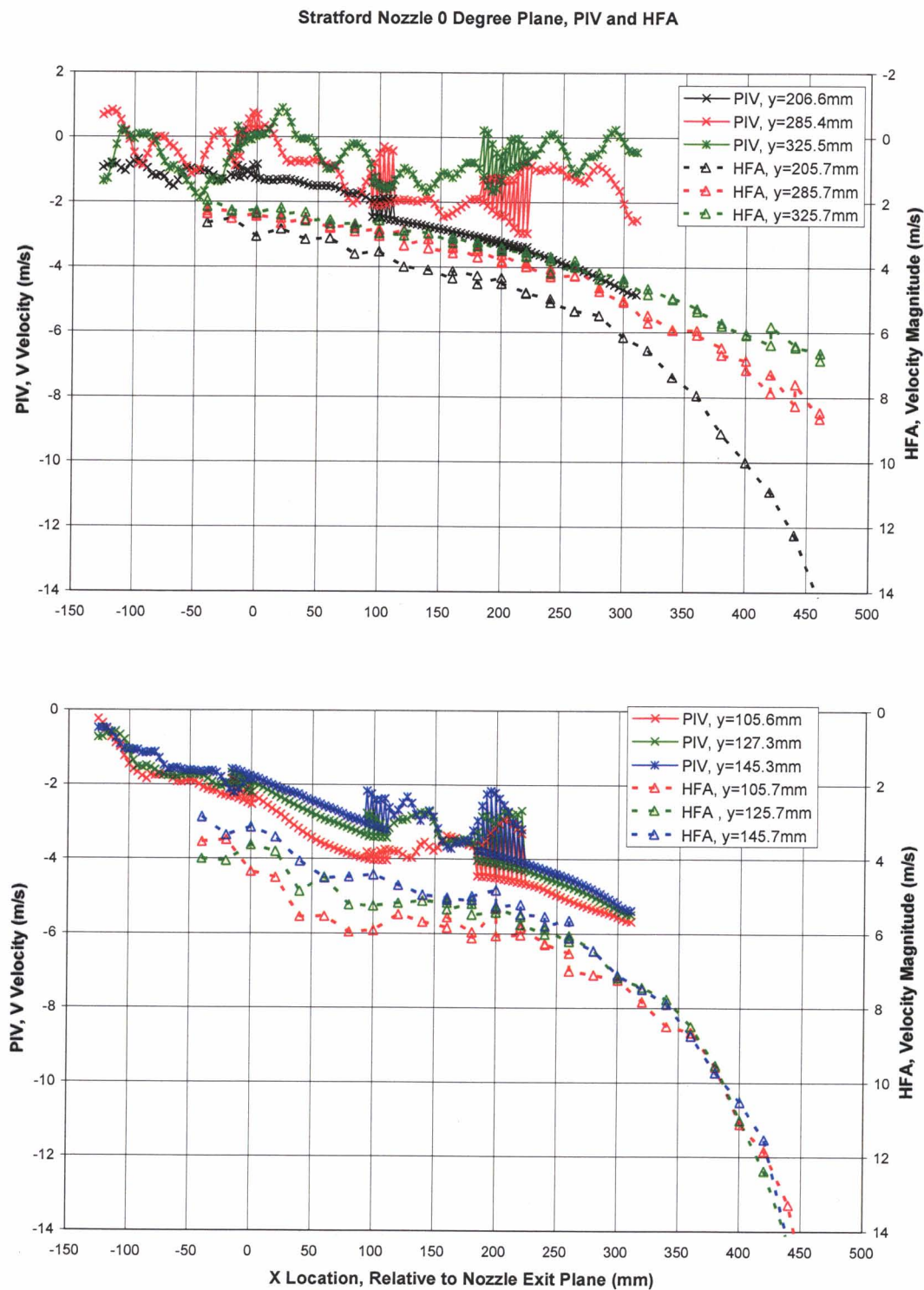
Figure 78. Comparison of HFA Velocity Magnitude to PIV V-Velocity in the Stratford Nozzle 0° Plane.
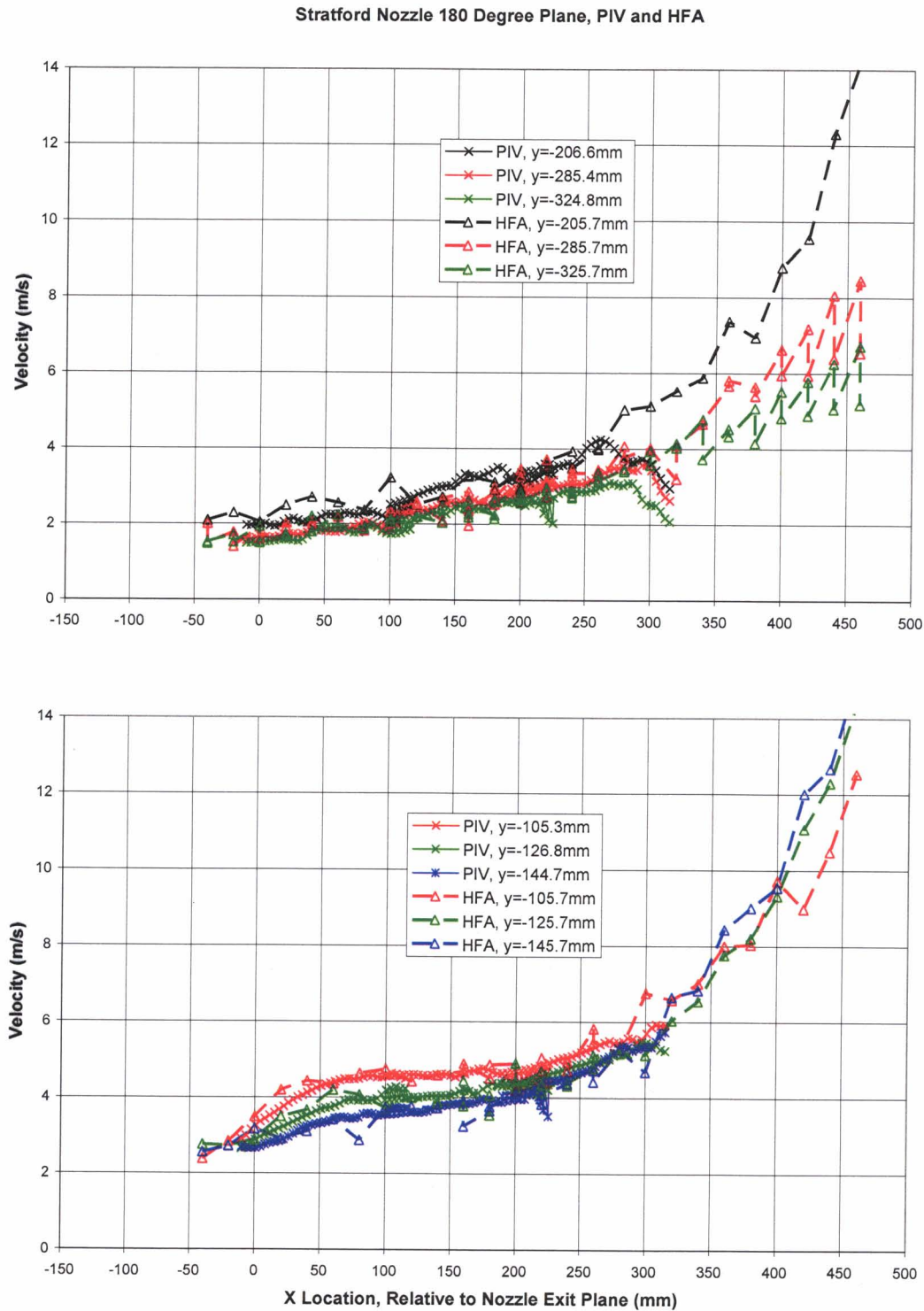
Figure 79. Comparison of HFA Velocity Magnitude to PIV V-Velocity in the Stratford Nozzle 180° Plane.

Bell Nozzle 0 Degree Plane, PIV and HFA
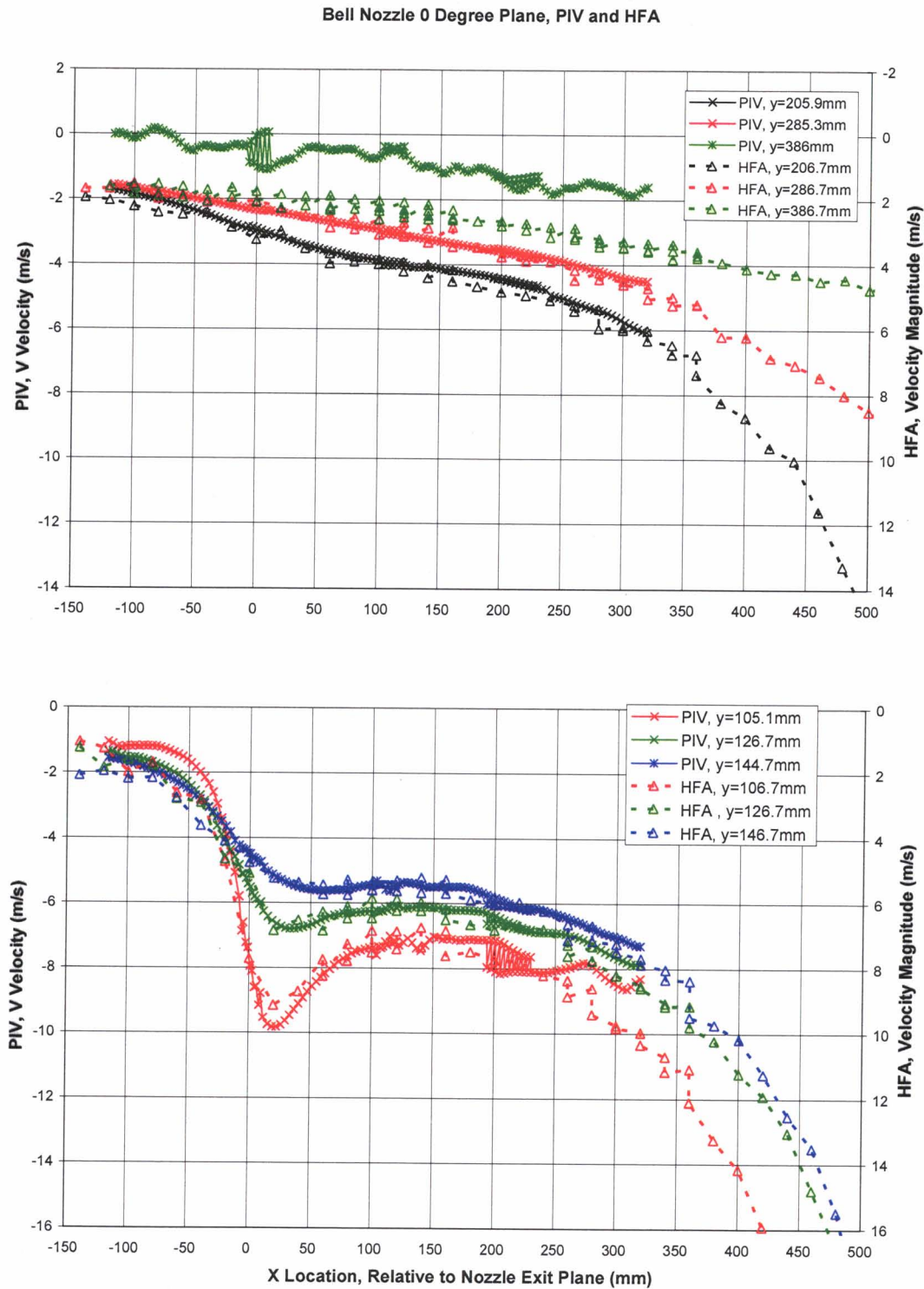
Figure 80. Comparison of HFA Velocity Magnitude to PIV V-Velocity in the Bell Nozzle 0° Plane.

Bell Nozzle 180 Degree Plane, PIV and HFA
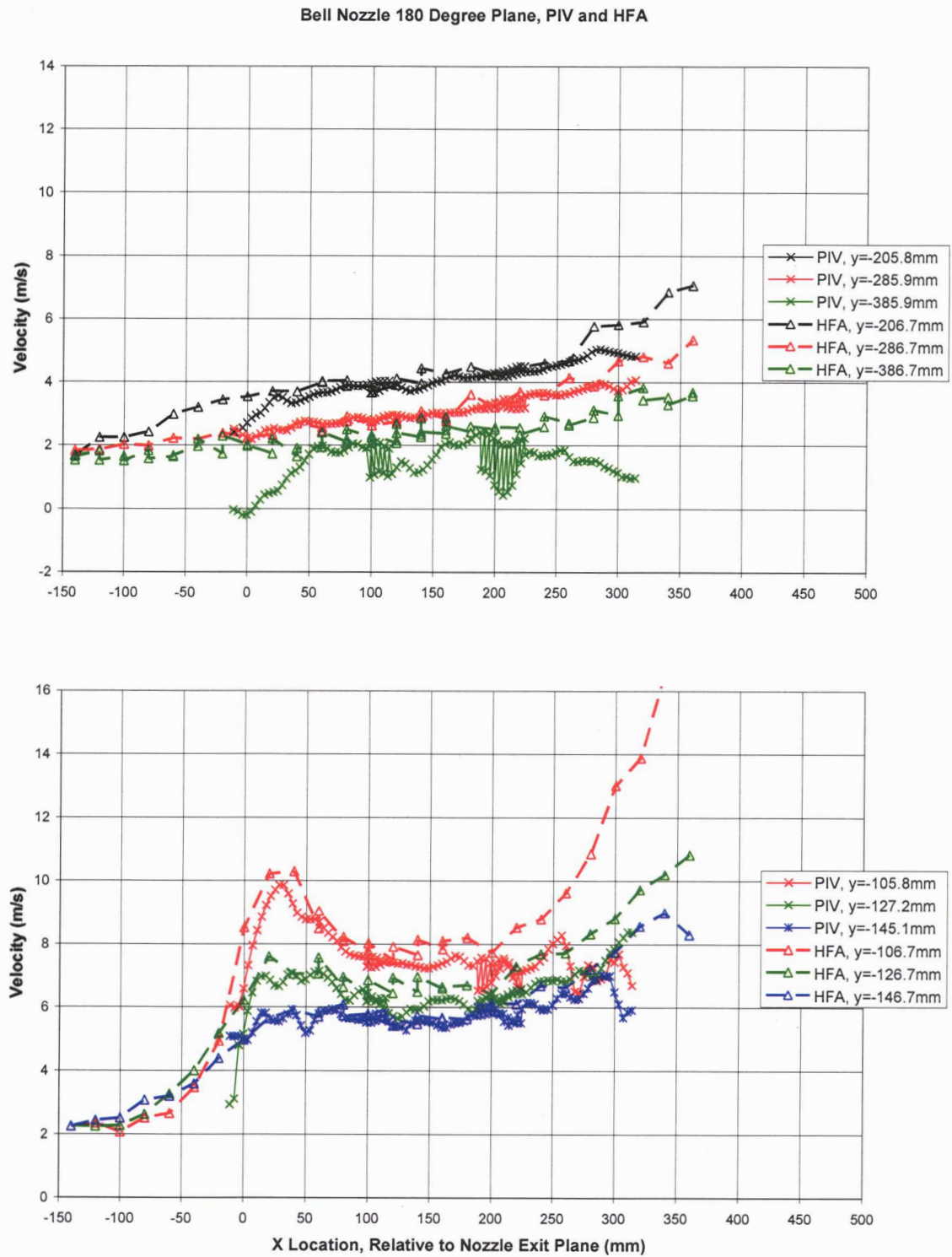
Figure 81. Comparison of HFA Velocity Magnitude to PIV V-Velocity in the Bell
Nozzle 180° Plane.

3.5.7. Entrained Flow Symmetry

The PIV data for both nozzles (the Stratford, Figure 38; the Bell, Figure 59) showed that the entrained flowfield in the 0° planes was fairly similar to that in the respective 180° planes. One of the objectives of the HFA data was to determine if the entrained flowfields in the 90° planes was similar to that of 0 and 180° planes. That is, were the entrained flowfield symmetric about the nozzles?

The HFA data showed that the character of the entrained flow in the 90° planes was similar to that in the 0 and 180° planes (Figure 72 and Figure 76). But as discussed in the section above, the HFA indicated velocity in the 90° planes was higher than that in the 0 and 180° planes. Both nozzles' 90° planes were measured with the HFA hardware that appeared to record velocity magnitudes higher than the true velocity (see Section 3.5.6). If in fact the 90° plane HFA data read high, and the real velocities were lower, the curves for the 90° planes (and the Stratford's 0° plane) in Figure 72 and Figure 76 would move downward toward the curves for the other three planes. This would likely result in entrained flow that was more symmetric than that implied by Figure 72 and Figure 76.

That said, the reader is reminded of the vortex at the inlet of the plume capture pipe in the 180° plane and the vortices attached to the west face of the test cabin (see Section 3.2). Both of which eliminate the possibility of truly axisymmetric entrained flowfields.

3.5.8. HFA Data Files

The electronic media associated with this report contains all HFA datasets and associated Excel files used to manipulate it. It also contains a few key TecPlot 'layout' files for plotting the data. The Bell and Stratford data structure and processing was very similar. The Bell nozzle files are described here. In these files the Stratford nozzle is at times referred to as the 'Sonic' nozzle. The HFA data for each nozzle is in its own folder.

All of the raw data for each window was processed with two calibration curves, one for lower velocities and one for higher velocities. The velocities resulting from the 'low' and 'high' calibrations are in neighboring columns in 'Bellnearfield.xls' (Stratnearfield.xls). Each widow's data is contained in a separate worksheet.

'BellHFAdata6.xls' (StratHFAdata2.xls) references Bellnearfield.xls and also has one worksheet for each window of data. In each worksheet a transition velocity (labeled 'filter') is specified which sets the value below/above which the low/high calibrations were used. Most users of the data should have no reason to modify this transition value. 'BellHFAdata6.xls' has worksheets (one per plane) that combine the data from all the windows in a plane. This worksheet is used to create the line plots presented in this report.

'BellHFAforTecPlot.xls' (StratHFAforTecPlot.xls) references the window data in BellHFAdata6.xls. BellHFAforTecPlot.xls combines, or weaves, the data into one continuous data field for each plane. These woven data worksheets were exported to

create the TecPlot '.dat' data files. The .dat data files are included in the electronic media.

4. CONCLUSIONS

The entrained flowfield velocities for the Bell and Stratford nozzles were captured with both particle image velocimetry (PIV) and hot film anemometry (HFA). The data acquired with the two different techniques exhibit excellent agreement in three of the four planes. For the one plane in which they did not agree as well, there is a reasonable explanation for the differences.

In this test configuration there were two phenomena inducing the entrained flow. The first was the plume expansion at the nozzle exit. The second was the plume capture pipe sink. The data clearly shows that the acceleration of the entrained flows near the nozzle exits was different between the nozzles. The data also clearly shows that for the majority of the area in which the entrained flowfields were measured, the entrained flows were quite similar for both nozzles. This similarity was due to the sink that existed in the plume capture pipe. This sink resulted from the interaction of the plumes and the plume capture pipe inner wall. The sink induced flow from all directions toward the plume capture pipe inlet.

The Stratford nozzle PIV data quality is acceptable. The PIV data acquisition techniques and test boundaries were being improved as the Stratford data was being acquired. Therefore, the Bell nozzle's PIV data is the better quality data of the two PIV data sets.

The PIV data indicated there was a region of unsteadiness in the entrained flow above the nozzle test articles. The source of the unsteady flow was not identified.

The PIV and HFA data indicate the entrained flowfields in the 0, 90 and 180° planes were fairly similar. That is, the flow was generally symmetric about the nozzles. However, there were at least two large sources of asymmetry; the vortices and streaks of entrained flow from the base upstream of the nozzles and the vortex attached to the floor, going into the bottom of the plume capture pipe.

Although the plume capture pipe sink had a significant effect on the entrained flowfield, the local effects of the nozzle flows could be discerned. Therefore, the data reported here should prove useful for benchmarking CFD codes for cold flow nozzle flow entrainment.

5.   RECOMMENDATIONS AND LESSONS LEARNED

In this section recommendations and lessons learned are presented in the general order that material was discussed in this report.

Recommendation for CFD analysis of the test configuration:
- The computational domain should be three dimensional. The entrained flow did contain three dimensional features.
- However, the entrained flow was sufficiently symmetric that an axisymmetric computational domain is a plausible first approximation of the flow.
- The plume capture pipe should be included in the computational domain. Attention should be paid to proper modeling of the plume capture pipe sink.

Lessons Learned, general:
- Parametric pretest CFD of the proposed test configurations was helpful in setting requirements for test configurations geometry and also for understanding the range of velocity magnitudes to be measured.
- Data acquisition computers and equipment should be shielded from the high acoustic energy the plumes create. The ~125 to 133dB vibrated disk drives enough to make the computers inoperative.
- The flow visualization with the fog, prior to obtaining any data, was very useful in understanding the large global flow features.
- The plume is not fully captured by the pipe at low nozzle inlet pressures. For these experiments, the plume was fully captured when nozzle inlet pressures was greater than ~5atm.

Lesson Learned related to the plume capture pipe sink effect on entrained flow:
- Running two different nozzle configurations was very helpful in understanding where the entrainment effects due to the nozzle exit effect were dominate and where plume capture pipe sink effect was dominate. If only one nozzle had been run, then it would have been difficult to delineate the two effects.

Recommendations related to the plume capture pipe sink effect on entrained flow:
   To reduce or eliminate the plume capture pipe sink effect:
- Remove the plume capture pipe entirely, or
- Remove more of it to increase distance between nozzle test article and pipe inlet, or
- Perforate the pipe, with 25 or 50mm holes, downstream of its inlet to reduce the sink's strength at the pipe inlet
   To more easily discern the effect of the plume capture pipe sink, obtain entrained flow velocities data:
- With different distances between the nozzle exit and plume capture pipe inlet.
- Without nozzles running, run the ejectors, currently in the pipe, at the same mass flow that the nozzles exhausted into the pipe.

Recommendations to better understand the effect of the Bell nozzle flow separation on entrained flow:
- Obtain entrained flow velocity data for the current Bell nozzle with significantly lower nozzle inlet pressure, ~10.4atm.
- Run a CFD analysis at the tested nozzle inlet pressure, then at a high enough nozzle inlet pressure to eliminate the nozzle flow separation.

Recommendation to eliminate Bell nozzle flow separation:
- Design a new test article with a lower area ratio.

Recommendation to better understand the different effects on flow entrainment of the Stratford and Bell nozzles:
- Run the Stratford at the same nozzle inlet pressure and/or mass flow as the Bell nozzle.

Lessons Learned relative to entrainment flow data:
- Acquiring both PIV and HFA data was useful. The PIV provided high density measurements. The HFA provided lower density measurement, but over a much larger area. This helped interpret the 'big picture' of the flow physics and helped in understanding the PIV data better.

Lessons Learned relative to the PIV data acquisition:
- Have the openings in the building far from the test article and measurement region. Openings near the measurement fields induced additional fluctuations in the entrained flow.
- Place the seeder far from the PIV measurement field so as to seed the entrained air as evenly as possible. For this test, the seeder by the garage door worked well.
- Perform all seeding parametrics and diagnostics at reduced nozzle inlet pressure to conserve facility air supply.
- Two scheduled data acquisition periods, with several days between them, enabled problems discovered in the first period to be fixed without wasting valuable PIV test time.
- Do not try to acquire the highest priority data in the first test runs. Use the first runs to understand the PIV system requirements for obtaining good data and to understand the structure of the nozzle flow.

Recommendations for future PIV data acquisition:
- The CCD camera used for PIV testing was a 2 Mega Pixel camera. Use of new generation, more sensitive with a higher number of active pixels, CCD cameras such as 4 or 11 Mega Pixel cameras would allow for the capture of a much larger field of view and negate the need for merging smaller FOV PIV data sets.
- The need to illuminate a large field of view would also require more powerful dual cavity YAG lasers than the 120mJ per pulse one used here.
- Use multiple PIV cameras side by side to double the effective field of view, and, therefore, data acquired.
- Shield the cameras and computers from the acoustic environment generated by the plumes.

- Use multiple seeders to ensure optimal seed particle uniformity and density.

Recommendations to improve the HFA data acquisition:
- Obtain and use a two component instrument so both U and V-velocity components could be captured at the same time.
- Have multiple probes on hand prior to starting the test. They break easily.
- Have probes calibrated prior to testing.
- Have real time feed back during calibration of HFA probes.

Lesson Learned relative to capturing flow visualization with the digital video camera and low power laser:
- Insufficient light energy was available if the camera was position to capture 'back scattered' light. That is, if the laser and camera were on the same side of the feature being illuminated with light scattered backward toward the camera. Sufficient light energy was available when the camera was positioned to capture 'forward scattered' light. That is, if the camera was on the other side of the feature being illuminated with light scattered forward toward the camera. More light is scattered forward than back.

6. REFERENCES

1. Sparkes, D.W. "A Standard Choked Nozzle for Absolute Calibration of Air Flowmeters", The Aeronautical Journal of the Royal Aeronautical Society, April, 1968. Pgs 335-338.
2. Dr. Khaled Hammad, Personal Communication, January, 2005.
3. FlowMap Particle Image Velocimetry Instrumentation, Vol. 1, Dantec Dynamics Inc., 1998.
4. Westergaard, Madsen, Marassi and Tomasini, "Accuracy of PIV Signals in Theory and Practice", 5th International Symposium on Particle Image Velocimetry, Busan, Korea, September, 2003, paper 3301
5. "Experimentation and Uncertainty Analysis for Engineers", Hugh W. Coleman & W. Glenn Steele, Jr., John Wiley & Sons Inc., 1989. 6.
6. Collis D C and Williams M J, Two-dimensional convection from heated wires at low Reynolds numbers, J. Fluid Mech. 6, 357–84, 1959.
7. Brunn, H, H., Nabhani, N., Fardad, A. A., and Al-Kayiem, H. H., Velocity component measurements by X hot-wire anemometry, Meas. Sci. Tech., 1, 1314-1321, 1990.

7.   APPENDICIES

Appendix 1. Nozzle Test Article Geometries and Bell Nozzle Wall Pressure Data.

The nozzle internal geometries are presented in Tables A1 and A2. The Stratford nozzle internal geometry is the as-designed contour for a throat of 35.56mm. The Bell nozzle internal geometry was extracted from an Initial Graphics Exchange Specification file, refined in a grid generator and printed out. Bell nozzle wall static pressure measurement locations are documented in Table A3.

3.5.7. Entrained Flow Symmetry

The PIV data for both nozzles (the Stratford, Figure 38; the Bell, Figure 59) showed that the entrained flowfield in the 0° planes was fairly similar to that in the respective 180° planes. One of the objectives of the HFA data was to determine if the entrained flowfields in the 90° planes was similar to that of 0 and 180° planes. That is, were the entrained flowfield symmetric about the nozzles?

The HFA data showed that the character of the entrained flow in the 90° planes was similar to that in the 0 and 180° planes (Figure 72 and Figure 76). But as discussed in the section above, the HFA indicated velocity in the 90° planes was higher than that in the 0 and 180° planes. Both nozzles' 90° planes were measured with the HFA hardware that appeared to record velocity magnitudes higher than the true velocity (see Section 3.5.6). If in fact the 90° plane HFA data read high, and the real velocities were lower, the curves for the 90° planes (and the Stratford's 0° plane) in Figure 72 and Figure 76 would move downward toward the curves for the other three planes. This would likely result in entrained flow that was more symmetric than that implied by Figure 72 and Figure 76.

That said, the reader is reminded of the vortex at the inlet of the plume capture pipe in the 180° plane and the vortices attached to the west face of the test cabin (see Section 3.2). Both of which eliminate the possibility of truly axisymmetric entrained flowfields.

3.5.8. HFA Data Files

The electronic media associated with this report contains all HFA datasets and associated Excel files used to manipulate it. It also contains a few key TecPlot 'layout' files for plotting the data. The Bell and Stratford data structure and processing was very similar. The Bell nozzle files are described here. In these files the Stratford nozzle is at times referred to as the 'Sonic' nozzle. The HFA data for each nozzle is in its own folder.

All of the raw data for each window was processed with two calibration curves, one for lower velocities and one for higher velocities. The velocities resulting from the 'low' and 'high' calibrations are in neighboring columns in 'Bellnearfield.xls' (Stratnearfield.xls). Each widow's data is contained in a separate worksheet.

'BellHFAdata6.xls' (StratHFAdata2.xls) references Bellnearfield.xls and also has one worksheet for each window of data. In each worksheet a transition velocity (labeled 'filter') is specified which sets the value below/above which the low/high calibrations were used. Most users of the data should have no reason to modify this transition value. 'BellHFAdata6.xls' has worksheets (one per plane) that combine the data from all the windows in a plane. This worksheet is used to create the line plots presented in this report.

'BellHFAforTecPlot.xls' (StratHFAforTecPlot.xls) references the window data in BellHFAdata6.xls. BellHFAforTecPlot.xls combines, or weaves, the data into one continuous data field for each plane. These woven data worksheets were exported to

create the TecPlot '.dat' data files. The .dat data files are included in the electronic media.

4.   CONCLUSIONS

The entrained flowfield velocities for the Bell and Stratford nozzles were captured with both particle image velocimetry (PIV) and hot film anemometry (HFA). The data acquired with the two different techniques exhibit excellent agreement in three of the four planes. For the one plane in which they did not agree as well, there is a reasonable explanation for the differences.

In this test configuration there were two phenomena inducing the entrained flow. The first was the plume expansion at the nozzle exit. The second was the plume capture pipe sink. The data clearly shows that the acceleration of the entrained flows near the nozzle exits was different between the nozzles. The data also clearly shows that for the majority of the area in which the entrained flowfields were measured, the entrained flows were quite similar for both nozzles. This similarity was due to the sink that existed in the plume capture pipe. This sink resulted from the interaction of the plumes and the plume capture pipe inner wall. The sink induced flow from all directions toward the plume capture pipe inlet.

The Stratford nozzle PIV data quality is acceptable. The PIV data acquisition techniques and test boundaries were being improved as the Stratford data was being acquired. Therefore, the Bell nozzle's PIV data is the better quality data of the two PIV data sets.

The PIV data indicated there was a region of unsteadiness in the entrained flow above the nozzle test articles. The source of the unsteady flow was not identified.

The PIV and HFA data indicate the entrained flowfields in the 0, 90 and 180° planes were fairly similar. That is, the flow was generally symmetric about the nozzles. However, there were at least two large sources of asymmetry; the vortices and streaks of entrained flow from the base upstream of the nozzles and the vortex attached to the floor, going into the bottom of the plume capture pipe.

Although the plume capture pipe sink had a significant effect on the entrained flowfield, the local effects of the nozzle flows could be discerned. Therefore, the data reported here should prove useful for benchmarking CFD codes for cold flow nozzle flow entrainment.

5.   RECOMMENDATIONS AND LESSONS LEARNED

In this section recommendations and lessons learned are presented in the general order that material was discussed in this report.

Recommendation for CFD analysis of the test configuration:
- The computational domain should be three dimensional. The entrained flow did contain three dimensional features.
- However, the entrained flow was sufficiently symmetric that an axisymmetric computational domain is a plausible first approximation of the flow.
- The plume capture pipe should be included in the computational domain. Attention should be paid to proper modeling of the plume capture pipe sink.

Lessons Learned, general:
- Parametric pretest CFD of the proposed test configurations was helpful in setting requirements for test configurations geometry and also for understanding the range of velocity magnitudes to be measured.
- Data acquisition computers and equipment should be shielded from the high acoustic energy the plumes create. The ~125 to 133dB vibrated disk drives enough to make the computers inoperative.
- The flow visualization with the fog, prior to obtaining any data, was very useful in understanding the large global flow features.
- The plume is not fully captured by the pipe at low nozzle inlet pressures. For these experiments, the plume was fully captured when nozzle inlet pressures was greater than ~5atm.

Lesson Learned related to the plume capture pipe sink effect on entrained flow:
- Running two different nozzle configurations was very helpful in understanding where the entrainment effects due to the nozzle exit effect were dominate and where plume capture pipe sink effect was dominate. If only one nozzle had been run, then it would have been difficult to delineate the two effects.

Recommendations related to the plume capture pipe sink effect on entrained flow:
To reduce or eliminate the plume capture pipe sink effect:
- Remove the plume capture pipe entirely, or
- Remove more of it to increase distance between nozzle test article and pipe inlet, or
- Perforate the pipe, with 25 or 50mm holes, downstream of its inlet to reduce the sink's strength at the pipe inlet

To more easily discern the effect of the plume capture pipe sink, obtain entrained flow velocities data:
- With different distances between the nozzle exit and plume capture pipe inlet.
- Without nozzles running, run the ejectors, currently in the pipe, at the same mass flow that the nozzles exhausted into the pipe.

Recommendations to better understand the effect of the Bell nozzle flow separation on entrained flow:

- Obtain entrained flow velocity data for the current Bell nozzle with significantly lower nozzle inlet pressure, ~10.4atm.
- Run a CFD analysis at the tested nozzle inlet pressure, then at a high enough nozzle inlet pressure to eliminate the nozzle flow separation.

Recommendation to eliminate Bell nozzle flow separation:

- Design a new test article with a lower area ratio.

Recommendation to better understand the different effects on flow entrainment of the Stratford and Bell nozzles:

- Run the Stratford at the same nozzle inlet pressure and/or mass flow as the Bell nozzle.

Lessons Learned relative to entrainment flow data:

- Acquiring both PIV and HFA data was useful. The PIV provided high density measurements. The HFA provided lower density measurement, but over a much larger area. This helped interpret the 'big picture' of the flow physics and helped in understanding the PIV data better.

Lessons Learned relative to the PIV data acquisition:

- Have the openings in the building far from the test article and measurement region. Openings near the measurement fields induced additional fluctuations in the entrained flow.
- Place the seeder far from the PIV measurement field so as to seed the entrained air as evenly as possible. For this test, the seeder by the garage door worked well.
- Perform all seeding parametrics and diagnostics at reduced nozzle inlet pressure to conserve facility air supply.
- Two scheduled data acquisition periods, with several days between them, enabled problems discovered in the first period to be fixed without wasting valuable PIV test time.
- Do not try to acquire the highest priority data in the first test runs. Use the first runs to understand the PIV system requirements for obtaining good data and to understand the structure of the nozzle flow.

Recommendations for future PIV data acquisition:

- The CCD camera used for PIV testing was a 2 Mega Pixel camera. Use of new generation, more sensitive with a higher number of active pixels, CCD cameras such as 4 or 11 Mega Pixel cameras would allow for the capture of a much larger field of view and negate the need for merging smaller FOV PIV data sets.
- The need to illuminate a large field of view would also require more powerful dual cavity YAG lasers than the 120mJ per pulse one used here.
- Use multiple PIV cameras side by side to double the effective field of view, and, therefore, data acquired.
- Shield the cameras and computers from the acoustic environment generated by the plumes.

- Use multiple seeders to ensure optimal seed particle uniformity and density.

Recommendations to improve the HFA data acquisition:
- Obtain and use a two component instrument so both U and V-velocity components could be captured at the same time.
- Have multiple probes on hand prior to starting the test. They break easily.
- Have probes calibrated prior to testing.
- Have real time feed back during calibration of HFA probes.

Lesson Learned relative to capturing flow visualization with the digital video camera and low power laser:
- Insufficient light energy was available if the camera was position to capture 'back scattered' light. That is, if the laser and camera were on the same side of the feature being illuminated with light scattered backward toward the camera. Sufficient light energy was available when the camera was positioned to capture 'forward scattered' light. That is, if the camera was on the other side of the feature being illuminated with light scattered forward toward the camera. More light is scattered forward than back.

6. REFERENCES

1. Sparkes, D.W. "A Standard Choked Nozzle for Absolute Calibration of Air Flowmeters", The Aeronautical Journal of the Royal Aeronautical Society, April, 1968. Pgs 335-338.
2. Dr. Khaled Hammad, Personal Communication, January, 2005.
3. FlowMap Particle Image Velocimetry Instrumentation, Vol. 1, Dantec Dynamics Inc., 1998.
4. Westergaard, Madsen, Marassi and Tomasini, "Accuracy of PIV Signals in Theory and Practice", 5th International Symposium on Particle Image Velocimetry, Busan, Korea, September, 2003, paper 3301
5. "Experimentation and Uncertainty Analysis for Engineers", Hugh W. Coleman & W. Glenn Steele, Jr., John Wiley & Sons Inc., 1989. 6.
6. Collis D C and Williams M J, Two-dimensional convection from heated wires at low Reynolds numbers, J. Fluid Mech. 6, 357–84, 1959.
7. Brunn, H, H., Nabhani, N., Fardad, A. A., and Al-Kayiem, H. H., Velocity component measurements by X hot-wire anemometry, Meas. Sci. Tech., 1, 1314-1321, 1990.

7.   APPENDICIES

Appendix 1. Nozzle Test Article Geometries and Bell Nozzle Wall Pressure Data.

The nozzle internal geometries are presented in Tables A1 and A2. The Stratford nozzle internal geometry is the as-designed contour for a throat of 35.56mm. The Bell nozzle internal geometry was extracted from an Initial Graphics Exchange Specification file, refined in a grid generator and printed out. Bell nozzle wall static pressure measurement locations are documented in Table A3.

Table A1. Stratford Nozzle Internal, As-Designed, Wall Geometry.

Section	X (mm) Relative to the Nozzle Throat	X (mm) Stratford Global Coordinates	Y (mm) Stratford Global Coordinates
Upstream Measurement Section	-221.1832	-232.8638	53.3400
	-167.8432	-179.5238	53.3400
Profiled Contraction	-167.8432	-179.5238	53.3400
	-166.2074	-177.8881	53.3399
	-164.5717	-176.2523	53.3395
	-162.9359	-174.6166	53.3384
	-161.3002	-172.9808	53.3361
	-159.6644	-171.3450	53.3324
	-158.0286	-169.7093	53.3269
	-156.3929	-168.0735	53.3192
	-154.7571	-166.4378	53.3089
	-153.1214	-164.8020	53.2957
	-151.4856	-163.1662	53.2793
	-149.8498	-161.5305	53.2592
	-148.2141	-159.8947	53.2351
	-146.5783	-158.2590	53.2066
	-144.9426	-156.6232	53.1734
	-143.3068	-154.9874	53.1351
	-141.6710	-153.3517	53.0913
	-140.0353	-151.7159	53.0417
	-138.3995	-150.0802	52.9859
	-136.7638	-148.4444	52.9235
	-135.1280	-146.8086	52.8542
	-133.4922	-145.1729	52.7776
	-131.8565	-143.5371	52.6934
	-130.2207	-141.9014	52.6012
	-128.5850	-140.2656	52.5006
	-126.9492	-138.6298	52.3912
	-125.3134	-136.9941	52.2727
	-123.6777	-135.3583	52.1448
	-122.0419	-133.7226	52.0070
	-120.4062	-132.0868	51.8590
	-118.7704	-130.4510	51.7005
	-117.1346	-128.8153	51.5310
	-115.4989	-127.1795	51.3502
	-113.8631	-125.5438	51.1578
	-112.2274	-123.9080	50.9533
	-110.5916	-122.2722	50.7365
	-108.9558	-120.6365	50.5069
	-107.3201	-119.0007	50.2641
	-105.6843	-117.3650	50.0080
	-104.0486	-115.7292	49.7379
	-102.4128	-114.0934	49.4537
	-100.7770	-112.4577	49.1548
	-99.1413	-110.8219	48.8411
	-97.5055	-109.1862	48.5120
	-95.8698	-107.5504	48.1673
	-94.2340	-105.9146	47.8065
	-92.5982	-104.2789	47.4294
	-90.9625	-102.6431	47.0355
	-89.3267	-101.0074	46.6244
	-87.6910	-99.3716	46.1959
	-86.0552	-97.7358	45.7495
	-84.4194	-96.1001	45.2849
	-82.7837	-94.4643	44.8017
	-81.1479	-92.8286	44.2996
	-79.5122	-91.1928	43.7782
	-77.8764	-89.5570	43.2370
	-76.2406	-87.9213	42.6759
	-74.6049	-86.2855	42.0943
	-72.9691	-84.6498	41.4920
	-71.3334	-83.0140	40.8686
	-69.6976	-81.3782	40.2236
Conical Section	-69.6976	-81.3782	40.2236
	-26.4133	-38.0939	22.8667

Section	X (mm) Relative to the Nozzle Throat	X (mm) Stratford Global Coordinates	Y (mm) Stratford Global Coordinates
Nozzle Convergent Section	-26.4133	-38.0939	22.8667
	-26.1028	-37.7834	22.7434
	-25.7917	-37.4724	22.6215
	-25.4801	-37.1607	22.5011
	-25.1679	-36.8486	22.3821
	-24.8552	-36.5358	22.2646
	-24.5419	-36.2225	22.1486
	-24.2280	-35.9087	22.0340
	-23.9136	-35.5943	21.9210
	-23.5987	-35.2794	21.8094
	-23.2833	-34.9640	21.6992
	-22.9674	-34.6480	21.5906
	-22.6509	-34.3316	21.4835
	-22.3340	-34.0146	21.3778
	-22.0165	-33.6972	21.2736
	-21.6986	-33.3793	21.1709
	-21.3802	-33.0609	21.0698
	-21.0613	-32.7420	20.9701
	-20.7420	-32.4226	20.8719
	-20.4222	-32.1028	20.7752
	-20.1020	-31.7826	20.6800
	-19.7813	-31.4619	20.5863
	-19.4601	-31.1408	20.4942
	-19.1386	-30.8192	20.4035
	-18.8166	-30.4972	20.3144
	-18.4942	-30.1749	20.2267
	-18.1714	-29.8520	20.1406
	-17.8482	-29.5288	20.0560
	-17.5246	-29.2052	19.9729
	-17.2006	-28.8813	19.8914
	-16.8763	-28.5569	19.8113
	-16.5515	-28.2322	19.7328
	-16.2264	-27.9071	19.6558
	-15.9010	-27.5816	19.5803
	-15.5751	-27.2558	19.5064
	-15.2490	-26.9296	19.4340
	-14.9225	-26.6031	19.3632
	-14.5957	-26.2763	19.2938
	-14.2685	-25.9492	19.2260
	-13.9411	-25.6217	19.1598
	-13.6133	-25.2940	19.0950
	-13.2853	-24.9659	19.0319
	-12.9569	-24.6375	18.9702
	-12.6282	-24.3089	18.9101
	-12.2993	-23.9800	18.8516
	-11.9701	-23.6508	18.7946
	-11.6407	-23.3213	18.7391
	-11.3110	-22.9916	18.6852
	-10.9810	-22.6616	18.6329
	-10.6508	-22.3314	18.5820
	-10.3203	-22.0010	18.5328
	-9.9897	-21.6703	18.4851
	-9.6588	-21.3394	18.4389
	-9.3277	-21.0083	18.3943
	-8.9964	-20.6770	18.3513
	-8.6649	-20.3455	18.3098
	-8.3332	-20.0138	18.2699
	-8.0013	-19.6819	18.2315
	-7.6692	-19.3499	18.1947
	-7.3370	-19.0176	18.1595
	-7.0046	-18.6852	18.1258
	-6.6721	-18.3527	18.0937
	-6.3394	-18.0200	18.0631
	-6.0065	-17.6872	18.0341
	-5.6736	-17.3542	18.0067
	-5.3405	-17.0211	17.9808
	-5.0073	-16.6879	17.9565
	-4.6739	-16.3546	17.9337
	-4.3405	-16.0212	17.9126
	-4.0070	-15.6876	17.8930
	-3.6734	-15.3540	17.8749
	-3.3397	-15.0204	17.8585
	-3.0059	-14.6866	17.8436
	-2.6721	-14.3528	17.8302
	-2.3382	-14.0189	17.8184
	-2.0043	-13.6849	17.8082
	-1.6703	-13.3510	17.7996
	-1.3363	-13.0169	17.7926
	-1.0022	-12.6829	17.7871
	-0.6682	-12.3488	17.7831
	-0.3341	-12.0147	17.7808
Nozzle Throat	0.0000	-11.6806	17.7800

Section	X (mm) Relative to the Nozzle Throat	X (mm) Stratford Global Coordinates	Y (mm) Stratford Global Coordinates
Nozzle Divergent Section	0.0000	-11.6806	17.7800
	0.1289	-11.5517	17.7801
	0.2579	-11.4228	17.7805
	0.3868	-11.2938	17.7811
	0.5158	-11.1649	17.7819
	0.6447	-11.0359	17.7829
	0.7736	-10.9070	17.7842
	0.9026	-10.7781	17.7857
	1.0315	-10.6491	17.7875
	1.1604	-10.5202	17.7895
	1.2894	-10.3913	17.7917
	1.4183	-10.2624	17.7941
	1.5472	-10.1334	17.7968
	1.6761	-10.0045	17.7998
	1.8050	-9.8756	17.8029
	1.9339	-9.7467	17.8063
	2.0628	-9.6178	17.8099
	2.1917	-9.4890	17.8138
	2.3206	-9.3601	17.8179
	2.4494	-9.2312	17.8222
	2.5783	-9.1023	17.8268
	2.7071	-8.9735	17.8315
	2.8360	-8.8447	17.8366
	2.9648	-8.7158	17.8418
	3.0937	-8.5870	17.8473
	3.2225	-8.4582	17.8530
	3.3513	-8.3294	17.8590
	3.4801	-8.2006	17.8652
	3.6089	-8.0718	17.8716
	3.7376	-7.9430	17.8783
	3.8664	-7.8143	17.8852
	3.9951	-7.6855	17.8923
	4.1239	-7.5568	17.8997
	4.2526	-7.4281	17.9073
	4.3813	-7.2994	17.9151
	4.5100	-7.1707	17.9231
	4.6386	-7.0420	17.9314
	4.7673	-6.9133	17.9400
	4.8960	-6.7847	17.9487
	5.0246	-6.6561	17.9577
	5.1532	-6.5274	17.9669
	5.2818	-6.3989	17.9764
	5.4104	-6.2703	17.9861
	5.5389	-6.1417	17.9960
	5.6675	-6.0132	18.0062
	5.7960	-5.8846	18.0166
	5.9245	-5.7561	18.0272
	6.0530	-5.6277	18.0381
	6.1814	-5.4992	18.0491
	6.3099	-5.3707	18.0605
	6.4383	-5.2423	18.0720
	6.5667	-5.1139	18.0838
	6.6951	-4.9855	18.0958
	6.8235	-4.8572	18.1081
	6.9518	-4.7288	18.1206
	7.0801	-4.6005	18.1333
	7.2084	-4.4722	18.1462
	7.3367	-4.3440	18.1594
	7.4649	-4.2157	18.1729
	7.5931	-4.0875	18.1865
	7.7213	-3.9593	18.2004
	7.8495	-3.8312	18.2145
	7.9776	-3.7030	18.2288
	8.1057	-3.5749	18.2434
	8.2338	-3.4468	18.2582
	8.3619	-3.3187	18.2733
	8.4899	-3.1907	18.2886
	8.6179	-3.0627	18.3041
	8.7459	-2.9347	18.3198
	8.8739	-2.8068	18.3358
	9.0018	-2.6789	18.3520
	9.1297	-2.5510	18.3684
	9.2575	-2.4231	18.3851
	9.3854	-2.2953	18.4020
	9.5132	-2.1675	18.4191
	9.6409	-2.0397	18.4365
	9.7687	-1.9120	18.4541
	9.8964	-1.7843	18.4719
	10.0241	-1.6566	18.4900
	10.1517	-1.5289	18.5083
	10.2793	-1.4013	18.5268
	10.4069	-1.2738	18.5455
	10.5344	-1.1462	18.5645
	10.6619	-1.0187	18.5837
	10.7894	-0.8913	18.6032
	10.9168	-0.7638	18.6229
	11.0442	-0.6364	18.6428
	11.1716	-0.5091	18.6629
	11.2989	-0.3817	18.6833
	11.4262	-0.2545	18.7039
	11.5534	-0.1272	18.7247
Nozzle Exit	11.6806	0.0000	18.7458

Table A2. Bell Nozzle Internal, As-Designed, Wall Geometry.

	X (mm) Relative to the Nozzle Throat	X (mm) Bell Global Coordinates	Y (mm) Bell Global Coordinates
Subsonic	-53.881528	-199.857284	33.966913
	-53.314357	-199.290113	33.966877
	-52.747186	-198.722942	33.966874
	-52.180009	-198.155765	33.966898
	-51.612838	-197.588593	33.966925
	-51.045667	-197.021422	33.966949
	-50.478496	-196.454251	33.966949
	-49.911322	-195.887077	33.966916
	-49.344151	-195.319906	33.966843
	-48.776977	-194.752732	33.966789
	-48.209806	-194.185561	33.966822
	-47.642635	-193.618390	33.967016
	-47.075461	-193.051216	33.967288
	-46.508289	-192.484045	33.967367
	-45.941118	-191.916874	33.966983
	-45.373944	-191.349700	33.966020
	-44.806773	-190.782529	33.965220
	-44.239599	-190.215355	33.965617
	-43.672431	-189.648187	33.968200
	-43.105272	-189.081028	33.972194
	-42.538104	-188.513860	33.974422
	-41.970939	-187.946695	33.971540
	-41.403759	-187.379515	33.960524
	-40.836930	-186.812686	33.940422
	-40.270495	-186.246250	33.911063
	-39.704481	-185.680236	33.872263
	-39.139299	-185.115054	33.823959
	-38.575074	-184.550829	33.766198
	-38.011806	-183.987561	33.699033
	-37.449755	-183.425511	33.622533
	-36.889097	-182.864853	33.536737
	-36.329941	-182.305696	33.441651
	-35.772393	-181.748148	33.337285
	-35.216622	-181.192377	33.223656
	-34.662913	-180.638668	33.100805
	-34.111272	-180.087027	32.968715
	-33.561796	-179.537551	32.827393
	-33.014888	-178.990643	32.676975
	-32.470577	-178.446333	32.517555
	-31.928841	-177.904596	32.349197
	-31.390026	-177.365782	32.172043
	-30.854188	-176.829944	31.985917
	-30.321684	-176.297439	31.790662
	-29.792595	-175.768350	31.586035
	-29.267176	-175.242931	31.372183
	-28.745344	-174.721100	31.149970
	-28.226729	-174.202485	30.920266
	-27.711014	-173.686770	30.683965
	-27.197825	-173.173581	30.442455
	-26.686198	-172.661954	30.197660
	-26.175189	-172.150944	29.951566
	-25.663874	-171.639629	29.706123
	-25.151870	-171.127634	29.462104
	-24.639445	-170.615201	29.219007
	-24.126846	-170.102602	28.976259
	-23.614341	-169.590097	28.733312
	-23.102015	-169.077770	28.489988
	-22.589796	-168.565551	28.246438
	-22.077612	-168.053367	28.002818
	-21.565391	-167.541147	27.759270
	-21.053121	-167.028876	27.515829
	-20.540823	-166.516579	27.272445
	-20.028521	-166.004277	27.029073
	-19.516232	-165.491988	26.785671
	-19.003962	-164.979718	26.542233
	-18.491699	-164.467455	26.298773
	-17.979439	-163.955195	26.055311
	-17.467174	-163.442929	25.811860
	-16.954899	-162.930654	25.568431
	-16.442612	-162.418367	25.325024
	-15.930311	-161.906066	25.081646
	-15.418000	-161.393755	24.838293
	-14.905697	-160.881453	24.594917
	-14.393436	-160.369192	24.351458
	-13.881241	-159.856997	24.107858
	-13.369115	-159.344870	23.864115
	-12.856958	-158.832714	23.620435
	-12.344657	-158.320413	23.377058
	-11.832095	-157.807850	23.134233
	-11.319295	-157.295050	22.891909
	-10.806633	-156.782388	22.649294
	-10.294540	-156.270296	22.405479
	-9.783442	-155.759198	22.159570
	-9.273001	-155.248756	21.912244
	-8.761475	-154.737231	21.667217
	-8.246958	-154.222713	21.428537
	-7.727457	-153.703213	21.200188
	-7.202447	-153.178202	20.985058
	-6.672078	-152.647833	20.784078
	-6.136102	-152.111858	20.597902
	-5.594933	-151.570688	20.427404
	-5.048906	-151.024662	20.273027
	-4.498772	-150.474527	20.135052
	-3.944507	-149.920263	20.013574
	-3.387042	-149.362797	19.908726
	-2.826843	-148.802598	19.819716
	-2.264525	-148.240281	19.745546
	-1.700236	-147.675992	19.685223
	-1.134533	-147.110289	19.640441
	-0.567871	-146.543626	19.616297
Throat	0.000000	-145.975756	19.618155

	X (mm) Relative to the Nozzle Throat	X (mm) Bell Global Coordinates	Y (mm) Bell Global Coordinates
Supersonic	0.000000	-145.975756	19.618155
	0.483117	-145.492638	19.644014
	0.964135	-145.011621	19.693605
	1.442383	-144.533372	19.767593
	1.915714	-144.060041	19.866497
	2.383110	-143.592645	19.990925
	2.843617	-143.132138	20.139284
	3.296772	-142.678984	20.308125
	3.743268	-142.232488	20.494328
	4.183381	-141.792374	20.694664
	4.618248	-141.357510	20.906129
	5.049255	-140.926500	21.125374
	5.477978	-140.497778	21.349030
	5.906129	-140.069626	21.573786
	6.335355	-139.640400	21.796498
	6.766083	-139.209672	22.016271
	7.197872	-138.777883	22.233946
	7.630273	-138.345482	22.450409
	8.062838	-137.912917	22.666547
	8.495204	-137.480551	22.883074
	8.927395	-137.048361	23.099948
	9.359530	-136.616225	23.316933
	9.791732	-136.184023	23.533786
	10.224120	-135.751635	23.750269
	10.656756	-135.319000	23.966256
	11.089613	-134.886142	24.181797
	11.522665	-134.453091	24.396948
	11.955878	-134.019877	24.611774
	12.389227	-133.586529	24.826327
	12.822706	-133.153049	25.040612
	13.256328	-132.719427	25.254613
	13.690098	-132.285657	25.468313
	14.124027	-131.851728	25.681687
	14.558123	-131.417632	25.894725
	14.992382	-130.983373	26.107427
	15.426806	-130.548949	26.319793
	15.861394	-130.114361	26.531826
	16.296142	-129.679613	26.743529
	16.731052	-129.244703	26.954895
	17.166128	-128.809628	27.165923
	17.601374	-128.374382	27.376602
	18.036791	-127.938964	27.586924
	18.472384	-127.503371	27.796883
	18.908145	-127.067610	28.006491
	19.344068	-126.631687	28.215762
	19.780147	-126.195608	28.424709
	20.216376	-125.759380	28.633345
	20.652759	-125.322996	28.841656
	21.089327	-124.886428	29.049580
	21.526110	-124.449645	29.257050
	21.963141	-124.012614	29.463999
	22.400437	-123.575318	29.670388
	22.837830	-123.137825	29.876356
	23.275513	-122.700243	30.082136
	23.713074	-122.262682	30.287962
	24.150506	-121.825249	30.494063
	24.587851	-121.387905	30.700361
	25.025476	-120.950280	30.906056
	25.463789	-120.511966	31.110271
	25.903206	-120.072549	31.312118
	26.344068	-119.631688	31.510804
	26.786032	-119.189724	31.706998
	27.228295	-118.747460	31.902519
	27.670035	-118.305721	32.099216
	28.110430	-117.865326	32.298928
	28.548927	-117.426829	32.502761
	28.986124	-116.989631	32.709362
	29.422892	-116.552863	32.916871
	29.860102	-116.115653	33.123438
	30.298599	-115.677157	33.327266
	30.738567	-115.237188	33.527901
	31.179583	-114.796172	33.726215
	31.621223	-114.354533	33.923138
	32.063062	-113.912693	34.119611
	32.504778	-113.470978	34.316365
	32.946396	-113.029359	34.513354
	33.388033	-112.587723	34.710260
	33.829800	-112.145956	34.906896
	34.271806	-111.703950	35.102993
	34.714094	-111.261662	35.298451
	35.156639	-110.819117	35.493334
	35.599411	-110.376345	35.687609
	36.042377	-109.933379	35.881616
	36.485518	-109.490237	36.075136
	36.928832	-109.046923	36.268256
	37.372331	-108.603424	36.460953
	37.816021	-108.159735	36.653210
	38.259910	-107.715845	36.845011
	38.704000	-107.271756	37.036342
	39.148292	-106.827464	37.227206
	39.592781	-106.382975	37.417605
	40.037470	-105.938286	37.607546
	40.482358	-105.493397	37.797024
	40.927441	-105.048315	37.986041
	41.372717	-104.603039	38.174596
	41.818193	-104.157563	38.362681
	42.263866	-103.711890	38.550293
	42.709736	-103.266020	38.737437
	43.155808	-102.819947	38.924105
	43.602081	-102.373675	39.110297
	44.048553	-101.927203	39.296009
	44.866490	-101.109266	39.634766
	45.685084	-100.290672	39.971912
	46.504344	-99.471411	40.307436
	47.324273	-98.651482	40.641327
	48.144875	-97.830880	40.973574
	48.966152	-97.009604	41.304171
	49.788092	-96.187664	41.633096
	50.610692	-95.365064	41.960351
	51.433955	-94.541801	42.285921
	52.257887	-93.717868	42.609808

	X (mm) Relative to the Nozzle Throat	X (mm) Bell Global Coordinates	Y (mm) Bell Global Coordinates
	53.082491	-92.893264	42.932003
	53.907762	-92.067993	43.252499
	54.733693	-91.242063	43.571278
	55.560271	-90.415484	43.888340
	56.387510	-89.588245	44.203673
	57.215415	-88.760340	44.517277
	58.043974	-87.931781	44.829140
	58.873187	-87.102569	45.139257
	59.703048	-86.272708	45.447635
	60.533551	-85.442205	45.754281
	61.364696	-84.611060	46.059165
	62.196519	-83.779237	46.362223
	63.028996	-82.946760	46.663464
	63.862060	-82.113695	46.963073
	64.695663	-81.280092	47.261181
	65.529975	-80.445780	47.557302
	66.365244	-79.610511	47.850716
	67.201197	-78.774558	48.142168
	68.036896	-77.938859	48.434344
	68.871886	-77.103869	48.728548
	69.707682	-76.268074	49.020460
	70.546057	-75.429698	49.304903
	71.386558	-74.589197	49.582966
	72.227338	-73.748418	49.860189
	73.067409	-72.908347	50.139563
	73.907480	-72.068275	50.418916
	74.748357	-71.227399	50.695855
	75.590057	-70.385699	50.970260
	76.432350	-69.543405	51.242851
	77.275134	-68.700621	51.513922
	78.118463	-67.857292	51.783298
	78.962374	-67.013382	52.050844
	79.806853	-66.168902	52.316586
	80.651878	-65.323877	52.580584
	81.497448	-64.478308	52.842838
	82.343557	-63.632199	53.103342
	83.190204	-62.785551	53.362095
	84.037379	-61.938377	53.619111
	84.885074	-61.090681	53.874407
	85.733284	-60.242471	54.127982
	86.582015	-59.393740	54.379832
	87.431243	-58.544513	54.629969
	88.280979	-57.694777	54.878403
	89.131218	-56.844538	55.125160
	89.981929	-55.993827	55.370227
	90.833112	-55.142643	55.613629
	91.684774	-54.290981	55.855378
	92.536903	-53.438853	56.095474
	93.389497	-52.586258	56.333928
	94.242546	-51.733210	56.570760
	95.096030	-50.879725	56.805974
	95.949957	-50.025798	57.039590
	96.804308	-49.171448	57.271637
	97.659083	-48.316673	57.502116
	98.514281	-47.461474	57.731033
	99.369891	-46.605864	57.958399
	100.225901	-45.749854	58.184245
	101.082311	-44.893444	58.408584
	101.939114	-44.036641	58.631432
	102.796293	-43.179462	58.852797
	103.653848	-42.321908	59.072696
	104.511777	-41.463978	59.291179
	105.370046	-40.605709	59.508250
	106.228690	-39.747065	59.723922
	107.087662	-38.888094	59.938202
	107.946984	-38.028771	60.151113
	108.806634	-37.169122	60.362685
	109.666610	-36.309145	60.572950
	110.526902	-35.448854	60.781925
	111.387496	-34.588259	60.989634
	112.248393	-33.727362	61.196083
	113.109581	-32.866175	61.401303
	113.971059	-32.004696	61.605318
	114.832804	-31.142951	61.808158
	115.694828	-30.280928	62.009841
	116.557118	-29.418638	62.210398
	117.419662	-28.556094	62.409859
	118.282448	-27.693307	62.608255
	119.145477	-26.830278	62.805614
	120.008736	-25.967020	63.001956
	120.872213	-25.103543	63.197293
	121.735920	-24.239836	63.391667
	122.599833	-23.375923	63.585109
	123.463939	-22.511816	63.777654
	124.328252	-21.647504	63.969321
	125.192746	-20.783010	64.160152
	126.057410	-19.918346	64.350172
	126.922255	-19.053500	64.539423
	127.787258	-18.184497	64.727935
	128.652406	-17.323349	64.915726
	129.517712	-16.458043	65.102833
	130.383163	-15.592592	65.289298
	131.248735	-14.727020	65.475158
	132.114429	-13.861327	65.660448
	132.980243	-12.995512	65.845194
	133.846166	-12.129589	66.029424
	134.712187	-11.263569	66.213182
	135.578304	-10.397452	66.396510
	136.444494	-9.531262	66.579463
	137.310768	-8.664987	66.762065
	138.177092	-7.798664	66.944357
	139.043487	-6.932268	67.126353
	139.909944	-6.065812	67.308107
	140.776424	-5.199331	67.489655
	141.642953	-4.332802	67.671045
	142.509494	-3.466261	67.852314
	143.376060	-2.599696	68.033505
	144.242625	-1.733131	68.214665
	145.109202	-0.866553	68.395831
Nozzle Exit	145.975756	0.000000	68.577052

Table A3. Bell Nozzle Wall Static Pressure Measurement Locations

Wall Pstatic Measurement Label	X(in) Relative to Nozzle Throat	X(mm) Relative to Nozzle Throat	X(mm) Relative to Global Coordinate System
PS2-SR-1	0.2931	7.4447	-138.5310
PS2-SR-2	0.5592	14.2037	-131.7721
PS2-SR-3	0.8868	22.5247	-123.4510
PS2-SR-4	1.176	29.8704	-116.1054
PS2-SR-5	1.5042	38.2067	-107.7691
PS1-SR-6	1.816	46.1264	-99.8494
PS1-SR-7	2.1121	53.6473	-92.3284
PS1-SR-8	2.4223	61.5264	-84.4493
PS1-SR-9	2.6853	68.2066	-77.7691
PS1-SR-10	3.005	76.3270	-69.6488
PS1-SR-11	3.3094	84.0588	-61.9170
PS1-SR-12	3.6134	91.7804	-54.1954
PS1-SR-13	3.9094	99.2988	-46.6770
PS1-SR-14	4.2259	107.3379	-38.6379
PS1-SR-15	4.5235	114.8969	-31.0789
PS1-SR-16	4.8306	122.6972	-23.2785
PS1-SR-17	5.1124	129.8550	-16.1208
PS1-SR-18	5.4132	137.4953	-8.4805
PS2-SR-19	0.2777	7.0536	-138.9222
PS2-SR-20	0.5532	14.0513	-131.9245
PS2-SR-21	0.8531	21.6687	-124.3070
PS2-SR-22	1.1539	29.3091	-116.6667
PS2-SR-23	1.4751	37.4675	-108.5082
PS1-SR-24	1.7759	45.1079	-100.8679
PS1-SR-25	2.0968	53.2587	-92.7170
PS1-SR-26	2.4101	61.2165	-84.7592
PS1-SR-27	2.714	68.9356	-77.0402
PS1-SR-28	2.9896	75.9358	-70.0399
PS1-SR-29	3.3171	84.2543	-61.7214
PS1-SR-30	3.6258	92.0953	-53.8804
PS1-SR-31	3.9045	99.1743	-46.8015
PS1-SR-32	4.2053	106.8146	-39.1611
PS1-SR-33	4.4966	114.2136	-31.7621
PS1-SR-34	4.8068	122.0927	-23.8830
PS1-SR-35	5.1155	129.9337	-16.0421
PS1-SR-36	5.4179	137.6147	-8.3611
PS3-SR-37	-1.80	-45.7200	-191.6958
PS3-SR-38	-1.80	-45.7200	-191.6958
PS3-SR-39	-1.80	-45.7200	-191.6958

Table A4. Bell Nozzle Wall Pressures

Pressure Tap	Axial Station Relative to Nozzle Exit (mm)	Axial Station Relative to Nozzle Throat (mm)	Nozzle Pressure Ratio				
			10.41	19.83	19.87	19.89	19.15
			Pwall/Pnozzle_inlet				
PS2-SR-1	-138.5310	7.4447	0.0993	0.0984	0.0983	0.0986	0.0986
PS2-SR-2	-131.7721	14.2037	0.0858	0.0859	0.0859	0.0861	0.0861
PS2-SR-3	-123.4510	22.5247	0.0697	0.0694	0.0694	0.0695	0.0695
PS2-SR-4	-116.1054	29.8704	0.0541	0.0540	0.0540	0.0543	0.0543
PS2-SR-5	-107.7691	38.2067	0.0439	0.0439	0.0439	0.0440	0.0440
PS1-SR-6	-99.8494	46.1264	0.0367	0.0364	0.0364	0.0365	0.0365
PS1-SR-7	-92.3284	53.6473	0.0848	0.0319	0.0319	0.0320	0.0320
PS1-SR-8	-84.4493	61.5264	0.0898	0.0285	0.0285	0.0285	0.0286
PS1-SR-9	-77.7691	68.2066	0.0908	0.0253	0.0253	0.0253	0.0253
PS1-SR-10	-69.6488	76.3270	0.0915	0.0225	0.0225	0.0225	0.0225
PS1-SR-11	-61.9170	84.0588	0.0920	0.0203	0.0203	0.0203	0.0203
PS1-SR-12	-54.1954	91.7804	0.0923	0.0183	0.0183	0.0184	0.0184
PS1-SR-13	-46.6770	99.2988	0.0923	0.0171	0.0171	0.0171	0.0171
PS1-SR-14	-38.6379	107.3379	0.0924	0.0157	0.0157	0.0158	0.0158
PS1-SR-15	-31.0789	114.8969	0.0926	0.0169	0.0164	0.0160	0.0340
PS1-SR-16	-23.2785	122.6972	0.0928	0.0387	0.0384	0.0381	0.0437
PS1-SR-17	-16.1208	129.8550	0.0928	0.0469	0.0468	0.0467	0.0490
PS1-SR-18	-8.4805	137.4953	0.0930	0.0444	0.0442	0.0441	0.0472
PS2-SR-19	-138.9222	7.0536	0.0990	0.0984	0.0985	0.0986	0.0987
PS2-SR-20	-131.9245	14.0513	0.0855	0.0844	0.0844	0.0845	0.0843
PS2-SR-21	-124.3070	21.6687	0.0690	0.0686	0.0686	0.0688	0.0688
PS2-SR-22	-116.6667	29.3091	0.0550	0.0550	0.0550	0.0551	0.0551
PS2-SR-23	-108.5082	37.4675	0.0457	0.0455	0.0455	0.0457	0.0457
PS1-SR-24	-100.8679	45.1079	0.0385	0.0384	0.0384	0.0384	0.0384
PS1-SR-25	-92.7170	53.2587	0.0822	0.0322	0.0322	0.0323	0.0323
PS1-SR-26	-84.7592	61.2165	0.0893	0.0279	0.0279	0.0280	0.0280
PS1-SR-27	-77.0402	68.9356	0.0909	0.0244	0.0244	0.0245	0.0245
PS1-SR-28	-70.0399	75.9358	0.0916	0.0224	0.0224	0.0225	0.0225
PS1-SR-29	-61.7214	84.2543	0.0922	0.0195	0.0195	0.0196	0.0196
PS1-SR-30	-53.8804	92.0953	0.0924	0.0185	0.0185	0.0185	0.0185
PS1-SR-31	-46.8015	99.1743	0.0924	0.0172	0.0172	0.0172	0.0172
PS1-SR-32	-39.1611	106.8146	0.0925	0.0158	0.0159	0.0159	0.0159
PS1-SR-33	-31.7621	114.2136	0.0927	0.0175	0.0164	0.0159	0.0345
PS1-SR-34	-23.8830	122.0927	0.0930	0.0393	0.0391	0.0389	0.0441
PS1-SR-35	-16.0421	129.9337	0.0932	0.0449	0.0449	0.0448	0.0476
PS1-SR-36	-8.3611	137.6147	0.0926	0.0470	0.0470	0.0469	0.0491
PS3-SR-37	-191.6958	-45.7200	0.9773	0.9761	0.9753	0.9753	0.9754
PS3-SR-38	-191.6958	-45.7200	0.9782	0.9780	0.9769	0.9767	0.9766
PS3-SR-39	-191.6958	-45.7200	bad	bad	bad	bad	bad
Nozzle Base 1A	0.0000	145.9758	0.09453	0.049687	0.049609	0.049552	0.051429
Nozzle Base 2A	0.0000	145.9758	0.09486	0.049802	0.049717	0.04966	0.051536
Nozzle Base 1B	0.0000	145.9758	0.09466	0.049686	0.049567	0.049541	0.051412
Nozzle Base 2B	0.0000	145.9758	0.09570	0.050233	0.050143	0.050094	0.052026
Nozzle Base 1C	0.0000	145.9758	0.09503	0.049921	0.049809	0.049771	0.051692
Nozzle Base 2C	0.0000	145.9758	0.09510	0.049944	0.04987	0.049791	0.051705